

UCLA

UCLA Electronic Theses and Dissertations

Title

Investigating the Wavelength Dependence of Weak Lensing Measurement from a Space Telescope and Estimating the Reduced Shear Signal in the Hubble Space Telescope Frontier Parallel Fields

Permalink

<https://escholarship.org/uc/item/4ch0996f>

Author

Tung, Nathan

Publication Date

2019

Peer reviewed|Thesis/dissertation

UNIVERSITY OF CALIFORNIA

Los Angeles

Investigating the Wavelength Dependence of Weak Lensing Measurement
from a Space Telescope and Estimating the Reduced Shear Signal in the Hubble Space
Telescope Frontier Parallel Fields

A dissertation submitted in partial satisfaction of the
requirements for the degree of Doctor of Philosophy
in Physics

by

Nathan Tung

2019

© Copyright page by

Nathan Tung

2019

ABSTRACT OF THE DISSERTATION

Investigating the Wavelength Dependence of Weak Lensing Measurement
from a Space Telescope using a Simple Model
and Estimating the Reduced Shear at the Hubble Frontier Parallel Fields

by

Nathan Tung

Doctor of Philosophy in Physics

University of California, Los Angeles, 2019

Professor Edward L. Wright, Chair

Ignoring redshift dependence, the statistical performance of a weak lensing survey is set by two numbers: the effective shape noise of the sources, which includes the intrinsic ellipticity dispersion and the measurement noise, and the density of sources that are useful for weak lensing measurements. We provide some general guidance for weak lensing shear measurements from a “generic” space telescope using the galaxy flux signal-to-noise ratio (S/N), ellipticity measurement variance, and effective galaxy number per square degree as metrics to evaluate weak lensing measurement performance across wavelength. Galaxy data are collected from both the ULTRAVISTA field and the Hubble Space Telescope (HST) Frontier Parallel Fields (FPFs) and fitted to radially symmetric Sersic galaxy light profiles. The Sersic galaxy profiles are then stretched to impose an artificial weak lensing shear, and then convolved with a pure Airy Disk

PSF to simulate imaging of weak gravitationally lensed galaxies from a hypothetical diffraction-limited space telescope. Our results consistently show that weak lensing measurements are optimized for the longest wavelengths available in the survey, until thermal background from the telescope or interplanetary dust reduces the sensitivity. We also perform a crude measurement of galaxy ellipticities in the HST FPFs using Source Extractor (SExtractor) software (Bertin & Arnouts, 1996) in order to estimate a reduced shear at the location of the parallel fields. The average ellipticity among a significantly large density of distant galaxy images is directly related to reduced gravitational shear signal, which we approximate with our simplifying assumptions and use to estimate the primary FF galaxy cluster masses to illustrate that shear measurements at long NIR wavelengths are completely reasonable.

This dissertation of Nathan Tung is approved.

Tommaso L. Treu

Matt A. Malkan

Alice Eve Shapley

Edward L. Wright, Committee Chair

University of California, Los Angeles

2019

Contents

1.	Introduction	1
2.	The Standard Cosmological Model	4
2.1.	Robertson-Walker Metric	4
2.2.	The Scale Factor and Redshift	8
2.3.	Evolution of the Scale Factor	9
2.4.	Cosmological Parameters	11
2.5.	Matter Models	13
2.6.	Distance Measures	14
3.	Weak Gravitational Lensing	18
3.1.	Gravitational Lensing: Strong vs. Weak	18
3.2.	Applications of Weak Lensing	23
3.3.	Weak Lensing Theory	25
3.4.	Weak Lensing Strategy	32
3.5.	Tangential and Cross Components of the Shear	37
3.6.	Weak Lensing Measurement	39
3.7.	Our Objective	43
4.	Methodology	46
4.1.	Simple galaxy profile models	47
4.2.	A simple space telescope model	49
4.3.	Calculating Galaxy Flux S/N	52
4.4.	Introducing Shear and Calculating Ellipticity measurement variance	54
4.5.	Analytical Gaussian Calculations	59

4.6.	Calculating an Effective Galaxy Number for Weak Lensing Shape Measurement	63
4.7.	Ellipticity Measurement on the Frontier Parallel Fields	65
5.	Data	70
5.1.	Constructing a galaxy catalog from the UltraVISTA field	71
5.2.	Constructing a galaxy catalog from the HST Frontier Parallel Fields	75
5.3.	Using SExtractor to measure galaxy ellipticity in the Frontier Parallel Fields	80
6.	Results	81
6.1.	UltraVISTA field	81
6.1.1.	Galaxy Flux S/N vs. Wavelength	81
6.1.2.	Ellipticity measurement variance vs. Wavelength	85
6.1.3.	Flux S/N and Ellipticity measurement variance with Gaussian Distributions	89
6.1.4.	Effective Galaxy Number	90
6.1.5.	Intrinsic Galaxy Ellipticity	95
6.1.6.	Dependence on Effective Radius	97
6.2.	HST Frontier Parallel Fields	97
6.2.1.	Weak Lensing Measurement Performance Across Wavelength	97
6.2.2.	Weak Lensing Measurement Performance Across Wavelength	101
7.	Conclusion	111
	References	119

List of Figures

Figure 1 – The overall geometry of the universe	13
Figure 4 – The picture shows a famous cosmic mirage known as the Einstein Cross	19
Figure 5 – Examples of Einstein rings taken with the HST	20
Figure 6 – Distortions of the type produced by weak lensing	22
Figure 7 – The effects of foreground galaxy cluster mass on background galaxy shapes	23
Figure 8 – Angles involved in a thin gravitational lens system	26
Figure 9 – Normalized Sersic galaxy light profile plots for Sersic indices	50
Figure 10 – Normalized airy disk PSF superimposed	51
Figure 11 – Discrete Normalized Sersic Intensity Profile	52
Figure 12 – Discrete normalized airy disk PSF plotted.	52
Figure 13 – Effects of the convergence κ and the components of shear g_1 and g_2	55
Figure 14 – Normalized density plot of $\frac{\Delta I}{I_0} = \frac{I_{x-stretch} - I_{y-stretch}}{I_0}$	58
Figure 15 – Plot of galaxy source counts per square degree	65
Figure 16 – A comparison of a few different weight functions $W(\theta)$	70
Figure 17 — Mean and median AB magnitude of galaxies collected in the Ks catalog	74
Figure 18 — Mean and median AB magnitude of galaxies collected in the R catalog	74
Figure 19 – This image illustrates the “footprints” of the HST cameras	76
Figure 20 – Light paths originating with the galaxy cluster and neighboring parallel field	77
Figure 21 – Galaxy flux S/N vs. wavelength: 1.2 meter telescope, Ks catalog	82
Figure 22 – Galaxy flux S/N vs. wavelength: 2.4 meter telescope, Ks catalog	82
Figure 23 – Galaxy flux S/N vs. wavelength: 1.2 meter telescope, R catalog	83
Figure 24 – Galaxy flux S/N vs. wavelength: 2.4 meter telescope, R catalog	83
Figure 25 – Histogram of maximum S/N: 1.2 meter telescope, Ks catalog	84
Figure 26 – Histogram of maximum S/N: 2.4 meter telescope, Ks catalog	84
Figure 27 – Histogram of maximum S/N: 1.2 meter telescope, R catalog	85
Figure 28 – Histogram of maximum S/N: 2.4 meter telescope, R catalog	85

Figure 29 – Ellipticity variance vs. wavelength:1.2 meter telescope, Ks subset	86
Figure 30 – Ellipticity variance vs. wavelength:2.4 meter telescope, Ks subset	86
Figure 31 – Ellipticity variance vs. wavelength:1.2 meter telescope, R subset	87
Figure 32 – Ellipticity variance vs. wavelength:2.4 meter telescope, R subset	87
Figure 33 – Histogram of min. Variance: 1.2 meter telescope, Ks catalog	88
Figure 34 – Histogram of min. Variance: 2.4 meter telescope, Ks catalog	88
Figure 35 – Histogram of min. Variance: 1.2 meter telescope, R catalog	89
Figure 36 – Histogram of min. variance: 2.4 meter telescope, R catalog	89
Figure 37 – Gaussian ellipticity measurement variance vs. wavelength	90
Figure 38 – Non-Gaussian ellipticity measurement variance vs. wavelength	90
Figure 39 – Effective number vs. integration time: 1.2 meter telescope, Ks catalog	91
Figure 40 – Effective number vs. integration time: 2.4 meter telescope, Ks catalog	92
Figure 41 – Effective number vs. integration time: 1.2 meter telescope, R catalog	93
Figure 42 – Effective number vs. integration time: 2.4 meter telescope, R catalog	94
Figure 43 – Ellipticity variance vs. wavelength with intrinsic 2:1 elliptical axis ratio	96
Figure 44 – Plot of total K-flux vs. effective half-light radius in the Ks subset	97
Figure 45 – Plot of galaxy flux S/N vs. wavelength for all six FPFs	98
Figure 46 – Plot of galaxy shape variance vs. wavelength for all six FPFs	99
Figure 47 – Plot of the effective number vs. integration time for all six FPFs	100
Figure 48 – The relative pointing directions of Abell 2744 field	104
Figure 49 – The relative pointing directions of Abell 1063 field	105
Figure 50 – The relative pointing directions of Abell 370 field	106
Figure 51 – The relative pointing directions of MACS 1149 field	107
Figure 52 – The relative pointing directions of MACS 0717 field	108
Figure 53 – The relative pointing directions of MACS 0416 field	109
Figure 54 – Polar plot of individual galaxy ellipticity vectors in Abell 2744	110

List of Tables

Table 1 – Table of sample sky background intensities	54
Table 2 – Average total flux values for UltraVISTA catalogs	73
Table 3—SExtractor Configuration Parameters	79
Table 4 — Average statistics of the combined six FPF catalogs	80
Table 5 – Effective number of galaxy sources in each HST FPF	81
Table 6 – Table summarizing the reduced shear magnitude and angle for each of the FPFs and an estimated encircled mass estimate at the location of the parallel fields	103

CURRICULUM VITA

EDUCATION

PhD (Expected)

UCLA, Physics June 2019
Dissertation: "Investigating the Wavelength Dependence of Weak Lensing Measurement from a Space Telescope and Estimating the Reduced Shear Signal in the Hubble Space Telescope Frontier Parallel Fields"
Committee: Edward L. Wright (chair), Tommaso L. Treu, Matt A. Malkan, Alice E. Shapley

MS UCLA, Physics June 2011

BS Cal Poly Pomona, Physics June 2008
Graduated Summa Cum Laude
Minored in Mathematics

HONORS AND AWARDS

Outstanding Teaching Award, UCLA 2017 – 2018
Annual award for exceptional performance as a Teaching Assistance

Outstanding Teaching Award, UCLA 2010 – 2011
Annual award for exceptional performance as a Teaching Assistance

Outlaws of Physics Scholarship, Cal Poly Pomona 2008
Annual scholarship awarded to one outstanding undergraduate physics student

TEACHING EXPERIENCE

Teaching Assistant, UCLA September 2010 to June 2019
Physics and Astronomy Department

PEERS Facilitator, UCLA September 2012 to June 2017
Life and Physical Science Departments

Teaching Assistant Coordinator, UCLA September 2013
Physics and Astronomy Department

Physics Lecturer, Cal Poly Pomona September 2008 to June 2009
Physics Department

RESEARCH EXPERIENCE

Dissertation, UCLA, Physics and Astronomy Department 2019

Advisor: Professor Edward L. Wright

- Topics: Weak gravitational lensing, dark matter, statistical methods

Undergraduate Senior Project, Cal Poly Pomona 2007 to 2008

Advisor: Professor Kai Lam

- Study of Ed Witten's work involving quantum field theory and knot theory

Undergraduate Research, Cal Poly Pomona 2007 to 2009

Advisor: Professor Antonio Aurilia

- Investigation of the unification of physics at the Planck scale

PUBLICATIONS

Journal Publications

Tung, N. & Wright, E., 2017. On Using a Space Telescope to Detect Weak-lensing Shear. *PASP*, Volume 129.

PRESENTATIONS AND INVITED LECTURES

Seminar Presentation, "Unification of Physics at the Planck Scale," Cal Poly Pomona Physics Seminar, 2009.

Poster Presentation, "Unification of Physics at the Planck Scale," Undergraduate poster conference, 2009.

Poster Presentation, "Quantum Field Theory and Knots," Undergraduate senior project, 2008.

PROFESSIONAL AFFILIATIONS

AAPT, 2019-Present
American Association of Physics Teachers

SCAAPT, 2019-Present
Southern California section of AAPT

Sigma Pi Sigma, 2007-Present
Physics Honor Society

1. Introduction

Weak gravitational lensing has become a powerful tool for dark matter studies since lensing distortions depend on the total matter distribution, light plus dark. Many cosmic shear measurements have been done by ground-based telescopes, such as CFHTLS (Heymans, et al., 2012), VST-KIDS (VLT Survey Telescope – Kilo-Degree Survey) (Baxter, et al., 2013), Pan-STARRS (Kaiser, 2007), LSST (LSST-Science-Collaboration, et al., 2009) and DES (Baxter, et al., 2018). However, such results have their limitations. Weak lensing requires high image quality for the shear measurements, near-infrared imaging capabilities to measure photometric redshifts for galaxies at redshifts $z > 1$, a very high degree of system stability to minimize systematic effects, and the ability to survey large sectors of the extragalactic sky. This combination of requirements is hard to meet from the ground and demands a wide field Visible/NIR space mission (Refregier, et al., 2010). Of particular interest is the future launch of two space telescopes: the 1.2 meter Euclid space telescope, currently under development by the European Space Agency (ESA), and NASA's 2.4 meter Wide Field Infrared Survey Telescope-Astrophysics Focused Telescope Assets (WFIRST).

The Euclid space telescope will consist of a 1.2 meter diameter primary mirror, an imaging instrument consisting of a CCD-based visible optical channel and a Near IR Spectrometer and Imaging Photometer (NISIP). The visible channel will allow for measurement of the shapes of galaxies for weak lensing with a resolution of 0.18 arcseconds (PSF FWHM) with 0.1 arcsecond pixels in a wide red band (R+I+Z). The NISIP instrument images in the 0.9-2.0 micron range (Y, J, H bands) with 0.3 arcsecond pixels (Racca, et al., 2016). The launch date of the Euclid spacecraft is currently planned for 2020.

NASA's 2.4 meter WFIRST has a tentative launch date of 2024. The imaging capability of WFIRST will have a field of view of 0.281 square degrees with a pixel scale of 0.11 arcseconds per pixel over a wavelength range of 0.76 μm – 2.0 μm . The point spread function (PSF) encircled energy at 50% ranges from 0.11 arcseconds to 0.14 arcseconds over this wavelength range (Spergel, et al., 2015). Both space telescopes are expected to provide unprecedented measurements for weak lensing studies.

While real-life measurements of cosmic shear must account for a variety of complicating factors including galaxy structure, telescope seeing, and sources of noise, in this research we present a simplistic model calculation for the ellipticity measurement noise with a goal of locating the optimum wavelength band for cosmic shear measurements to be performed from a hypothetical diffraction-limited space telescope. Our calculation assumes a pure airy disk PSF for a fully illuminated circular aperture, galaxy light intensity profiles modeled by Sersic's equation (Sersic, 1963), and sky-dominated noise. Sersic galaxy light profiles are radially symmetric, so we introduce gravitational shear in our model as a small perturbation on the radial symmetry of the light profiles given by Sersic's equation, and then calculate the error of the shape measurement after telescope diffraction constrained to the assumptions stated above. We also calculate an effective galaxy number per square degree across different wavelength bands, taking into account the density of sources that are useful for weak lensing measurements and the effective shape noise of sources. From the data collected in this paper across galaxy sets from both the UltraVISTA Ks-selected and R-selected catalogs (Muzzin, et al., 2013), and the HST FPFs, we find that the longest wavelength available in the survey gives the minimum average ellipticity measurement variance, the maximum average galaxy flux S/N, and the maximum effective galaxy number counts.

We also perform a crude measurement of galaxy ellipticities in the HST FPFs using Source Extractor (SExtractor) software (Bertin & Arnouts, 1996) in order to estimate a reduced shear at the location of the parallel fields using the H-band, the longest wavelengths available in the HST FF data. In an effort to simplify the procedure, we assume a purely symmetric Gaussian PSF. While this choice is unrealistic and unrepresentative of the HST, it makes deconvolution of the PSF simple and allows for relatively easy extraction of an approximate galaxy source ellipticity signal. The average ellipticity among a significantly large density of distant galaxy images is directly related to reduced gravitational shear signal, which we approximate with our simplifying assumptions and calibrate to more strictly accurate values reported elsewhere in the literature to obtain an estimated encircled mass which we expect to correlate with the primary cluster masses of the FFs.

This paper is organized as follows. In Chapter 2 we review the standard cosmological model that forms the background of gravitational lensing theory. In Chapter 3 we provide a brief summary of weak gravitational lensing and measurement considerations and motivate our work. Chapter 4 describes the methodology of our analysis, including details of our model diffraction-limited telescope and Sersic galaxy profiles, equations and calculations for the flux SNR, shape measurement uncertainty, and effective galaxy number per square degree which we use to evaluate weak lensing measurement across wavelengths. This chapter also outlines the procedure and assumptions used to estimate the average reduced shear signal in the HST FPFs. In Chapter 5 we describe the galaxy data collected from the UltraVISTA and FPFs and the creation of the galaxy catalogs used in this study. In Chapter 6 we present the results of our calculations, including plots of the flux SNR and galaxy shape uncertainty vs. wavelength, and of the effective galaxy number per square degree vs. integration time across wavelength bands, and our results

for average ellipticity measurements on the FPFs to obtain estimates of the reduced shear and encircled mass. We draw our conclusions in Section 7. Methodology, Data and Results sections for the UltraVISTA fields heavily reference the author's previous publication (Tung & Wright, 2017).

2. The Standard Cosmological Model

In this Chapter, we review aspects of the standard cosmological model which have relevance for further discussion of weak gravitational lensing. This model is consistent with a description of a cosmological background which is a homogeneous and isotropic solution of the field equations of General Relativity, and is the standard cosmological model covered in most General Relativity text books; see for example, (Carroll, 2004).

2.1. Robertson-Walker Metric

General Relativity describes space-time as a four-dimensional manifold whose metric tensor $g_{\alpha\beta}$ is considered as a dynamic field. The dynamics of the metric are governed by Einstein's field equations, which relate the Einstein tensor to the stress-energy tensor of the matter contained in space-time. Two events in space-time with coordinates differing by dx^α are separated by ds , with $ds^2 = g_{\alpha\beta}dx^\alpha dx^\beta$ (Einstein summation convention implied). The eigentime, or proper time, of an observer who travels by ds changes by $c^{-1}ds$, where c is the speed of light. We use the convention that Greek indices run over 0...3 denoting coordinates of four-dimensional space-time while Latin indices run over the spatial indices 1...3 only. The sign convention $(+, -, -, -)$ shall be used throughout.

The standard cosmological model stems from two postulates motivated by modern observational cosmology: 1) When averaged over sufficiently large scales, the universe is isotropic. 2) When averaged over sufficiently large scales, the universe is homogeneous.

Isotropy applies at some specific point in the manifold, and states that space looks the same in any direction. Homogeneity is the statement that the metric is the same throughout the manifold. In general, there is no necessary relationship between isotropy and homogeneity; a manifold can be homogeneous but nowhere isotropic, or it can be isotropic at a point but not homogenous. However, if space is isotropic everywhere, then it is guaranteed to be homogenous, and if space is isotropic around a point and also homogenous, then it will be isotropic around every point.

Isotropy in the universe implies that clocks can be synchronized such that the space-time components of the metric tensor vanish, $g_{0i} = 0$. In other words, no particular direction in space-time can be singled out as special. The space and time components of the metric can thus be separated and the universe can be foliated into space-like slices such that each three-dimensional slice is isotropic and homogeneous. We can therefore consider space-time to be $\mathbb{R} \times \Sigma$, where \mathbb{R} represents the time direction and Σ is a isotropic and homogeneous three-manifold. The space-time metric can then generally be written in the form

$$ds^2 = c^2 dt^2 + g_{ij} dx^i dx^j \quad [1]$$

where g_{ij} is the metric of spatial hypersurfaces.

In order to not violate isotropy and homogeneity, the spatial metric can only be allowed to isotropically contract or expand with a scale function $a(t)$ which must be only a function of time. The scale function cannot be allowed to vary with space, otherwise the expansion would be allowed to differ at different locations in the universe, violating the postulate of homogeneity.

With all of this, the metric can further be simplified to

$$ds^2 = c^2 dt^2 - a^2(t) d\sigma^2 \quad [2]$$

where $d\sigma$ is the line element of the three-space Σ and $d\sigma^2$ gives the three-dimensional space metric on Σ ,

$$d\sigma^2 = \gamma_{ij} du^i du^j \quad [3]$$

A special case of the metric [2] is the Minkowski metric of Special Relativity, for which $d\sigma$ is the Euclidian line element and $a(t)$ is constant. Homogeneity also implies that all quantities describing the matter content of the Universe, e.g., density and pressure, can only be functions of time. The scale factor in [2] tells us how big the space-like slice of Σ is at the moment t .

The coordinates used here, in which the metric is free of cross terms $dt du^i$ and the coefficient of dt^2 is independent of the u^i , are known as comoving coordinates. Only a comoving observer will perceive an isotropic universe. Non-comoving observers will see regions of the sky systematically blue-shifted or red-shifted, and in fact, Earth is not quite comoving, and as a result we see a dipole anisotropy in the cosmic microwave background as a result of the conventional Doppler effect. The comoving time coordinate is the elapsed time since the Big Bang according to a clock of a comoving observer, and is a measure of cosmological time. Space in comoving coordinates is usually referred to as being “static”, as most bodies on the scale of galaxies or larger are approximately comoving, and comoving bodies have static, unchanging comoving coordinates. So for a pair of comoving galaxies, while the proper distance between them would have been smaller in the past and become larger in the future due to the expansion of space, the comoving distance between them remains constant at all times.

The spatial hypersurface Σ can either be flat or curved. Isotropy only requires them to be spherically symmetric; i.e., spatial surfaces of constant distance from an arbitrary point need to be two-spheres. Homogeneity permits us to choose an arbitrary point as a coordinate origin. We can then introduce two angles θ, ϕ which uniquely identify positions on the unit sphere around

the origin, and a radial coordinate χ . The most general admissible form for the spatial line element is then

$$d\sigma^2 = d\chi^2 + f_K^2(\chi)(d\phi^2 + \sin^2 \theta d\theta^2) \equiv d\chi^2 + f_K^2(\chi)d\Omega^2 \quad [4]$$

Homogeneity then requires that the radial function $f_K^2(\chi)$ is either a trigonometric, linear, or hyperbolic function of χ , depending on whether the curvature K is positive, zero, or negative.

Specifically,

$$f_K(w) = \begin{cases} K^{-1/2} \sin(K^{-1/2} \chi) & (K > 0) \\ \chi & (K = 0) \\ (-K^{-1/2}) \sinh[(-K^{-1/2})\chi] & (K < 0) \end{cases} \quad [5]$$

Here, $f_K(\chi)$, and thus $|K|^{-1/2}$ has the dimension of a length. If we define the radius r of the two-spheres by $f_K(\chi) \equiv r$, the metric $d\sigma^2$ takes the alternative form

$$d\sigma^2 = \frac{dr^2}{1 - Kr^2} + r^2 d\Omega^2 \quad [6]$$

where

$$d\chi^2 = \frac{dr^2}{1 - Kr^2} \quad [7]$$

The value of K in [6] sets the curvature, and therefore the size, of the spatial surfaces. It is common to normalize K so that $K \in \{-1, 0, 1\}$ and absorbed the physical size of the manifold into the scale factor $a(t)$. Then, the $K = -1$ case corresponds to constant negative curvature on Σ , and is sometimes called open; the $K = 0$ case corresponds to no curvature, and is called flat; the $K = +1$ case corresponds to positive constant positive curvature on Σ , and is sometimes called closed.

For the flat case $K = 0$, the metric on Σ becomes Euclidean:

$$\begin{aligned}
d\sigma^2 &= d\chi^2 + \chi^2 d\Omega^2 \\
&= dx^2 + dy^2 + dz^2
\end{aligned}
\tag{8}$$

Globally, it could describe \mathbb{R}^3 or a more complicated manifold, such as a three-torus $S^1 \times S^1 \times S^1$.

For the closed case $K = +1$ we have

$$d\sigma^2 = d\chi^2 + \sin^2 \chi d\Omega^2 \tag{9}$$

which is the metric of a three-sphere S^3 . In this case the only possible global structure is the complete three-sphere (except for the nonorientable manifold obtained by identifying antipodal points on S^3).

For the open case $K = -1$, we obtain

$$d\sigma^2 = d\chi^2 + \sinh^2 \chi d\Omega^2 \tag{10}$$

This is the metric for a three-dimensional space of constant negative curvature. Globally such a space could extend forever, which is the origin of the word “open”, but it could technically also describe a nonsimply-connected compact space (so “open” is not really the most accurate label).

The metric on space-time describes one of these hypersurfaces evolving in size, and can be written

$$ds^2 = c^2 dt^2 - a^2(t) \left[\frac{dr^2}{1 - Kr^2} + r^2 d\Omega^2 \right] \tag{11}$$

This is the Robertson-Walker metric.

2.2. The Scale Factor and Redshift

Due to the expansion of space, photons are redshifted as they propagate from a source to an observer. Consider a comoving source emitting a light signal at t_{em} which reaches a comoving observer at the coordinate origin $w = 0$ at some time t_{obs} . Since $ds = 0$ for light, a backward-

directed radial light ray propagates according to $|cdt| = a(t)d\chi$, from the metric. The comoving coordinate distance between source and observer is constant by definition,

$$d\chi_{em-obs} = \int_{obs}^{em} d\chi = \int_{t_{em}}^{t_{obs}(t_{em})} \frac{c dt}{a} = \text{constant} \quad [12]$$

Since this is constant, the derivative of χ_{em-obs} with respect to t_s is zero. It then follows that

$$\frac{dt_{obs}}{dt_{em}} = \frac{a(t_{obs})}{a(t_{em})} \quad [13]$$

Identifying the inverse time intervals $(dt_{em,obs})^{-1}$ with the source emitted and the observed light frequencies $\nu_{s,o}$, and denoting the wavelength of light by λ , we can write

$$\frac{dt_{obs}}{dt_{em}} = \frac{\nu_{em}}{\nu_{obs}} = \frac{\lambda_{obs}}{\lambda_{em}} \quad [14]$$

Since the redshift z is defined as the relative change in wavelength, or $1 + z = \lambda_{obs}\lambda_{em}^{-1}$, we find that

$$1 + z = \frac{\lambda_{obs}}{\lambda_{em}} = \frac{a(t_{obs})}{a(t_{em})} \quad [15]$$

This shows that light is redshifted by the amount by which the Universe has expanded between emission and observation. If the observation takes place today, we typically take

$a(t_o) = a_{obs} = a_0 = 1$ and can write

$$a_{em} = \frac{1}{1 + z} \quad [16]$$

2.3. Evolution of the Scale Factor

To complete the description of space-time, we need to know how the scale function $a(t)$ depends on time, and how the curvature K depends on the matter which fills space-time. In

General Relativity, the dynamics of space-time are determined by Einstein's field equations relating the Einstein tensor $G_{\alpha\beta}$ to the stress-energy tensor $T_{\alpha\beta}$ of the matter,

$$G_{\alpha\beta} = \frac{8\pi G}{c^2} T_{\alpha\beta} + \Lambda g_{\alpha\beta} \quad [17]$$

The second term proportional to the metric tensor $g_{\alpha\beta}$ is the cosmological constant, originally introduced by Einstein to allow for a static Universe. For the highly symmetric form of the Robertson-Walker metric, Einstein's equations imply that $T_{\alpha\beta}$ has to have the form of the stress-energy tensor of a homogeneous perfect fluid, which is characterized by its density $\rho(t)$ and its pressure $p(t)$. Homogeneity requires the density and pressure depend only on time. The field equations then simplify to the two independent equations

$$\left(\frac{\dot{a}}{a}\right)^2 = \frac{8\pi G}{3} \rho - \frac{Kc^2}{a^2} + \frac{\Lambda}{3} \quad [18]$$

and

$$\left(\frac{\ddot{a}}{a}\right)^2 = -\frac{4\pi}{3} G \left(\rho + \frac{3p}{c^2}\right) + \frac{\Lambda}{3} \quad [19]$$

Together these are known as the Friedmann equations, and metrics of the form of equations [2], [3], and [4] are called Friedmann-Robertson-Walker (FRW) metrics.

The scale factor $a(t)$ is determined once its value at one instant of time is fixed. We choose $a = 1$ at the present epoch t_0 . The two equations [18] and [19] can be combined to yield the *adiabatic equation*

$$\frac{d}{dt} [a^3(t)\rho(t)c^2] + p(t) \frac{da^3(t)}{dt} = 0 \quad [20]$$

The first term $a^3\rho$ is proportional to the energy contained in a fixed comoving volume, and hence the equation states that the change in "internal" energy equals the pressure times the

change in proper volume. Equation [20] is thus a statement of the first law of thermodynamics in the cosmological context.

2.4. Cosmological Parameters

The rate of expansion is characterized by the *Hubble Parameter*, defined as

$$H \equiv \frac{\dot{a}}{a} \quad [21]$$

The value of the Hubble parameter at the present epoch $t = t_0$ is the *Hubble Constant*

$$H(t_0) = H_0 \quad [22]$$

Current measurements roughly fall into the range of

$$H_0 = 100h \text{ km sec}^{-1} \text{ Mpc}^{-1} \quad [23]$$

with $h = (0.5 - 0.8)$. This has measurements of inverse time, hence,

$$H_0 \approx 3.2 \times 10^{-18} h \text{ sec}^{-1} \approx 1.0 \times 10^{-10} h \text{ yr}^{-1} \quad [24]$$

The time scale for the expansion of the Universe is the inverse Hubble constant, or

$$H_0^{-1} \approx 1.0 \times 10^{10} h^{-1} \text{ yr} \quad [25]$$

The *Hubble distance* is defined as

$$d_H = \frac{c}{H_0} \quad [26]$$

The combination

$$\frac{3H_0^2}{8\pi G} = \rho_{cr} \approx 1.9 \times 10^{-29} h^2 \text{ g cm}^{-3} \quad [27]$$

is the *critical density* of the Universe, and the density ρ_0 in units of ρ_{cr} is the *density parameter*

Ω_0 ,

$$\Omega_0 = \frac{\rho_0}{\rho_{cr}} = \frac{8\pi G}{3H_0^2} \rho_0 \quad [28]$$

This quantity, which will generally change with time, is called the “critical” density because the Friedmann equation [18] can be written

$$\Omega_0 - 1 = \frac{K}{H^2 a^2} \quad [29]$$

The sign of K is thus determined by whether Ω_0 is greater than, equal to, or less than, unity:

$$\rho_0 < \rho_{cr} \quad \leftrightarrow \quad \Omega_0 < 1 \quad \leftrightarrow \quad K < 0 \quad \leftrightarrow \quad \text{open}$$

$$\rho_0 = \rho_{cr} \quad \leftrightarrow \quad \Omega_0 = 1 \quad \leftrightarrow \quad K = 0 \quad \leftrightarrow \quad \text{flat}$$

$$\rho_0 > \rho_{cr} \quad \leftrightarrow \quad \Omega_0 > 1 \quad \leftrightarrow \quad K > 0 \quad \leftrightarrow \quad \text{closed}$$

The density parameter then tells us which of the three Robertson-Walker geometries describes our Universe. Recent measurements of the cosmic microwave background anisotropy lead us to believe that Ω_0 is very close to unity.

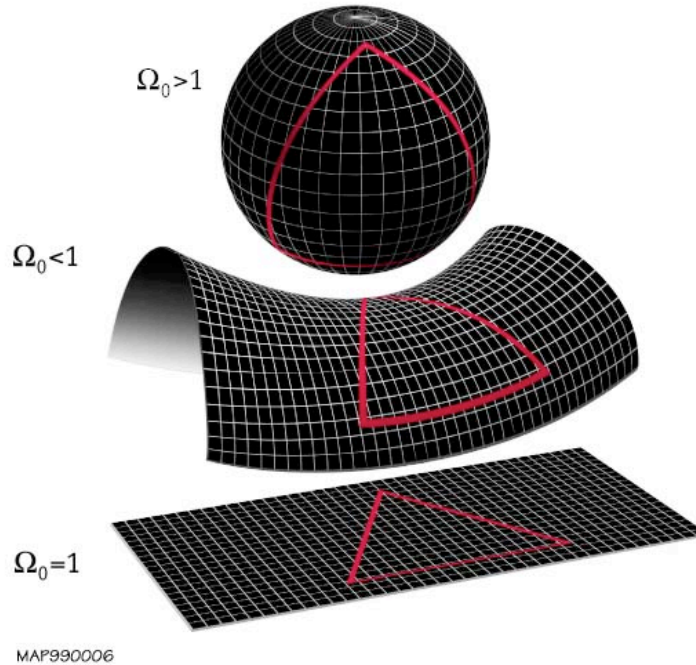


Figure 1 – The overall geometry of the universe is determined by whether the Omega cosmological parameter is less than, equal to or greater than 1. Shown from top to bottom are a closed universe with positive curvature, a hyperbolic universe with negative curvature and a flat universe with zero curvature.

Source: <https://wmap.gsfc.nasa.gov/media/990006/index.html> (NASA, 2011)

We further define

$$\Omega_\Lambda \equiv \frac{\Lambda}{3H_0^2} \tag{30}$$

as the *cosmological-constant energy density*, which represents the vacuum or dark energy density of the universe in absence of all other forms of matter or radiation.

2.5. Matter Models

A complete description of the expansion of the Universe requires an equation of state,

$p = p(\rho)$, relating the pressure to the energy density of the matter. Ordinary matter, which is frequently called *dust* in this context, has $p \ll \rho c^2$, while radiation or other forms of relativistic matter have $p = \rho c^2/3$. Plugging these into the adiabatic equation [20], we find

$$\rho(t) = a^{-n}(t)\rho_0 \quad [31]$$

with

$$n = \begin{cases} 3 & \text{for dust, } p = 0 \\ 4 & \text{for relativistic matter, } p = \rho c^2/3 \end{cases} \quad [32]$$

The energy density of relativistic matter therefore drops more rapidly with time than that of ordinary matter.

2.6. Distance Measures

The meaning of “distance” is no longer unique in a curved space-time. The instantaneous physical distance is a convenient construct, but not itself observable, since observations always refer to events on our past light cone, not our current spatial hypersurface. In Euclidean space there are a number of different ways to infer the distance of an object; we could compare its apparent brightness to its intrinsic luminosity, or its apparent angular velocity to its intrinsic transverse speed, or its apparent angular size to its physical extent. For each of these cases, we can define a different kind of distance that we would infer if space were Euclidean and the Universe were not expanding. Since the local spatial geometry is Euclidean, we want these definitions of “distance” in cosmology to coincide with the common notion of distance at low redshift.

Distance measures relate an emission event and an observation event on two separate geodesic lines which fall on a common light cone, either the forward light cone of the source or the backward light cone of the observer. They are therefore characterized by the times t_{em} and

t_{obs} of the emission and observation respectively, and by the structure of the light cone. These times can uniquely be expressed by the values $a_{em} = a(t_{em})$ and $a_{obs} = a(t_{obs})$, or by their corresponding redshifts $z = z_{em}$ and z_{obs} . Since redshifts are directly observable, we choose the latter parametrization. Furthermore, if we are the observer at the current epoch, we can take $a_{obs} = 1$, $z_{obs} = 0$, and $z = z_{em}$.

The evolution of the Hubble parameter, as a function of redshift and density parameters, can be written as

$$H(z) = H_0 E(z) \quad [33]$$

where

$$E(z) = \sqrt{\Omega_r(1+z)^4 + \Omega_m(1+z)^3 + \Omega_k(1+z)^2 + \Omega_\Lambda} \quad [34]$$

Here, Ω_r is the total radiation energy density, Ω_m is the total matter density, Ω_Λ is the dark energy density, and $\Omega_k = 1 - \Omega_m - \Omega_\Lambda$ represents the curvature. To compute distance to an object from its redshift, the above equation must be integrated. In general, and for our Universe, only numerical solutions of such integration is possible, and closed analytical forms only exist for special limited choices of the parameters.

The *comoving distance* is defined to be the distance between two points measured along a path defined at the present cosmological time. The comoving distance from an observer to a distant object (e.g., a galaxy) can be computed by

$$d_c(z) = d_H \int_0^z \frac{dz'}{E(z')} \quad [35]$$

where d_H is the Hubble distance defined by [26]. The comoving distance between fundamental observers, i.e., observers that are both moving with the Hubble flow, does not change with time, as comoving distance accounts for the expansion of the Universe. In contrast, the *proper distance* d_p , roughly corresponds to where a distant object would be at a specific moment of cosmological

time, which can change over time due to the expansion of the Universe. Comoving distance factors out the expansion of the universe, giving a notion of distance that does not change in time due to spatial expansion, $d_p(t) = a(t)d_c(t)$. Locally (infinitesimal redshift separation), or at the same present time, the two distances are the same.

The *proper motion distance*, or *transverse comoving distance*, d_M is the distance inferred from the intrinsic and observed motion of a distance source,

$$d_M = \frac{u}{\dot{\theta}} \quad [36]$$

where u is the proper transverse velocity, and $\dot{\theta}$ is the observed angular velocity. This depends on whether the Universe has positive, flat, or negative curvature:

$$d_M = \begin{cases} \frac{d_H}{\sqrt{\Omega_k}} \sinh(\sqrt{\Omega_k} d_C(z)/d_H), & \text{for } \Omega_k > 0 \\ d_C(z), & \text{for } \Omega_k = 0 \\ \frac{d_H}{\sqrt{\Omega_k}} \sinh(\sqrt{\Omega_k} d_C(z)/d_H), & \text{for } \Omega_k < 0 \end{cases} \quad [37]$$

The *angular diameter distance* d_A is the distance inferred from the intrinsic size x and the observed size of the source θ ,

$$d_A = \frac{x}{\theta} \quad [38]$$

In terms of the transverse comoving distance, it can be written as

$$d_A(z) = \frac{d_M(z)}{1+z} \quad [39]$$

The *luminosity distance* d_L is defined from the relationship between the absolute luminosity of a source L and the observed flux of the object F (the energy per unit time per unit area of the same detector),

$$F = \frac{L}{4\pi d_L^2} \Rightarrow d_L = \sqrt{\frac{L}{4\pi F}} \quad [40]$$

This definition comes from the fact that in flat space, for a source at distance d the flux over the luminosity is just one over the area of a sphere centered around the source,

$F/L = 1/A(d) = 1/4\pi d^2$. In a FRW universe, however, the flux will be diluted. Conservation of photons tells us that all of the photons emitted by the source will eventually pass through a sphere at comoving distance χ from the emitter, but the flux is also diluted by two additional effects: 1) the individual photons redshift by a factor $(1+z)$, and 2) the photons hit the sphere less frequently, since two photons emitted a time δt apart will be measured at a time $(1+z)\delta t$ apart. Therefore, we have

$$\frac{F}{L} = \frac{1}{(1+z)^2 A} \quad [41]$$

The area A of a sphere at comoving distance χ can be derived from $d\Omega^2$ in the Robertson-Walker metric [11], and depends on whether the curvature of the Universe is positive, flat, or negative.

Fortunately, the dependence on all of the cosmological parameters is common to all the distance measures, and one can simply write:

$$d_L(z) = (1+z)d_M = (1+z)^2 d_A \quad [42]$$

So having measured any one such distance, it can easily be converted to any other. On the other hand, different independent measurements of different distances can be compared to test the consistency of the Robertson-Walker metric.

3. Weak Gravitational Lensing

Here we provide a brief overview of weak lensing theory and measurement and motivate our investigation of the wavelength dependence of weak lensing shape measurement. Gravitational lensing is discussed in general at first, including some distinctions between strong lensing and weak lensing. We then turn our attention to some practical considerations of weak lensing measurements. The chapter concludes with the motivation and statement of our scientific objective.

3.1. Gravitational Lensing: Strong vs. Weak

General Relativity dictates that light rays passing near a massive body are deflected. The effect is similar to that of an optical lens, hence the term “gravitational lensing”. Moreover, gravitational light deflection is independent of the nature and the state of the matter which causes the deflection. Since gravitational lensing is sensitive to the total matter distribution, light plus dark, it has become a valuable tool for investigating dark matter distributions.

In extreme examples of gravitational lensing, cosmic bodies of sufficient mass and density are capable of bending light rays from a single background source so that multiple rays can reach the observer. The result is an image in the direction of each ray, producing multiple images. If the source is aligned with lens and observer, then the symmetric deflection of rays towards the observer can result in a ring-like distortion of the source. Such images are aptly named Einstein rings, or Einstein arcs in the more typical case of close but non-perfect alignment, resulting in images smeared into incomplete rings, or circular arcs.



Figure 2 – The picture shows a famous cosmic mirage known as the Einstein Cross, and is a direct visual confirmation of the theory of general relativity. The core galaxy, UGC J224030.2+032131 is lensing multiple images of a distant quasar located in the background of the galaxy.

“Seeing quadruple” ESA/Hubble & NASA 2012. (NASA, 2012)

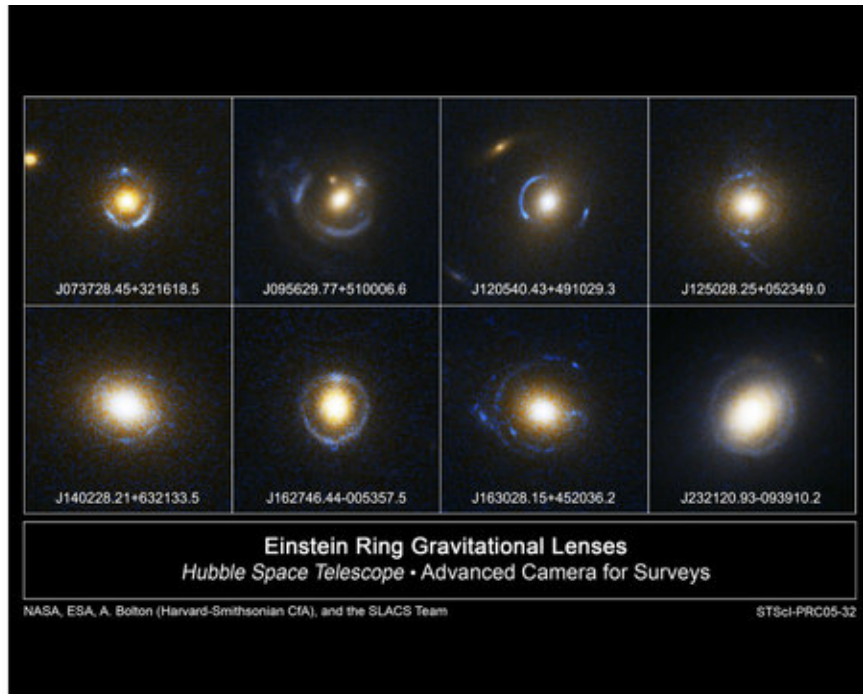


Figure 3 – Examples of Einstein rings taken with the HST. The images were taken between August 2004 and March 2005 by the Hubble telescope's Advanced Camera for Surveys. (NASA, 2005)

The extreme phenomena mentioned above are examples of “strong gravitational lensing”. For them, the lensing phenomenon is readily detectable in individual sources. In general, tidal gravitational fields lead to differential deflection of light bundles, and the size and shape of their cross sections are therefore changed. Since photons are neither emitted nor absorbed in the process of gravitational light deflection, surface brightness of sources remains unchanged. However, changing the cross section of a light bundle does change the flux observed from a source, and the different images in a multiple-image system generally will have different fluxes.

“Weak gravitational lensing” is characterized by weak distortions and small magnifications. For example, an extended circular source may be weakly distorted into an elliptical image. If all galaxies were circular, these small distortions could be measured on

individual images as well. However, background galaxy sources are not circular and the intrinsic ellipticity of galaxies is typically unknown and usually much greater than the gravitational shear distortion. Thus, weakly lensed images are useful in a statistical sense averaging over a large ensemble of background galaxy sources whose intrinsic orientation is largely random. The weak gravitational distortion will impose a coherent alignment of the images which is measurable, provided the distortion is larger than $\sim\sigma_\epsilon/\sqrt{N}$, where σ_ϵ is the intrinsic rms ellipticity of the background galaxies, and N is the number of images from which their shear is measured. The accuracy with which the average distortion over a small solid angle can be measured therefore depends on the number density of sources for which the shape measurement can be carried out.

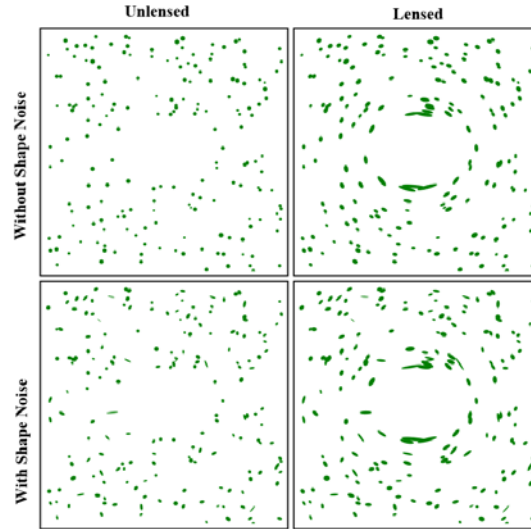


Figure 4 – Distortions of the type produced by weak lensing, acting on circles and a distribution of ellipses more similar to that of real galaxies. The distortion shown here is greatly exaggerated relative to real astronomical systems. Without shape noise, the lensed shapes of galaxies (upper right) would immediately yield knowledge of the gravitational shear. More realistically, galaxies come pre-equipped with intrinsic elliptical shapes. In this latter case, the lensed shapes of individual galaxies (lower right) cannot be used to determine the gravitational shear when the original galaxy shapes are unknown.

“Shapenoise” © TallJimbo 2008. From [Wikimedia Commons](#).

Copyleft: This is a free work, you can copy, distribute, and modify it under the terms of the [Free Art License](#).

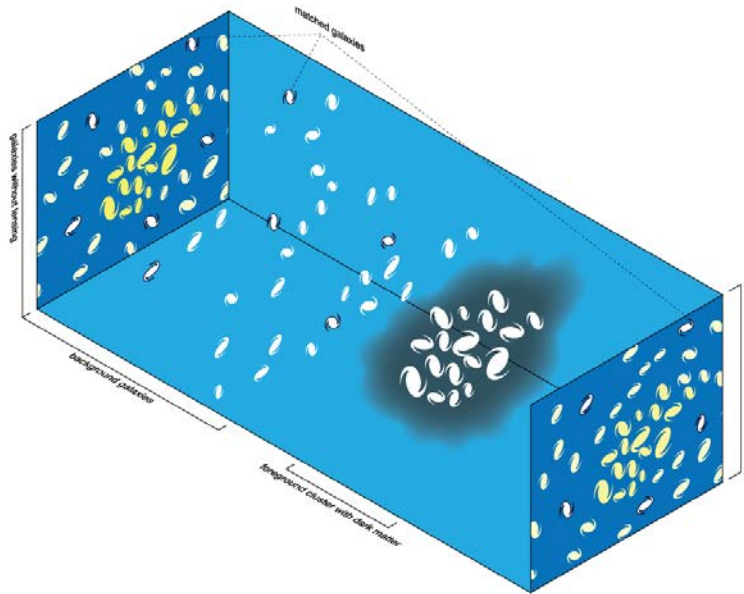


Figure 5 – The effects of foreground galaxy cluster mass on background galaxy shapes. The upper left panel shows (projected onto the plane of the sky) the shapes of cluster members (in yellow) and background galaxies (in white), ignoring the effects of weak lensing. The lower right panel shows this same scenario, but includes the effects of lensing. The middle panel shows a 3-d representation of the positions of cluster and source galaxies, relative to the observer. Note that the background galaxies appear stretched tangentially around the cluster.

“Gravitational-lensing-3d” © Sachs, Michael 2008. From [Wikimedia Commons](#).

Copyright: This is a free work, you can copy, distribute, and modify it under the terms of the [Free Art License](#).

3.2. Applications of Weak Lensing

Gravitational lensing has developed into a versatile tool for observational cosmology for two primary purposes: 1) to investigate the nature and distribution of dark matter in the universe, and 2) as a probe of the geometry of the Universe.

Concerning non-relativistic matter, the gravitational field depends on neither the nature of matter nor on its physical state. Light deflection probes the total matter density without distinguishing between ordinary baryonic or dark matter. Gravitational lensing is therefore a powerful probe for dark matter distributions in the Universe. While lensing measurements on their own cannot determine the origin or nature of dark matter, it can be useful for deducing the geometry of dark matter distributions in the Universe, which can be tested against other dark matter theories. As an extreme example, we are confident that compact dark-matter objects, such as black holes or brown dwarfs, cannot be overly abundant in the Universe as they would lead to unobserved lensing effects.

Weak lensing can be readily observed in the vicinity of strong lensing, since around a strong lensing sample the gravitational distortion will eventually become “weak”, or in a blank field of distant galaxies, where weak lensing is caused by a cosmological shear signal owed to the geometry of the Universe. In order to obtain three-dimensional geometry from lensing measurements, accurate information about the shear signal as a function of redshift is required. On the theoretical side, the large-scale geometry of the Universe is determined by gravitational theory and the cosmological model. Large scale lensing observations can provide observational tests and constraints for such models.

We offer a brief list some other applications of weak lensing below. For a more complete review of lensing applications, see for example (Matthias Bartelmann, 2001).

- Distortion of image shapes can be used to determine the local tidal gravitational field of a cluster. This information can be used to construct 2-D projected mass maps of clusters.

- Statistical mass distributions of galaxies can be obtained from galaxy-galaxy lensing
- Larger-scale mass distributions in the Universe affects observations of galaxy shapes and clusters of background sources, as well as the statistical properties of the CMB
- WL can be used to construct a mass-selected sample of clusters of galaxies, making use only of their tidal gravitational field which leaves an imprint on the image shapes of background galaxies.
- Redshift distribution of these faint and distant galaxies can be derived from lensing itself, well beyond the magnitude limit which is currently available through spectroscopy

3.3. Weak Lensing Theory

A typical situation considered in gravitational lensing is sketched in Figure 8, where light is deflected by a single mass distribution at redshift z_d , or angular diameter distance D_d , distorting the light rays coming from a source at redshift z_s , or angular diameter distance D_s to be seen at position θ . Without the intervening mass distribution, the source would be seen at an angular position β . If there are no other deflectors close to the line-of-sight, and if the size of the deflecting mass is small compared to both the distance from source to deflector and the deflector to the observer, then the actual light rays which are in reality smoothly curved in the region near the deflector can be replaced to by straight light rays with a sharp “kink” near the deflector. This kink is described the *deflection angle* $\hat{\alpha}$.

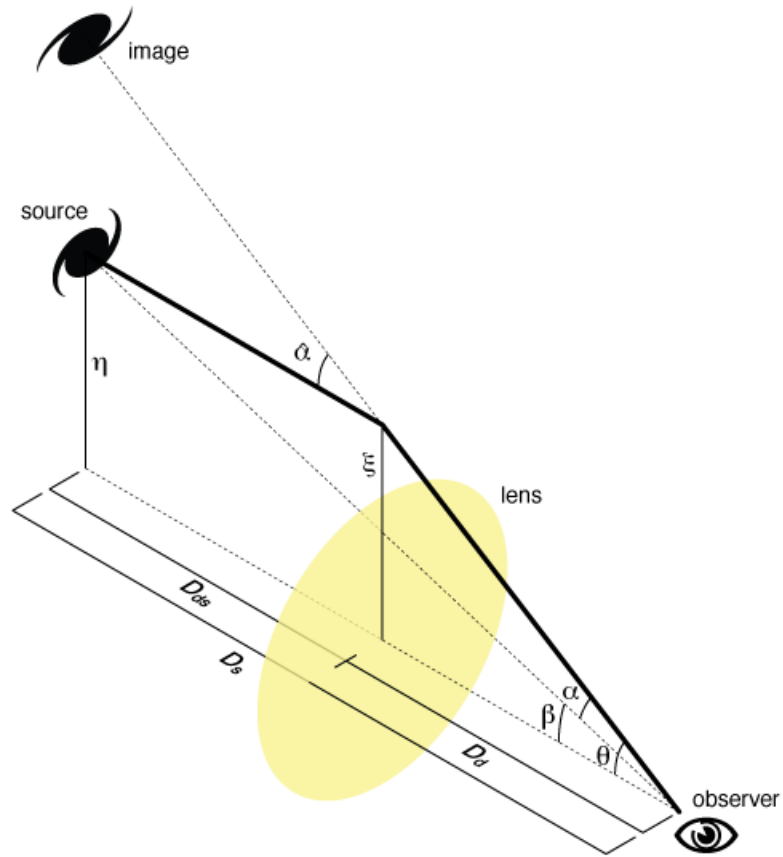


Figure 6 – Angles involved in a thin gravitational lens system (where the distances between the source, lens, and observer are much larger than the size of the lens). In the figure, D_{ds} is the angular diameter distance from the lens to the source, D_s is the angular diameter distance from the observer to the source, and D_d is the angular diameter distance from the observer to the lens.

“Gravitational Lensing Angles” © Sachs, Michael 2008. From [Wikimedia Commons](#).

Copyright: This is a free work, you can copy, distribute, and modify it under the terms of the [Free Art License](#).

In the simplest case of deflection by a point mass M , assuming the light ray does not propagate through the strong gravitational field close the event horizon of the point mass, General Relativity predicts that the deflection angle $\hat{\alpha}$ is

$$\hat{\alpha} = \frac{4GM}{c^2\xi} \quad [43]$$

This is twice the value obtained in Newtonian gravity, and under the condition that $\xi \gg R_S$, where R_S is the Schwarzschild radius of the lens, the deflection angle will be small, $\hat{\alpha} \ll 1$.

Under the condition of weak gravitational fields, the field equations of General Relativity can be linearized and the deflection angle of a distribution of mass is then the vectorial sum of the deflections due to individual masses. Consider a three-dimensional mass distribution with volume density $\rho(\vec{r}) = dm/dV$, and let a light ray propagating along the z -direction pass this mass distribution whose spatial trajectory we describe by (ξ_1, ξ_2, z) . The actual light ray is deflected, but if the deflection angle is small, it can be approximated as a straight line in the vicinity of the deflecting mass. This corresponds to the Born approximation in atomic and nuclear physics. The impact vector of the light ray relative to the mass element dm at a location $\vec{r} = (\xi'_1, \xi'_2, z')$ is just $\vec{\xi} - \vec{\xi}'$, where $\vec{\xi} = (\xi_1, \xi_2)$ is just a two-dimensional vector, independent of z . The total deflection angle is then

$$\hat{\vec{\alpha}}(\vec{\xi}) = \frac{4G}{c^2} \sum dm(\xi'_1, \xi'_2, z') \frac{\vec{\xi} - \vec{\xi}'}{|\vec{\xi} - \vec{\xi}'|^2} \quad [44]$$

Which is also a two-dimensional vector. Since $dm = \rho(\vec{r})dV = \rho(\vec{r})d^2\xi'dz'$, we can write this as

$$\hat{\alpha}(\vec{\xi}) = \frac{4G}{c^2} \int d^2\xi' \int dz' \rho(\xi'_1, \xi'_2, z') \frac{\vec{\xi} - \vec{\xi}'}{|\vec{\xi} - \vec{\xi}'|^2} \quad [45]$$

Since $\vec{\xi} - \vec{\xi}'$, and thus the last factor in equation [45], is independent of z' , the z' integration can be carried by defining the *surface mass density*

$$\Sigma(\vec{\xi}) = \int dz \rho(\xi_1, \xi_2, z) \quad [46]$$

Which is the mass density projected onto a plane perpendicular to the incoming light ray. The deflection angle then becomes

$$\hat{\alpha}(\vec{\xi}) = \frac{4G}{c^2} \int d^2\xi' \Sigma(\vec{\xi}') \frac{\vec{\xi} - \vec{\xi}'}{|\vec{\xi} - \vec{\xi}'|^2} \quad [47]$$

To reiterate, this expression is valid as long as the deviation of the actual light ray from a straight undeflected line within the region of the mass distribution is small compared to the scale on which the mass distribution changes significantly. This condition is satisfied in most astrophysically relevant situations (i.e., lensing by galaxies and clusters of galaxies), unless the deflecting mass extends all the way from the source to the observer.

Now, referring again to Figure 8, let $\vec{\eta}$ denote the two-dimensional position of the source on the source plane. Then, recalling the definition of angular diameter distance,

$$\vec{\eta} = D_s \vec{\theta} - D_{ds} \hat{\alpha}(\vec{\xi}) \quad [48]$$

We can also write that $\vec{\eta} = D_s \vec{\beta}$ and $\vec{\xi} = D_d \vec{\theta}$. Rearranging equation [48] in terms of $\vec{\beta}$, we get

$$\vec{\beta} = \vec{\theta} - \frac{D_{ds}}{D_s} \hat{\alpha}(D_d \vec{\theta}) \quad [49]$$

Defining the scaled deflection angle as

$$\vec{\alpha}(\vec{\theta}) = \frac{D_{ds}}{D_s} \hat{\alpha}(D_d \vec{\theta}) \quad [50]$$

we can now write

$$\vec{\beta} = \vec{\theta} - \vec{\alpha}(\vec{\theta}) \quad [51]$$

The interpretation of the lens equation [51] is that a source with true position $\vec{\beta}$ can be seen by an observer at angular position $\vec{\theta}$ satisfying [51]. The scaled deflection angle $\vec{\alpha}(\theta)$ depends on the observed angular position $\vec{\theta}$ of the light ray, and on the mass distribution according to [47] and [50]. All of these distances are to be interpreted as angular-diameter distances, and they depend, for a given source and lens redshift, on the cosmological model. If [51] has more than one solution for fixed $\vec{\beta}$, a source at $\vec{\beta}$ has images at several positions on the sky and the lens produces multiple images. For this to happen, the lens must be “strong” in the sense that the surface mass density [46] is larger than a “critical mass density”

$$\Sigma_{cr} = \frac{c^2}{4\pi G} \frac{D_s}{D_d D_{ds}} \quad [52]$$

If a mass distribution has $\Sigma \geq \Sigma_{cr}$, then it produces multiple images, and thus Σ_{cr} acts as a characteristic value for the surface mass density to distinguish between “weak” and “strong” lenses. With Σ_{cr} , we also define the dimensionless surface mass density

$$\kappa(\vec{\theta}) = \frac{\Sigma(D_d \vec{\theta})}{\Sigma_{cr}} \quad [53]$$

In terms of κ , a strong lens is characterized by $\kappa \geq 1$, and the scaled deflection angle can be written as

$$\vec{\alpha}(\vec{\theta}) = \frac{1}{\pi} \int d^2\theta' \kappa(\vec{\theta}') \frac{\vec{\theta} - \vec{\theta}'}{|\vec{\theta} - \vec{\theta}'|^2} \quad [54]$$

Equation [54] implies that $\vec{\alpha}$ is a conservative vector field in that it can be written as the gradient of a scalar *deflection potential*,

$$\psi(\vec{\theta}) = \frac{1}{\pi} \int d^2\theta' \kappa(\vec{\theta}') \ln|\vec{\theta} - \vec{\theta}'| \quad [55]$$

as $\vec{\alpha} = \nabla\psi$. The potential function $\psi(\vec{\theta})$ can be viewed as a two-dimensional analogue of the Newtonian gravitational potential and satisfies the Poisson equation with the two-dimensional surface mass density, $\nabla^2\psi = 2\kappa(\vec{\theta})$.

The solutions $\vec{\theta}$ of the lens equation [51] yield the angular positions of the images of a source at $\vec{\beta}$. Because light bundles are deflected differentially, the shapes of the images will be distorted from that of the source. An extreme example of this distortion is the occurrence of giant luminous arcs in strong lensing galaxy clusters. Since photons are neither emitted nor absorbed in gravitational light deflection, lensing distortions conserve surface brightness. Hence, if $I^{(s)}(\vec{\beta})$ is the source surface brightness distribution in the source plane, then the observed surface brightness distribution in the lens plane as a function of the observable position of the image $\vec{\theta}$ is

$$I(\vec{\theta}) = I^{(s)}[\vec{\beta}(\vec{\theta})] \quad [56]$$

In general, the shape of the images must be determined by solving the lens equation for all points within an extended source, but the situation simplifies somewhat in the case of weak lensing. If the size of the source is much smaller than the characteristic angular scale of the deflector, one can locally linearize the lens mapping. The first order image distortion is then described by the Jacobian of the lens equation

$$\mathcal{A}(\vec{\theta}) = \frac{\partial \vec{\beta}}{\partial \vec{\theta}} = \left(\delta_{ij} - \frac{\partial^2 \psi(\vec{\theta})}{\partial \theta_i \partial \theta_j} \right) = \begin{pmatrix} 1 - \kappa - \gamma_1 & -\gamma_2 \\ -\gamma_2 & 1 - \kappa + \gamma_1 \end{pmatrix} \quad [57]$$

where κ is the dimensionless surface mass density [53], related to ψ through Poisson's equation, and we have introduced the components of the shear γ as

$$\gamma_1 = \frac{1}{2}(\psi_{,11} - \psi_{,22}), \quad \gamma_2 = \psi_{,12} \quad [58]$$

The shear is to be defined as a complex quantity with the components γ_i as the real and imaginary parts of γ : $\gamma \equiv \gamma_1 + i\gamma_2 = |\gamma|e^{2i\phi}$. Thus, if $\vec{\theta}_o$ is a point within an image, corresponding to the point $\vec{\beta}_o = \vec{\beta}(\vec{\theta}_o)$ within the source, we find from [56] that to first linear order, the distortion of the image surface brightness distribution is

$$I(\vec{\theta}) = I^{(s)}[\vec{\beta}_o + \mathcal{A}(\vec{\theta}_o) \cdot (\vec{\theta} - \vec{\theta}_o)] \quad [59]$$

According to this mapping, the shapes of circular sources are mapped to elliptical images. The ratios of the semi-axes of such an ellipse to the radius of the original circular source are given by the inverse of the eigenvalues of the Jacobian matrix, which are $1 - \kappa \pm |\gamma|$. The fluxes observed from the image and from the unlensed source are given by integrals over the brightness distributions $I(\vec{\theta})$ and $I^{(s)}(\vec{\beta})$, respectively. The ratio of the fluxes is defined as the *magnification* $\mu(\vec{\theta}_o)$. From [59], the magnification is then just the ratio of the solid angles subtended by an image and the unlensed source, which is given by the inverse of the determinant of \mathcal{A} ,

$$\mu = \frac{1}{\det \mathcal{A}} = \frac{1}{(1 - \kappa)^2 - |\gamma|^2} \quad [60]$$

Giant arcs are obtained at places where one of the eigenvalues of \mathcal{A} is close to zero, i.e., where $\mu \gg 1$.

The images are thus distorted in shape and size by the Jacobian \mathcal{A} . The shape distortion is due to the tidal gravitational field, described by the shear γ , whereas the magnification described by μ is caused by both isotropic focusing caused by the local matter density and anisotropic focusing caused by shear.

The Jacobian matrix of the lens equation can be further reduced in terms of more measureable quantities in form

$$\mathcal{A}(\vec{\theta}) = (1 - \kappa) \begin{pmatrix} 1 - g_1 & -g_2 \\ -g_2 & 1 + g_1 \end{pmatrix} \quad [61]$$

In this version of \mathcal{A} , the shape distortion of images is described solely by the (complex) reduced shear, defined as

$$g = \frac{\gamma}{1 - \kappa}, \quad g = g_1 + ig_2 = |g|e^{2i\varphi} \quad [62]$$

The amplitude of g describes the degree of distortion, whereas its phase φ yields the direction of distortion. The factor of “2” is present in the phase to account for the fact that an ellipse transforms into itself after a rotation by 180° . The pre-factor $(1 - \kappa)$ only affects the size, but the not the shape of the images.

3.4. Weak Lensing Strategy

If an ensemble of faint and distant galaxies are observed through the gravitational lens of deflector, the appearance of said galaxies are changed. The tidal shear components of the gravitational field distort the shapes of galaxies, and the magnification associated with gravitational light deflection changes their apparent brightness. If all galaxies were intrinsically circular, the measured ellipticity of galaxy images would immediately yield information on the local tidal gravitational field. However, galaxies are not intrinsically circular and the intrinsic ellipticity of distant galaxies is generally unknown, making the extraction of significant

information from individual galaxies impossible, expect perhaps for giant luminous arcs whose distortion is so extreme that gravitation field information can still be easily determined.

The strategy nevertheless, is to assume that galaxies are intrinsically randomly oriented so that the strength of the tidal gravitational field can be inferred from a sample of galaxy images, provided the average ellipticity signal of the sample is larger than the Poisson noise caused by the finite number of galaxy images in the sample and by the intrinsic ellipticity distribution. The average intrinsic ellipticity over a large enough sample can then be assumed to go to zero, since we expect no direction to be singled out in the Universe,

$$\langle \epsilon_{int} \rangle = 0 \quad [63]$$

The Poisson shape noise due to intrinsic ellipticity dispersion reduces as $\sigma_{meas} \propto \frac{\sigma_{\epsilon}}{N}$, where N is the size of the sample, and the average measured ellipticity over a sufficiently large sample then serves as a good estimate of the average shear signal,

$$\langle \epsilon_{meas} \rangle = \langle \epsilon_{shear} \rangle \text{ for large } N \quad [64]$$

The weak lensing measurement problem then reduces to finding an estimation of the average measured ellipticity of an ensemble of galaxies. If a galaxy had elliptical isophotes, its shape and size could simply be defined in terms of the axis ratio and area enclosed by a boundary isophotes. However, the shapes of faint galaxies can be irregular and not well approximated by ellipses. Additionally, galaxy images are given in terms of pixel brightness on CCDs. What is required then is a definition of size and shape which accounts for the irregularity of images, and which is well adapted to observational data.

Let $I(\vec{\theta})$ be the surface brightness of a galaxy image at angular position $\vec{\theta}$. Let us assume the galaxy is isolated, so that I can be measured to large angular separations from the center of the image, $\vec{\bar{\theta}}$, which we define by

$$\vec{\bar{\theta}} = \frac{\int d^2\theta q_I[I(\vec{\theta})]\vec{\theta}}{\int d^2\theta q_I[I(\vec{\theta})]} \quad [65]$$

where $q_I[I(\vec{\theta})]$ is a suitably chosen weight function. For example, if $q_I[I(\vec{\theta})] = I$, then $\vec{\bar{\theta}}$ represents the “center of light”, in the same way the center of mass is defined in a mass distribution. Alternatively, if $q_I = I(\theta)H(I - I_{th})$, where H is the Heaviside step function and I_{th} is some threshold intensity, then $\vec{\bar{\theta}}$ is the center of the area enclosed by a limiting isophote with $I = I_{th}$. For a given choice of $q_I(I)$, the tensor of second brightness moments is defined by,

$$Q_{ij} = \frac{\int d^2\theta q_I[I(\vec{\theta})](\theta_i - \bar{\theta}_i)(\theta_j - \bar{\theta}_j)}{\int d^2\theta q_I[I(\vec{\theta})]}, \quad i, j \in \{1, 2\} \quad [66]$$

In defining equation [65] and [66], the weight function $q_I(I)$ is presumably chosen so that the integrals converge. For an image with circular isophotes, $Q_{11} = Q_{22}$, and $Q_{12} = 0$. The trace of Q describes the size of the image, and the traceless part of Q_{ij} contains information about the ellipticity of the image. For example, the size can be defined by

$$\omega \equiv (Q_{11}Q_{22} - Q_{12}^2)^{1/2} \quad [67]$$

The shape of the image can be quantified by two complex ellipticities,

$$\chi = \frac{Q_{11} - Q_{22} + 2iQ_{12}}{Q_{11} + Q_{22}}, \quad \epsilon \equiv \frac{Q_{11} - Q_{22} + 2iQ_{12}}{Q_{11} + Q_{22} + 2(Q_{11}Q_{22} - Q_{12}^2)^{1/2}} \quad [68]$$

Both of these ellipticities have the same phase (because of the same numerator), but different absolute value. For an image with elliptical isophotes of axis ratio $r \leq 1$, one obtains

$$|\chi| = \frac{1-r^2}{1+r^2}, \quad |\epsilon| = \frac{1-r}{1+r} \quad [69]$$

Depending on the context, χ or ϵ may be the more convenient ellipticity to consider. The two ellipticities are related to each other via the transformations,

$$\epsilon = \frac{\chi}{1 + (1 - |\chi|^2)^{1/2}}, \quad \chi = \frac{2\epsilon}{1 + |\epsilon|^2} \quad [70]$$

If we define the center of a source $\vec{\beta}$ as,

$$\vec{\beta} = \frac{\int d^2\beta q_l[I(\vec{\beta})]\vec{\beta}}{\int d^2\beta q_l[I(\vec{\beta})]} \quad [71]$$

then in total analogy, for the shape of a galaxy source we define the second-moment brightness tensor $Q_{ij}^{(s)}$ and source ellipticity $\epsilon^{(s)}$,

$$Q_{ij}^{(s)} = \frac{\int d^2\beta q_l[I(\vec{\beta})](\beta_i - \bar{\beta}_i)(\beta_j - \bar{\beta}_j)}{\int d^2\beta q_l[I(\vec{\beta})]}, \quad i, j \in \{1, 2\} \quad [72]$$

and

$$\epsilon^{(s)} \equiv \frac{Q_{11}^{(s)} - Q_{22}^{(s)} + 2iQ_{12}^{(s)}}{Q_{11}^{(s)} + Q_{22}^{(s)} + 2(Q_{11}^{(s)}Q_{22}^{(s)} - Q_{12}^{(s)2})^{1/2}} \quad [73]$$

The lens equation relates the tensors Q_{ij} and $Q_{ij}^{(s)}$ by

$$Q^{(s)} = \mathcal{A}Q\mathcal{A}^T = \mathcal{A}Q\mathcal{A} \quad [74]$$

where $\mathcal{A} \equiv \mathcal{A}(\vec{\theta})$ is the Jacobian matrix of the lens equation at position $\vec{\theta}$. The size of a galaxy image, defined by equation [67], relative to the size of the corresponding source is related by

$$\omega = \mu(\vec{\theta})\omega^{(s)} \quad [75]$$

The complex ellipticities of source relative to image then transform as

$$\epsilon^{(s)} = \begin{cases} \frac{\epsilon - g}{1 - g^* \epsilon}, & \text{if } |g| \leq 1 \\ \frac{1 - g^* \epsilon}{\epsilon^* - g^*}, & \text{if } |g| > 1 \end{cases} \quad [76]$$

where the asterisk denotes complex conjugation, and g is the reduced shear defined by equation [62]. The inverse transformations are obtained by interchanging source and image ellipticities, and $g \rightarrow -g$ in [76].

For the case of weak lensing, $\kappa \ll 1$, $\gamma \ll 1$, and thus so too is the reduced shear $g \ll 1$.

Then, [76] simply becomes

$$\epsilon^{(s)} \approx \begin{cases} \epsilon - g, & \text{if } |g| \leq 1 \\ \frac{1}{\epsilon^* - g^*}, & \text{if } |g| > 1 \end{cases} \quad [77]$$

or, inverting,

$$\epsilon \approx \begin{cases} \epsilon^{(s)} + g, & \text{if } |g| \leq 1 \\ \frac{1}{\epsilon^{(s)*} + g^*}, & \text{if } |g| > 1 \end{cases} \quad [78]$$

Given the assumption that the intrinsic orientation of galaxies is random, the expectation values of the source ellipticity vanishes,

$$\langle \epsilon^{(s)} \rangle = 0 \quad [79]$$

This assumption is not generally challenged since the faint galaxies used for weak lensing typically come from a large range of redshifts, and so most of them are not physically related and their ellipticities are not expected to be correlated. This then implies that the expectation value of the image ellipticity ϵ , obtained by averaging the transformation law [78] over the intrinsic source orientation, is then

$$\langle \epsilon \rangle \approx \begin{cases} g, & \text{if } |g| \leq 1 \\ \frac{1}{g^*}, & \text{if } |g| > 1 \end{cases} \quad [80]$$

This is the seminal result of all the theoretical work discussed in this section. It shows that the image ellipticity provides an unbiased estimate of the local shear, albeit a noisy one. The noise is determined by the intrinsic dispersion

$$\sigma_\epsilon = \sqrt{\langle \epsilon^{(s)} \epsilon^{(s)*} \rangle} \quad [81]$$

in the sense that when averaging over an ensemble of N galaxy images all distorted by the same reduced shear, the $1\text{-}\sigma$ deviation of the mean ellipticity from the true shear is σ_ϵ/N . The strategy of weak lensing measurement then, is to beat down this noise by averaging over many galaxy images. Of course, the physical region in the Universe over which the shear can be considered roughly constant is limited, so the averaging over galaxy images is always related to smoothing of the shear. The accuracy of a shear estimate thus depends on the local number density of galaxies for which a shape can be measured. In order to obtain high number density, deep imaging observations are required.

3.5. Tangential and Cross Components of the Shear

The shear components γ_1 and γ_2 in equation [57] are defined relative to a Cartesian coordinate reference frame. However, it is often useful to consider the shear components in a rotated reference frame. For example, arcs in a galaxy cluster will be tangentially aligned, and so their ellipticity angle will be oriented tangent to the radial vector in the cluster. We thus define the tangential and cross components of the shear as follows:

Let ϕ specify a direction. Then the tangential and cross components of shear relative to this direction are defined as

$$\gamma_t = -\text{Re}[\gamma e^{-2i\phi}], \quad \gamma_x = -\text{Im}[\gamma e^{-2i\phi}] \quad [82]$$

For example, in the case of a circularly-symmetric matter distribution, the shear at any point will be oriented tangent to the radial direction pointing towards the center of symmetry. If ϕ represents the polar angle of a point, $\gamma_x = 0$. Tangential and cross components of ellipticity, ϵ_t and ϵ_x , are defined in complete analogy to the components of the shear. A positive tangential ellipticity value implies that the image is oriented in the tangent direction; i.e., the major axis is aligned tangentially. A negative tangential ellipticity value implies that the image is oriented in the radial direction; i.e., the minor axis is aligned tangentially.

In the case of an axisymmetric mass distribution, the tangential shear is related to the dimensionless surface mass density $\kappa(\theta)$ at a radius θ and the mean surface mass density $\bar{\kappa}(\theta)$ inside the radius θ by $\gamma_t = \bar{\kappa} - \kappa$ (Schneider, 1999). For more general matter distributions, a remarkably similar expression holds:

$$\langle \gamma_t \rangle = \bar{\kappa} - \langle \kappa \rangle \quad [83]$$

where $\langle \kappa(\theta) \rangle$ and $\langle \gamma_t(\theta) \rangle$ denote the mean surface mass density and mean tangential shear on the circle of radius θ . Thus, the mean tangential shear at some radial distance θ relative to a point is equal to the mean enclosed surface mass density at θ .

As a reminder, the dimensionless surface mass density is defined by equation [53].

Restoring the units, the normal mean surface mass density Σ inside a radius θ is thus gotten by

$$\langle \Sigma(\theta) \rangle = \Sigma_{cr} \langle \kappa(\theta) \rangle = \frac{c^2}{4\pi G} \frac{D_s}{D_d D_{ds}} \langle \gamma_t \rangle \quad [84]$$

where Σ_{cr} is the critical surface mass density defined in equation [52]. The encircled mass is obtained from this density by multiplying through by circular area, $A = \pi r^2 = \pi (D_d \theta)^2$:

$$M(< D_d\theta) = \frac{c^2}{4G} \frac{D_d D_s}{D_{ds}} \langle \gamma_t \rangle \theta^2 \quad [85]$$

3.6. Weak Lensing Measurement

Real astronomical data used for weak lensing are supplied by charge-coupled device (CCD) images from modern telescopes. The steps from CCD frames to a set of galaxy images with measured shapes can broadly be grouped into four categories: data reduction, image detection, shape determination, and corrections for the point-spread function. The data-reduction process is fairly well standardized and involves de-biasing, flat-fielding, and removal of cosmic rays and bad pixels (Bartelmann & Schneider, 1999). For our project, galaxy data is collected from publicly available scientific UltraVISTA catalogs and dithered HST images. As such, the data reduction has already been performed by the groups that release said data.

To detect galaxies and measure their shapes, care must be taken to avoid overlapped images. Since weak lensing observations require large number densities, overlapping galaxy images are a legitimate concern. Whether a detected object is a single galaxy or a merged galaxy pair will greatly impact the shape measurement. In addition, images are noisy owing to a finite number of photons per pixel and to the intrinsic noise in the CCD electronics. Thus, a local enhancement of counts needs to be classified as a statistically significant source detection, and a conservative signal-to-noise threshold reduces the number of galaxy images. Stars also need to be identified and distinguished from galaxy images. The measured shape of stars, treated as point source objects, reflect the shape profile of the PSF and should not be counted in the average ellipticity signal that is used to estimate the reduced shear. If the field to be studied is far from the Galactic plane, however, the number density of stars will be correspondingly small.

Several data-analysis software packages exist for the detection and measurement of galaxy images, for example, the popular Source Extractor (SExtractor) software (Bertin &

Arnouts, 1996). SExtractor provides automated routines to detect, deblend, measure and classify sources from astronomical images. Star and galaxy separation are handled by the software using a neural network trained with simulated images. Given SExtractor's ability to deal with large digital images (up to $60,000 \times 60,000$ pixels), and to deal with a wide variety of object shapes and magnitudes, the software is well suited for the analysis of large extragalactic surveys such as the HST Frontier Fields that will be considered in this study.

Once an object is identified, the quadrupole moments can be obtained from equation [66]. The weight function q_I in [66] should ideally be chosen so that it vanishes for surface brightnesses close to and smaller than the sky brightness, otherwise one risks sampling too much noise. If, on the other hand, q_I is cut off at too bright values of I , the area within the measured quadrupole moments are at risk of being too small and the effects of seeing can become overwhelming. Too conservative of a cut-off will also decrease the measured galaxy counts.

SExtractor uses a weight in form of $q_I = I(\theta)H(I - I_{th})$ for the measurement of object centroids and multipole moments, where I_{th} is some threshold intensity to be input by the user, ideally close to but a few σ_{noise} above the sky background. The quadrupole moments SExtractor outputs are then measured inside the resulting limiting isophote. However, we note that while this scheme is automated by SExtractor and requires minimal human intervention, the limiting isophote being close to the sky background necessarily results in a shape that is affected by sky noise. This implies that the measured quadrupole moments and the ellipticities calculated thereof will depend non-linearly on the CCD brightness, and the effect of noise will enter these values in a non-linear fashion.

A more robust measurement of the multipole moments, favored by the lensing community, is a weight function of the form $q_I[\vec{\theta}] = I(\vec{\theta})W(\vec{\theta})$, where $W(\vec{\theta})$ explicitly

depends on $\vec{\theta}$. This allows more control over the shape measurement, for example, by tuning $W(\vec{\theta})$ to the scale on which the object was detected at highest significance. The tradeoff is that the use of an angle dependent weight function results in quadrupole moments that do not obey the linear transformation law [74]. Equation [80] then no longer holds and the expectation value of the ellipticity $\langle\epsilon\rangle$ will necessarily be different from the reduced shear g . The actual relation between the mean ellipticity and reduced shear will depend on the choice of $W(\vec{\theta})$. Detailed simulations can be performed to calibrate an approximate correction factor f to fit an approximate relation $g \approx f\langle\epsilon\rangle$ for some given choice of $W(\vec{\theta})$. However, relying on simulated images to calibrate the new relation is not fully satisfactory since the results will necessarily depend on the assumptions underlying the simulation (Bartelmann & Schneider, 1999).

In either case, in order to obtain an estimate of the reduced shear from observed galaxy shapes, one must also deal with the telescope PSF, which mathematically can be described as a convolution of the source intensity profile and a function $P(\vec{\theta})$:

$$I^{(obs)}(\vec{\theta}) = \int d^2\phi I(\vec{\theta})P(\vec{\theta} - \vec{\phi}) \quad [86]$$

where $P(\vec{\theta})$ is the PSF describing the brightness distribution of a point source on the CCD, normalized to unity and centered at $\vec{0}$. The characteristic width of the PSF is called the size of the seeing disc and the smaller it is, the less smeared the images are. Weak lensing studies require a high number density of galaxy images, which requires observations to be extended to faint magnitudes. This puts a strong requirement on the telescopes that are suitable for weak lensing observations, which require a seeing well below 1 arcsecond (Bartelmann & Schneider, 1999). Ideally, the telescope should have a small and temporally stable PSF, and the shape of $P(\vec{\theta})$

needs to be known to a high degree of detail in order to accurately extract the shape of source galaxies from observed galaxy images.

The PSF includes effects of atmosphere as well as pointing errors of the telescope. Therefore, the PSF can be slightly anisotropic. The isotropic part of the PSF will cause small elliptical images to become rounder, thereby diluting the ellipticity signal. The anisotropic part of the PSF introduces a systematic, spurious image ellipticity. Generally, the PSF may vary across the FoV of the detector. If the number density of stars is large enough, the PSF variation across the field can be estimated by their images since the shapes of stars, which serve as point sources, reflects the PSF. However, the PSF as measured by the images of stars is not necessarily the same as the PSF which applies to galaxies, due to their different spectra and the chromaticity of the PSF. Nevertheless, it is usually assumed that the PSF measured from stellar images adequately represents the PSF for galaxies.

In the idealized case where the quadrupole moments are defined with the weight function $q_I(I) = I$, the effect of the PSF on the observed image ellipticities is fairly straightforward. A quadrupole tensor P_{ij} can be defined for the PSF in complete analogy to [66] for the quadrupole tensor of a galaxy intensity profile. Then, the observed quadrupole moments $Q_{ij}^{(obs)}$ are related to the source Q_{ij} by (Bartelmann & Schneider, 1999)

$$Q_{ij}^{(obs)} = P_{ij} + Q_{ij} \quad [87]$$

The galaxy source ellipticity χ then transforms as

$$\chi^{(obs)} = \frac{\chi + T\chi^{(PSF)}}{1 + T} \quad [88]$$

where

$$T = \frac{P_{11} + P_{22}}{Q_{11} + Q_{22}} \quad [89]$$

and

$$\chi^{(PSF)} = \frac{P_{11} + P_{22} + 2iP_{12}}{P_{11} + P_{22}} \quad [90]$$

The quantity T thus represents the ratio of the PSF size to the image size before convolution, and $\chi^{(PSF)}$ is the PSF ellipticity defined in complete analogy to equation [68]. The smaller T , the closer $\chi^{(obs)}$ is to χ . In the limit of very large T , $\chi^{(obs)}$ approaches the PSF ellipticity. If the PSF is purely isotropic, then $\chi^{(PSF)} = 0$. Equation [88] can be inverted to obtain χ from $\chi^{(obs)}$, but this inversion is unstable unless T is sufficiently small, in the sense that the noise affecting the measurement of $\chi^{(obs)}$ is amplified by the inversion process. Stated another way, if the PSF, and thus also T , is too large, the image can become unresolved after convolution with the PSF and information about the source ellipticity χ is lost. It should also be noted that strictly speaking, these transformation laws only apply for the specific choice of the weight function. For other weighting schemes, such as $q_l(I) = IW(\theta)$ as mentioned above, the resulting transformation becomes much more complicated (Bartelmann & Schneider, 1999), but we won't go into all of the details here.

3.7. Our Objective

To summarize the observational requirements for an efficient weak lensing study:

- 1) The number density of objects for which a shape can be reliably measured should be as high as possible;

- 2) the mean redshift of the source population should be high to put a large fraction of them into the background of the lenses, and to average out local intrinsic ellipticity correlations;
- 3) the source population should be as round as possible to reduce the intrinsic ellipticity dispersion;
- 4) the ratio of the size of the telescope PSF and that of the source should be as small as possible;
- 5) the PSF anisotropy should be as small as possible;
- 6) the PSF must be controllable, to allow corrections for it;
- 7) for most applications, the field-of-view should be large to enhance the statistical significance of the results;
- 8) the background electromagnetic noise should be as low as possible.

Points 1), 4), and 8) are each necessarily wavelength dependent. There is a higher density of sources useful for weak lensing measurement at high redshift around NIR wavelengths, but the FWHM of telescope PSFs are also larger at long wavelengths. These factors tend to compete with one another, and one would expect a sort of balancing act that ultimately determines which wavelengths are long enough to maximize number density for the statistical performance of weak lensing, but not too long to where the PSF produces unresolved images that compromise the ability to perform accurate shape measurement. On top of all this, accurate shape measurements of the small, faint distant galaxy images will favor the strongest source signal and the lowest background noise. The background electromagnetic noise will itself be wavelength dependent with its own color profile.

Current weak lensing surveys are typically done by ground-based telescopes and mostly rely on background galaxy shape measurements at optical wavelengths. However, seeing through Earth's atmosphere complicates matters and limits the accuracy of said measurements. The telescope PSFs of ground-based telescopes are complicated by wind, weather, and other terrestrial factors. Equally important, or perhaps even more so, atmospheric absorption and emission of electromagnetic radiation limits the wavelength spectrum available for accurate shape measurement of background galaxies at long wavelengths for ground based surveys. The OH airglow of Earth's atmosphere at red and NIR wavelengths makes observations of very faint sources from the ground undesirable at these long wavelengths. Therefore, to expand the available wavelength spectrum available for weak lensing measurement, a weak lensing space mission is desired.

In the work that follows, we set out to identify the optimal wavelength bands to maximize weak lensing measurement performance in general. We approach this problem by performing calculations on simple galaxy and telescope models while accounting for the basic wavelength dependence of the factors mentioned above. To address point 3), we will model galaxies with circularly symmetric Sersic light profiles. To address points 5) and 6), will use a pure airy disk PSF to model an "ideal" diffraction-limited space telescope. And to address point 8) will consider our telescope in space with background noise dominated by the zodiacal light. More details on our methods and calculations follow in Chapter 4. We will also derive analytical Gaussian equations for the flux SNR and shape measurement variance under the assumption of Gaussian PSFs and Gaussian galaxy light profiles.

Finally, we perform a crude measurement of galaxy ellipticities in the six HST FPFs using Source Extractor (SExtractor) software (Bertin & Arnouts, 1996) in order to estimate a reduced

shear at the location of the parallel fields using the longest wavelength available in the HST FF data. In an effort to simplify the procedure, we assume a purely symmetric Gaussian PSF. While this choice is unrealistic and unrepresentative of the HST, it makes deconvolution of the PSF simple and allows for relatively easy extraction of an approximate galaxy source ellipticity signal. The average ellipticity among a significantly large density of distant galaxy images is directly related to reduced gravitational shear signal, which we approximate with our simplifying assumptions and use to estimate the primary FF galaxy cluster masses to illustrate that shear measurements at long NIR wavelengths are completely reasonable.

4. Methodology

In this chapter we outline the basic models for background galaxy shapes and a diffraction-limited space telescope to investigate the wavelength dependence of weak lensing shape measurements. We keep intact the wavelength dependence of background source signals, telescope PSF diffraction, and background noise assuming sky dominated noise from a diffraction-limited space telescope.

Real galaxy data is collected from existing surveys of the UltraVISTA field and Frontier Fields to construct reasonable collections of simple shaped galaxies assumed to be described completely by Sersic galaxy light profiles of Sersic index one or four. The telescope PSF is assumed to be perfectly described by an airy disk and convolved with the Sersic galaxy profiles to simulate collections of galaxy images. We then calculate the galaxy flux S/N, the shape measurement error, and the effective number density of sources from these collections as functions of wavelength.

We also perform a crude measurement of galaxy ellipticities in the HST FPFs using Source Extractor (SExtractor) software (Bertin & Arnouts, 1996) in order to estimate a reduced shear at

the location of the parallel fields. In an effort to simplify the procedure, we assume a purely symmetric Gaussian PSF. While this choice is unrealistic and unrepresentative of the HST, it makes deconvolution of the PSF simple and allows for relatively easy extraction of an approximate galaxy source ellipticity signal. The average ellipticity among a significantly large density of distant galaxy images is directly related to reduced gravitational shear signal, which we approximate with our simplifying assumptions and compare to other more strictly accurate values reported elsewhere in the literature.

4.1. Simple galaxy profile models

Sersic's equation gives the light intensity profile at an angular distance θ from the center of the galaxy as

$$I(\theta) = I_e \exp \left\{ -b_n \left[\left(\frac{\theta}{\theta_e} \right)^{\frac{1}{n}} - 1 \right] \right\} \quad [91]$$

where I_e is the intensity at the effective angular radius θ_e that encloses half of the total light for the model. The constant b_n is defined in terms of the Sersic index n which describes the "shape" of the light profile.

Setting $n = 4$ in Sersic's equation gives the de Vaucouleurs profile: $I(R) \propto e^{-k\theta^{1/4}}$, which is a good description of elliptical galaxies. Setting $n = 1$ gives the exponential profile: $I(R) \propto e^{-k\theta}$, which is a good description of spiral galaxies. An index of $n = \frac{1}{2}$ produces a Gaussian distribution. In general, larger values of the index n correlate to higher degrees of central light concentration. The constant b_n in equation [132] can be solved in terms of n using complete and incomplete gamma functions such that

$$\Gamma(2n) = 2\gamma(2n, b_n) \quad [92]$$

but an approximate analytical expression for $0.5 < n < 10$ was given by Graham & Driver (2005):

$$b_n = 1.9992n - 0.3271 \quad [93]$$

In the form of equation [132], the Sersic light intensity profile depends on the effective intensity I_e at the half-light radius. It is a simple matter to rewrite Sersic's equation in terms of the total flux of the galaxy instead. The total flux over an infinite projected area is obtained by integrating [132] over area out to infinite radius, $\theta \rightarrow \infty$:

$$F_{total} = \int_0^{\infty} I(\theta) 2\pi\theta d\theta \quad [94]$$

This integral can be straight-forwardly solved with the substitution $x = b_n \left[\frac{\theta}{\theta_e} \right]^{\frac{1}{n}}$, yielding

$$F_{total} = \pi I_e \theta_e^2 \frac{e^{b_n}}{(b_n)^{2n}} \Gamma(2n + 1)$$

Using the property of the gamma function, $\Gamma(x) = (x - 1)!$ for positive integers, the total flux becomes,

$$F_{total} = \pi I_e \theta_e^2 \frac{e^{b_n}}{(b_n)^{2n}} (2n)! \quad [95]$$

Inverting equation [95] to solve for the intensity at the half-light radius, I_e , in terms of the total flux F_{total} , we find

$$I_e = \frac{(b_n)^{2n}}{\pi e^{b_n} \theta_e^2 (2n)!} F_{total} \quad [96]$$

The Sersic light intensity profile in terms of F_{total} can then be obtained by plugging equation [96] for I_e back into equation [132]:

$$I(\theta) = \left[\frac{(b_n)^{2n}}{\pi e^{b_n} \theta_e^2 (2n)!} F_{total} \right] \exp \left\{ -b_n \left(\left[\frac{\theta}{\theta_e} \right]^{\frac{1}{n}} - 1 \right) \right\} \quad [97]$$

This is the Sersic light intensity equation expressed in terms of the total galaxy flux. Using equation [97], data from each galaxy referenced from our two UltraVISTA data sets were modeled by radially symmetric Sersic galaxy light profiles by plugging in the total flux $F_{total}(\lambda)$ at wavelength λ , the half-light radius θ_e , and galaxy morphology type from the catalogs.

For the UltraVISTA data sets, galaxy photometric types from the ‘‘Photometric Redshift Catalog Fall 2008’’ (Ilbert, et al., 2009) have been converted to common Sersic indices where ellipticals have been assigned Sersic index $n = 4$, and spiral and irregular galaxy shapes have been assigned an index of $n = 1$. We thereby obtain two independent data sets from our Ks catalog and R catalog of radially symmetric Sersic galaxy light profiles with reasonable physical parameters modeled after those found in the real universe.

4.2. A simple space telescope model

The observed intensity function, I , of a galaxy image obtained from a telescope is given by the convolution of the galaxy object light intensity function, O , and the PSF, P , of the telescope. This produces the well-known imaging equation,

$$I = O \star P \quad [98]$$

In our model calculation, we assume a diffraction-limited space telescope with a pure Airy disk PSF given by

$$P(\theta) = \frac{\pi D^2}{4\lambda^2} \left[\frac{2J_1(\pi D\theta/\lambda)}{(\pi D\theta/\lambda)} \right]^2 \quad [99]$$

where $P(\theta)$ is the intensity in the focal plane of the telescope as a function of angular coordinate θ , λ is the wavelength of light, D is the diameter of the telescope aperture, and $J_1(x)$ is the

Bessel function of the first kind of order one. Implicitly, we assume in equation [99] that the PSF is an image of a star of unit intensity, so that the integral of the PSF over θ is unity. The imaging equation then preserves the total flux of an astronomical object, only distributing it differently.

We also assume the PSF is uniform across the whole of the field of view.

We model the light intensity profile of the galaxy object using Sersic's equation in terms of the total flux as derived in the previous section in equation [97]. Normalized plots of Sersic intensity profiles for $n = \{4, 1, \frac{1}{2}\}$ and the Airy disk PSF and its Gaussian approximation are shown in Figure 9 and Figure 10. Note that the airy disk pattern drops to 50% power at a radius of $0.514 \lambda/D$, so its FWHM is $1.028 \lambda/D$.

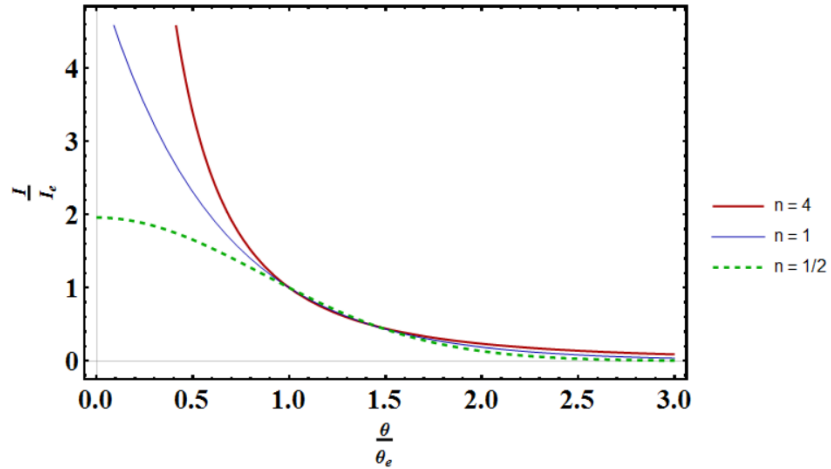


Figure 7 – Normalized Sersic galaxy light profile plots for Sersic indices $n = \{4, 1, \frac{1}{2}\}$, where θ_e is the effective half-light radius and I_e is the intensity at the effective radius θ_e .

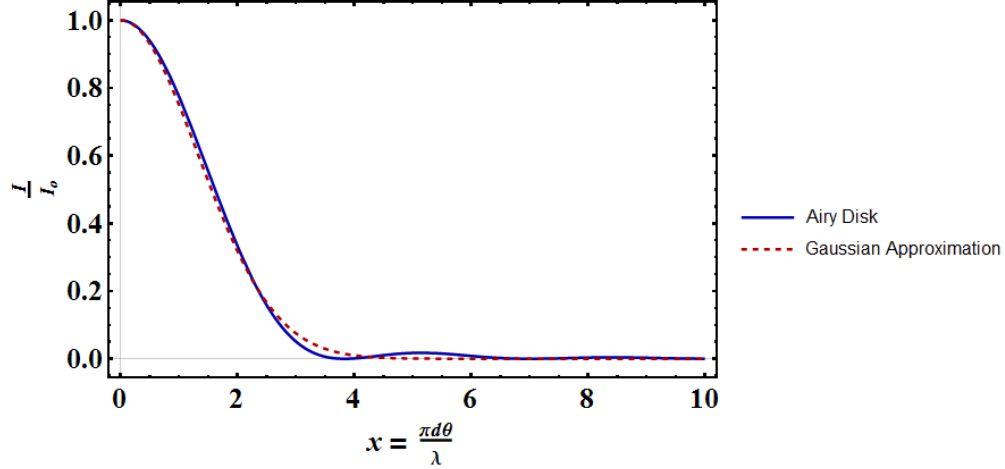


Figure 8 – Normalized airy disk PSF superimposed with its Gaussian approximation (dashed red line).

Unfortunately, the convolution integral of equations [97] and [99] in the imaging equation [98] is not analytically solvable in closed form. Moreover, real-life space telescopes don't measure continuous images, but rather the images are pixelized. Thus, in our calculations, we take the object function $O(\theta) = O(\theta_x, \theta_y)$ and the PSF $P(\theta) = P(\theta_x, \theta_y)$ and discretely sample the functions using Mathematica software over a 2D array of pixels. In this paper, the light profiles of each galaxy and the airy disk PSFs are sampled from $-7'' \leq \theta_{x,y} \leq +7''$ with a resolution of $0.02''$ per pixel. Additionally, Sersic profiles with Sersic index $n = 4$ have the center of the intensity profile falling off rather steeply, so to minimize the potential loss of information when discretely sampling over the rapidly varying central regions of the light profiles, the functions were all also super-sampled over a square grid of $\pm 0.1''$ around the center of the profile, $\vec{\theta} = (0,0)$, with a “super-resolution” of $0.001''$ per pixel. Once the functions were discretely sampled, a discrete convolution was performed by Mathematica software to produce a 2D array of pixel values representing 2D galaxy image-intensity profiles from a hypothetical diffraction-limited space telescope. Samples of these plots are shown in Figure 11 and Figure 12.

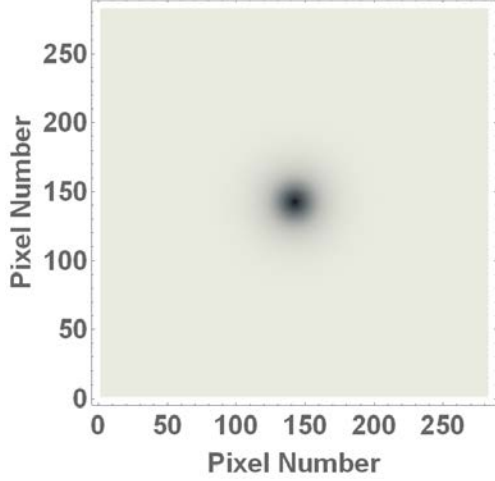


Figure 9 – Discrete Normalized Sersic Intensity Profile plotted in Mathematica (Sersic index $n = 1$ shown above). Black indicates high intensity; white indicates low intensity.

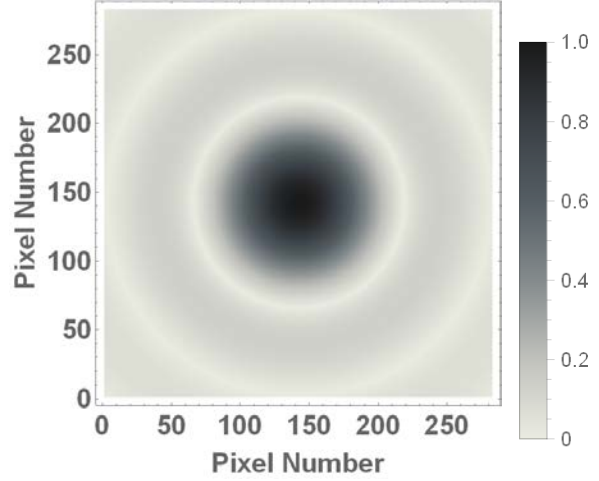


Figure 10 – Discrete normalized airy disk PSF plotted in Mathematica. Black indicates high intensity; white indicates low intensity. The grayscale intensities have been adjusted to enhance the brightness of the outer rings of the airy pattern in this plot.

4.3. Calculating Galaxy Flux S/N

Assuming sky-dominated noise for a source intensity profile $I_\nu(\Omega) = F_\nu \phi(\Omega)$, where F_ν is the total flux at frequency ν , and $\phi(\Omega)$ is the luminosity profile, observed against a background intensity B_ν over solid angle $d\Omega$ in a bandwidth $d\nu$ with central intensity ν by a telescope of area A , efficiency ϵ , and integration time t , the signal-to-noise ratio (S/N) is given by (Wright, 1985),

$$SNR = \left[\frac{d\nu A \epsilon t}{\nu h} \frac{F_\nu^2}{B_\nu \Omega_{eff}} \right]^{1/2} \quad [100]$$

where h is Planck's constant. The noise-effective solid angle Ω_{eff} in equation [100] is defined by (Wright, 1985):

$$\Omega_{eff} = \frac{[\int \phi(\Omega) d\Omega]^2}{\int \phi(\Omega)^2 d\Omega} \quad [101]$$

In the discrete case, integration becomes a summation over discrete pixels and we then define the effective number of noise pixels as

$$N_p = \frac{(\sum \phi)^2}{\sum(\phi^2)} \quad [102]$$

The noise-effective solid angle Ω_{eff} in equation [101] is then just the number of noise pixels N_p times the pixel-solid-angle $\Delta\Omega_{pixel}$ specifying the solid angle per pixel, $[\Delta\Omega_{pixel}] = \left[\frac{Solid\ Angle}{Pixel}\right]$:

$$\Omega_{eff} = N_p \cdot \Delta\Omega_{pixel} \quad [103]$$

The discrete sky noise-dominated S/N can then be written as

$$SNR = \left[\frac{dv}{v} \frac{A\epsilon t}{h} \frac{F_v^2}{B_v N_p \Delta\Omega_{pixel}} \right]^{1/2} = \sqrt{\frac{dv}{v} \frac{A\epsilon t}{h} \frac{F_v^2}{B_v \Delta\Omega_{pixel}} \left[\frac{(\sum \phi)^2}{\sum \phi^2} \right]^{-1}} \quad [104]$$

In our calculations of the S/N for our generic space telescope, we take the bandwidth over central frequency to be $\frac{dv}{v} = 1/5$, the quantum efficiency to be 50%, and the integration time to be 1000 seconds. We run calculations for telescope diameters of 1.2 m and 2.4 m inspired by the Euclid and WFIRST space telescopes. Sky background intensities are calculated from a fairly elaborate physical model of the zodiacal light at latitude 90° described in (Wright, 1998), which are summarized in Table 1. For confidence in this sky model, we note that the Hubble Space Telescope (HST) table of high sky background from the Wide Field Camera 3 Instrument Handbook for Cycle 24 (Dressel, 2016) is in good agreement with the zodiacal light from the model at latitude 0° . We also assume our telescopes to be cold enough so that their thermal emission is much less than the zodiacal background. This implies a telescope temperature $T < 132\text{ K}$ so that the blackbody radiation intensity is less than the sky background intensity at the L

band around 3.6 μm . In the Results section, we will plot the S/N vs. wavelength from equation [104] to determine the wavelength bands with the best signal.

Wavelength (microns)	Sky Background Intensity (kJy/Sr)
0.7	93
0.9	109
1.25	106
1.6	91
2.2	68
3.5	58

Table 1 – Table of sample sky background intensities at ecliptic latitude 90° calculated from the physical model described in (Wright, 1998) and used in this paper.

4.4. Introducing Shear and Calculating Ellipticity measurement variance

The images obtained directly from the image equation [98] with Sersic galaxy objects and airy disk PSFs are completely radially symmetric; i.e., the galaxy images are circular on a projected 2D plane. To simulate weak gravitational lensing on distant galaxies, we introduce a shear transformation on the object intensity $O(\theta)$ by a linear rescaling of the radial (angular) coordinate parameter $\theta = |\vec{\theta}|$ in the Sersic pattern,

$$\vec{\theta} = \begin{pmatrix} x \\ y \end{pmatrix} \rightarrow \vec{\theta}' = \mathcal{A} \cdot \vec{\theta} \quad [105]$$

where \mathcal{A} is the Jacobian matrix describing the distortion of images by weak gravitational lensing. If the size of the source is much smaller than the characteristic angular scale of the

deflector, we can locally linearize the gravitational lens mapping, which is then described by the Jacobian of the weak gravitational thin lens equation,

$$\mathcal{A} = (1 - \kappa) \begin{pmatrix} 1 - g_1 & -g_2 \\ -g_2 & 1 + g_1 \end{pmatrix} \quad [106]$$

where g_i , $i = 1,2$ are the components of the reduced shear, and κ is the convergence in gravitational lensing theory (Schneider, 1999).

	< 0	> 0
κ		
g_1		
g_2		

Figure 11 – Effects of the convergence κ and the components of shear g_1 and g_2 are shown. The green circle represents an unstretched circular image where all lensing parameters are presumed to be zero. The transformation on the initial circle depends on whether these parameters are positively or negatively valued.

As we are only interested in the effect of shear in the present analysis, we ignore the convergence, taking $(\kappa - 1) \rightarrow 1$ in the transformation equation. Additionally, the ability to measure the shear component g_1 is directly related to the ability to measure g_2 , so we need only

concern ourselves with one of the components of the reduced shear \vec{g} . For simplicity, we focus on g_1 and simply set $g_2 = 0$ and $g_1 = g$. The transformation on coordinates then simplifies to

$$\vec{\theta} = \begin{pmatrix} x \\ y \end{pmatrix} \rightarrow \vec{\theta}' = \begin{pmatrix} x' \\ y' \end{pmatrix} = \begin{pmatrix} 1-g & 0 \\ 0 & 1+g \end{pmatrix} \cdot \begin{pmatrix} x \\ y \end{pmatrix} = \begin{pmatrix} (1-g)x \\ (1+g)y \end{pmatrix} \quad [107]$$

When $g > 0$, a circle under this transformation is stretched in the x -direction and when $g < 0$, a circle is stretched in the y -direction. If $g = 0$, then the image is unstretched.

The stretch obtained by the introduction of weak lensing shear is applied only to the Sersic galaxy object intensity, $O(\theta) \rightarrow O'_{stretch}(\theta')$. Gravitational shear does not affect the PSF of the telescope. The stretched image intensity I' obtained from the imaging equation is now just

$$I' = O'_{stretch} \star P$$

To first order, we can Taylor expand the stretched image intensity I' as

$$I' = I + \Delta I = I + g \left. \left(\frac{\partial I'}{\partial g} \right) \right|_{g=0} \quad [108]$$

where I is the galaxy image obtained by convolution before introducing shear, and I' represents the stretched galaxy image. Note that $\left. \left(\frac{\partial I'}{\partial g} \right) \right|_{g=0}$ has a quadrupole shape like that seen in Figure

14. From this transformation equation [108], a least squares estimate of g gives

$$g = \frac{\int I' \left. \left(\frac{\partial I'}{\partial g} \right) \right|_{g=0} d\Omega}{\int \left. \left(\frac{\partial I'}{\partial g} \right) \right|_{g=0}^2 d\Omega} \quad [109]$$

where the variance of g is then

$$\sigma^2(g) = \frac{\sigma^2(I')}{\int \left. \left(\frac{\partial I'}{\partial g} \right) \right|_{g=0}^2 d\Omega} \quad [110]$$

Assuming sky-dominated noise uniformly distributed across the telescope with a background intensity B_ν over solid angle $d\Omega$, and where N_{sky} represents the electron count of sky noise in one pixel, the numerator of [110] is just

$$\sigma^2(I') = \sigma_{sky}^2(I') = N_{sky} = \left(\frac{A\epsilon t d\nu}{h\nu} \Delta\Omega_{pixel} \right) B_\nu \quad [111]$$

On the denominator of equation [110], we again convert the continuous calculus into discrete sums and differences to be calculated over pixels. Thus,

$$\int \left(\frac{\partial I'}{\partial g} \Big|_{g=0} \right)^2 d\Omega \rightarrow \sum \left(\frac{\Delta I'}{\Delta g} \Big|_{g=0} \right)^2 \Delta\Omega_{pixel} \quad [112]$$

Here in the discrete case, we take $\Delta I'$ to be the difference of an x -stretched intensity image subtracted from a y -stretched intensity image. Recall that the difference between a shear in the x -direction and y -direction is a matter of whether the reduced shear parameter g is positive or negative, respectively. Thus,

$$\Delta I' = I'_{x-stretch} - I'_{y-stretch} = I'(g) - I'(-g) \quad [113]$$

For our calculations, we let $|g| = 0.1$, which corresponds a 10% stretch. A plot of

$\Delta I' = I'_{x-stretch} - I'_{y-stretch}$ produces a “four-leaf clover” quadrupole-like image as shown in

Figure 14 plotted in Mathematica.

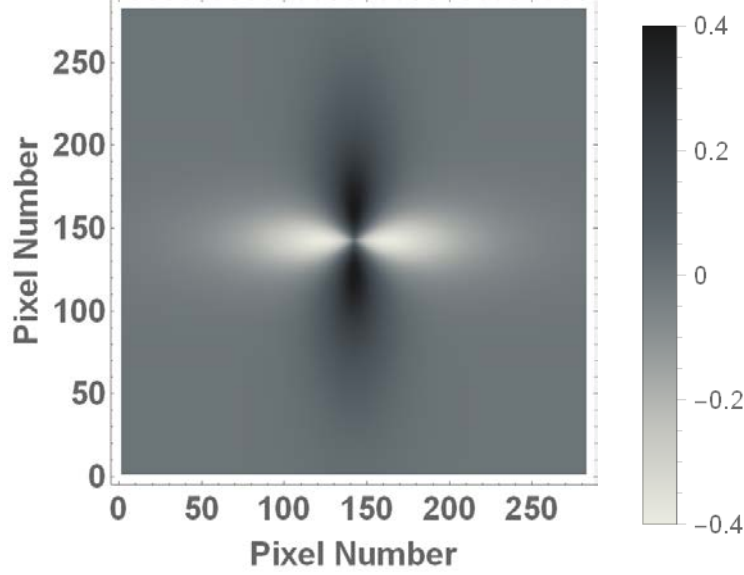


Figure 12 – Normalized density plot of $\frac{\Delta I'}{I_o} = \frac{I'_{x-stretch} - I'_{y-stretch}}{I_o}$, where $I_o = I(0,0)$ is the peak intensity of the original galaxy image, made in Mathematica. This image is obtained by taking the difference of a Sersic galaxy light intensity stretched in the x -direction and the galaxy light intensity stretched in the y -direction. Black represents high intensity; white represents low intensity.

To convert the units of $\Delta I'$ in equation [113] into electron counts, denoted by ΔN_{source} , the unit conversion is

$$\Delta N_{source} = \left(\frac{A\epsilon t d\nu}{h\nu} \Delta\Omega_{pixel} \right) \Delta I \quad [114]$$

Thus, the full equation for the variance of the shear calculated over pixels from equation [110] can be written as

$$\sigma^2(g) = \frac{N_{sky}}{\sum \left(\frac{\Delta N_{source}}{\Delta g} \right)^2} = \frac{B_\nu}{\frac{d\nu}{\nu} \frac{A\epsilon t}{h} \Delta\Omega_{pixel}} \left[\sum \left(\frac{\Delta I}{\Delta g} \right)^2 \right]^{-1} \quad [115]$$

Of course, weakly lensed galaxies observed in the real universe are not intrinsically circular, and the only thing that can actually be measured is the observed galaxy ellipticity, which includes the measured intrinsic ellipticity of the galaxy plus the measured gravitational shear. The uncertainty in the shear, σ_g , arises from a combination of unavoidable intrinsic shape noise, $\sigma_{int}^2 = \langle \epsilon_{int}^2 \rangle$, and the measurement error of galaxy shapes, $\sigma_{meas}^2(\epsilon)$:

$$\sigma_g^2 = \sigma_{int}^2 + \sigma_{meas}^2(\epsilon) \quad [116]$$

Here, included in the measurement noise $\sigma_{meas}^2(\epsilon)$ is the uncertainty contributions from the telescope measurement and shape measurement methods. Studies have shown the intrinsic shape noise is typically on the order of $\sigma_{int} \sim 0.26$, and varies little from $z = 0$ to $z = 3$ (Leauthaud, et al., 2007), so actually equation [115] is the ellipticity measurement variance, σ_m^2 , rather than the shear variance σ_g^2 .

4.5. Analytical Gaussian Calculations

The procedure summarized above for the calculation of the ellipticity measurement variance is manageable by a computer because we have discretized the continuous equations across a finite 2D array of discrete pixels. The continuous integral equation for the shear variance in Equation [110] is not analytically tractable, primarily due to the inability to solve the convolution integral of Sersic's equation with the Airy disk PSF. However, the integrals become manageable if we resort to a Gaussian approximation of the light intensity profile and PSF. The tradeoff, of course, is that in reality galaxies and PSFs are not purely Gaussian. Nevertheless, the analytical results obtained from a Gaussian approximation can be compared with the discrete calculations modeled in Mathematica for consistency checks, and some general behavior of how the shear varies with wavelength may still be desirable from the analytic Gaussian results.

The central lobe of the Airy disk PSF may be approximated with a Gaussian profile such that

$$P(\theta) \approx I_{op} e^{-\frac{\theta^2}{2\sigma_p^2}} \quad [117]$$

where $I_{op} = \left(\frac{\pi D^2}{4\lambda^2}\right)$ is the central intensity of the PSF, and we take $\sigma_p \approx 0.42 \left(\frac{\lambda}{D}\right)$ to preserve the peak amplitude of the Airy pattern. The Gaussian approximation of the Airy disk pattern is shown in Figure 10.

The Sersic profile equation becomes a Gaussian distribution when the Sersic index is set to $n = \frac{1}{2}$. A plot of the $n = \frac{1}{2}$ Sersic profile is shown in Figure 9. The Sersic object intensity in equation [97] then becomes

$$O(\vec{\theta}) = I_e e^{b_{1/2}} \exp \left[- \left(\frac{\theta}{\theta_e (b_{1/2})^{-1/2}} \right)^2 \right] \quad [118]$$

Let us rewrite this as

$$O(\vec{\theta}) = I_{oS} e^{-\frac{\theta^2}{2\sigma_S^2}} \quad [119]$$

where $I_{oS} = I_e e^{b_{1/2}}$ is the central intensity of the Sersic profile with $I_e = \frac{b_{1/2}}{\pi e^{b_{1/2} \theta_e^2}} F_{total}$, and

$$\sigma_S^2 = \frac{1}{2} \theta_e^2 (b_{1/2})^{-1}.$$

The convolution integral in the imaging equation can now be analytically computed in this Gaussian approximation as

$$I = O \star P = \frac{\sqrt{2\pi} I_{op} I_{oS}}{\frac{1}{\sigma_p^2} + \frac{1}{\sigma_S^2}} e^{-\frac{x^2+y^2}{2(\sigma_p^2+\sigma_S^2)}} \equiv I_{O(S \star P)} e^{-\frac{x^2+y^2}{2\sigma_{(S \star P)}^2}} \quad [120]$$

where we have defined $I_{o(S^*P)} = \frac{\sqrt{2\pi}I_{op}I_{oS}}{\frac{1}{\sigma_P^2} + \frac{1}{\sigma_S^2}}$ to be the central intensity of the convolved image

profile; and $\sigma_{(S^*P)}^2 = \sigma_P^2 + \sigma_S^2$ to represent the standard deviation of the image Gaussian

distribution after convolution; and $\theta = |\vec{\theta}| = \sqrt{x^2 + y^2}$. As one would expect, the image profile

produced by convolution of the two Gaussian distributions is also Gaussian. Because Gaussian

distributions are easily integrated, we can obtain analytic expressions for the galaxy flux S/N and

shear variance of a Gaussian image by calculating the integrals in equations [101] and [110].

Substitution of equation [120] into Ω_{eff} in equation [101] provides an analytical result for the effective Gaussian solid angle Ω_{eff} :

$$\Omega_{eff} = \frac{[\int \phi(\Omega) d\Omega]^2}{\int \phi(\Omega)^2 d\Omega} = 4\pi(\sigma_P^2 + \sigma_S^2) = 4\pi \left(\frac{\theta_e^2}{2b_{1/2}} + \frac{0.2025\lambda^2}{D^2} \right) \quad [121]$$

Recall, the Sersic constant b_n is given by equation [92] or reasonably well approximated by equation [93]. For a Gaussian Sersic index $n = \frac{1}{2}$, the value of this constant can be solved

exactly from [92] which gives, $b_{1/2} = \ln 2 = 0.693$. Equation [93] approximates the value to be

$b_{1/2} \approx 0.673$. Substituting [121] into equation [100] for the general flux SNR, the Gaussian flux

SNR becomes

$$SNR = \left\{ \frac{dv}{v} \frac{A\epsilon t}{h} \frac{F_v^2}{B_v} \left[4\pi \left(\frac{\theta_e^2}{2b_{1/2}} + \frac{0.2025\lambda^2}{D^2} \right) \right]^{-1} \right\}^{1/2} \quad [122]$$

To obtain a Gaussian approximation of the shear variance, we must first introduce the effects of weak gravitational shear to break radial symmetry by imposing the same linear

transformation as in equation [107]. The result of this transformation on the Gaussian Sersic

function is that

$$O(\vec{\theta}) \rightarrow O'(\vec{\theta}') = I_{o_s} e^{-\frac{(x')^2 + (y')^2}{2\sigma_s^2}} = I_{o_s} e^{-\frac{[(1-g)x]^2 + [(1+g)y]^2}{2\sigma_s^2}} \quad [123]$$

where we have again introduced the reduced shear g to simulate weak lensing distortions on the galaxy light profile shape. The convolution of this stretched Gaussian Sersic profile with the Gaussian approximation of the Airy disk PSF via the imaging equation then yields

$$I' = \frac{2\pi I_{o_p} I_{o_s}}{\sqrt{\frac{1}{\sigma_p^2} + \frac{(1+g)^2}{\sigma_s^2}} \sqrt{\frac{1}{\sigma_p^2} + \frac{(-1+g)^2}{\sigma_s^2}}} \exp\left[-\frac{(1-g)^2 x^2}{2[(-1+g)^2 \sigma_p^2 + \sigma_s^2]} - \frac{(1+g)^2 y^2}{2[(1+g)^2 \sigma_p^2 + \sigma_s^2]}\right] \quad [124]$$

Again, only the Sersic galaxy image is stretched while the PSF remains unaffected by the shear. The value of the shear parameter g and its variance $\sigma^2(g)$ are given by equations [109] and [110]. Assuming sky dominated noise uniformly distributed across the telescope with a background intensity B_v over solid angle $d\Omega$, the numerator in the variance equation [110] is just:

$$\sigma^2(I) = \sigma_{sky}^2(I) = \frac{A\epsilon t dv}{hv} B_v \quad [125]$$

The integral in the denominator of [110] can now be computed analytically in this Gaussian approximation as

$$\int \left(\frac{\partial I'}{\partial g} \Big|_{g=0} \right)^2 d\Omega = 4\pi^3 I_{o_p}^2 I_{o_s}^2 \frac{\sigma_p^4 \sigma_s^8}{(\sigma_p^2 + \sigma_s^2)^3} \quad [126]$$

Plugging in all the definitions for the Gaussian variables and rewriting [126] in terms of the galaxy and telescope parameters, we have

$$\int \left(\frac{\partial I'}{\partial g} \Big|_{g=0} \right)^2 d\Omega = \frac{0.01518 F_{tot}^2 \theta_e^4}{b_{1/2}^2 \left(\frac{\theta_e^2}{2b_{1/2}} + \frac{0.1764 \lambda^2}{D^2} \right)^3} \quad [127]$$

The full shear variance equation after proper unit conversion is then

$$\sigma^2(g) = B_v \left[\left(\frac{A\epsilon tdv}{h\nu} \right) \frac{0.0151 F_{tot}^2 \theta_e^4}{b_{1/2}^2 \left(\frac{\theta_e^2}{2b_{1/2}} + \frac{0.1764 \lambda^2}{D^2} \right)^3} \right]^{-1} \quad [128]$$

4.6. Calculating an Effective Galaxy Number for Weak Lensing Shape Measurement

The number of galaxies that have measurable shapes per solid angle in a given band depends on the number of counts of galaxies, $n(m)$, where m is the magnitude. Ultimately, we will sort our galaxy data in the Ks- and R- selected UltraVISTA catalogs into half-magnitude bins, using the Ks- and R-band total flux for the bin selections in each catalog, respectively. Counts are then weighted by how well we measure the galaxy shapes using the intrinsic ellipticity variance as a floor and counting only those galaxies that lie above an S/N threshold, which we choose to be $S/N > 10$, as is typical of weak lensing surveys (Kacprzak, et al., 2012). Because all galaxies are sorted by their Ks (or R) band flux, and assuming the total galaxy flux is proportional to the square of the effective half-light radius, we rescale the galaxy flux and half-radii data in each half-magnitude bin to extrapolate the catalog to fainter magnitudes via

$$\begin{cases} r_e \rightarrow r_e \left(\frac{F_{selection}}{F_m} \right)^{-1/2} \\ F_v \rightarrow F_v \left(\frac{F_m}{F_{selection}} \right) \end{cases} \quad [129]$$

where, F_v is the total galaxy flux in a given band, $F_{selection}$ is total flux in the Ks- or R-band for respective catalog, and F_m is the flux in the middle of a given half-magnitude bin selected in the Ks-band or R-band for the respective catalog.

Computing re-scaled values of the flux S/N and ellipticity measurement variance using the substitutions in Equation [129], we then calculate an effective number of galaxies per square degree in a given half-magnitude bin via

$$n_{eff}(m, \lambda, t) = \frac{N_{Source}}{N_{data}} \sum_i \left[\frac{\sigma_{int}^2}{(\sigma_{int}^2 + \sigma_{measured}^2)} \right] \quad [130]$$

The factor in front the summation takes the source galaxy counts per square degree, N_{Source} , over the number of sample galaxies, N_{data} , in a given half-magnitude bin selected from our catalog of galaxy data. The summation over i is taken over all sample galaxies in a given wavelength band above an S/N threshold of 10. We take $\sigma_{int} = 0.26$ (see Section 4.4 for justification). Because the flux S/N and shear variance depend on the telescope integration time, t , the effective number density also depends on t .

For N_{Source} , we fit the source galaxy counts per square degree from (Madau & Pozzetti, 2000) to the equation

$$\log \left[\frac{dN_{source}}{dm} \right] = F + 0.6 * [K_{AB} - 15] - By \quad [131]$$

with $y = w \left[\sqrt{(1 + x^2)} - 1 \right]$, $x = \max[0, [K_{AB} - A]/w]$ and $F = 0.77$, $K_{AB}(break) = A = 18.98$, $d(slope) = B = 0.34$, $width = w = 0.7$. The By term reduces the slope, and flattens the counts for really faint sources and avoids Olbers' paradox. With $dm = 0.5$ for half-magnitude bins, we have the number of source galaxies from the fit as

$$N_{Source} = 0.5 \times 10^{F+0.6[K_{AB}-15]-B \cdot y} \quad [132]$$

A plot of this fitting equation is displayed in Figure 15, along with the galaxy counts we get from our sample data for the Ks and R catalogs, respectively.

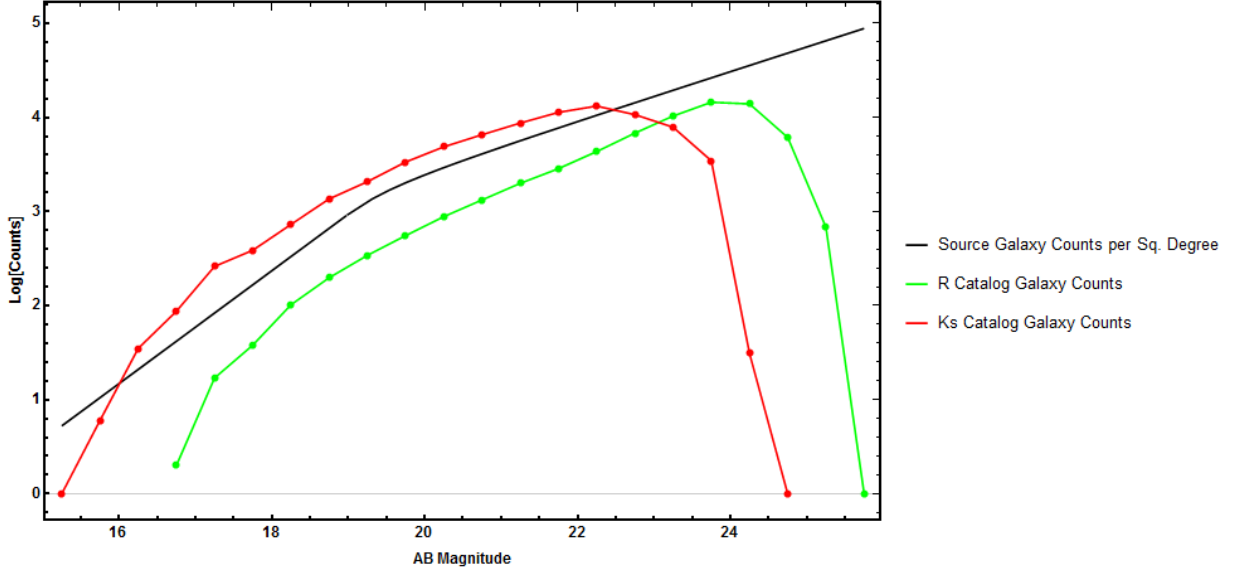


Figure 13 – Plot of galaxy source counts per square degree sampled in half-magnitude bins (black) superimposed with the galaxy counts in half-magnitude bins we get from our R catalog (green) and our Ks catalog (red). The black curve shows the model from equation [133] for the K-band counts. The R counts (green) are plotted as function of R-band AB magnitude and the K counts (red) are plotted as function of K-band AB magnitude.

Equation [130] gives the effective number of galaxies in a given half-magnitude bin. To find the total number of effective galaxies per square degree, we must sum equation [130] over all half-magnitude bins:

$$N_{eff}(\lambda, t) = \sum_m n_{eff} = \sum_m \left\{ \frac{N_{source}}{N_{data}} \sum_i \left[\frac{\sigma_{int}^2}{(\sigma_{int}^2 + \sigma_{measured}^2)} \right] \right\} \quad [133]$$

4.7. Ellipticity Measurement on the Frontier Parallel Fields

We perform a crude measurement of galaxy ellipticities in the six HST FPFs using Source Extractor (SExtractor) software (Bertin & Arnouts, 1996) in order to estimate a reduced shear

signal at the location of the parallel fields. The first order moment of an object is defined in SExtractor by

$$\bar{x} = \frac{\sum I_i x_i}{\sum I_i} \quad [134]$$

$$\bar{y} = \frac{\sum I_i y_i}{\sum I_i} \quad [135]$$

All of the x_i and I_i values in these formulae are the values from the pixels identified in the segmentation map as belonging to the object, and are thus influenced by detection thresholds and segmentation settings in SExtractor. The second order quadrupole moments are calculated by the software via

$$Q_{ij} = \frac{\sum_i \sum_j I_i (\theta_i - \bar{\theta}_j) (\theta_j - \bar{\theta}_i)}{\sum_i I_i} \quad [136]$$

This is essentially equation [66] computed over discrete pixels with a weight factor $q_I = I$, or rather, $q_I = IH(I - I_{th})$, where H is the Heaviside function with I_{th} being a threshold intensity that SExtractor uses for the detection and identification of an object since in principle a galaxy's light profile extends to infinity while SExtractor only computes the summations in [136] over the pixels for which an object has been detected. We use these SExtractor moments to calculate the observed complex ellipticities defined by equation [68] for galaxies in the HST PPFs.

Accounting for the HST PSF is nontrivial, and utilities such as TinyTim allow for a fairly accurate models of the HST PSF. In an effort to further simplify the procedure however, we will simply assume a purely symmetric Gaussian PSF in the form of equation [117]. While this choice is unrealistic and unrepresentative of the real HST PSF, it makes deconvolution of the PSF simple and allows for relatively easy extraction of an approximate galaxy source ellipticity signal.

The average source ellipticity among a significantly large density of distant galaxy images is directly related to reduced gravitational shear signal (see equation [80]). We assume equations [88] and [89] hold and use these to correct for the PSF, and note that by assuming a symmetric Gaussian, the PSF ellipticity χ_{PSF} in [90] simply vanishes. We calculate weighted average ellipticity using the same weight used for the effective galaxy number calculation in equation [130] of Chapter 4.6 scaled by the intrinsic galaxy shape, namely,

$$\langle \epsilon_i \rangle_{ave} = \frac{\sum_i w_i g_i}{\sum_i w_i}, \quad \text{with} \quad w_i = \frac{\sigma_{int}^2}{(\sigma_{int}^2 + \sigma_{measured}^2)} \quad [137]$$

where $i = 1, 2$ gives the two components of the complex shear, $\sigma_{int} = 0.26$ is the intrinsic galaxy shape noise and $\sigma_{measured}^2$ is the measured galaxy shape noise. We approximate $\sigma_{measured}^2$ using the Gaussian approximation given in equation [127] that we derived in Section 4.5. The magnitude of the average ellipticity is then gotten by

$$\langle |\epsilon| \rangle_{ave} = \sqrt{\langle \epsilon_1 \rangle_{ave}^2 + \langle \epsilon_2 \rangle_{ave}^2} \quad [138]$$

The average angle is gotten by

$$\langle \phi \rangle_{ave} = \frac{1}{2} \text{Arg}(\langle \epsilon_1 \rangle_{ave} + i \langle g_2 \rangle_{ave}) = \frac{1}{2} \text{Arg}(\langle \epsilon \rangle_{ave}) \quad [139]$$

The factor of $\frac{1}{2}$ is necessary since the complex shear is defined by $\epsilon = \epsilon_1 + i\epsilon_2 = |\epsilon|e^{2i\phi}$, with the factor of 2 in the complex exponential accounting for the transformation properties of an ellipse onto itself after a rotation of 180° . Thus, the argument of complex ϵ provides 2ϕ instead of ϕ .

In practice, the reduced shear is not exactly equal to the average ellipticity that can be measured by real telescopes. Even assuming an isotropic PSF, the limiting galaxy magnitude used for detection, the photometric depth of the image, and the size of the seeing disk all effect the measurement of the average ellipticity signal in a field, so the $\langle \epsilon \rangle_{meas}$ that we measure is not

exactly equal to the $\langle \epsilon \rangle$ defined in theory. Instead, the mean image ellipticity will be proportional to the reduced shear, $g \approx f \langle \epsilon \rangle_{meas}$, where f is a correction factor. This correction factor can be estimated by simulating realistic galaxy fields imposed with a known shear signal, applying the measurement scheme used on the real data to the simulated field, and then measuring the average ellipticity on the simulated field to compare to the known shear value. Instead of following this procedure, however, we will compare our measured average ellipticity to the reduced shear signal in the Abell 2744 cluster measured by (Medezinsk, et al., 2016). We will then take the ratio of the reported shear in the Abell 2744 FPF to our measured average ellipticity to be our correction factor f , and will apply this correction factor to recalibrate our shear values on all six of the FPFs. Once a calibrated average reduced shear signal has been estimated for a particular FPF, equation [85] will be used to calculate the encircled mass, which assumes a symmetric matter distribution and is the estimate of the total projected mass inside a radius equal to the distance from any given FPF to the corresponding primary FF.

We conclude this chapter by noting that a purely isotropic PSF will have the effect of rounding out small galaxy shapes. Assuming a purely symmetric Gaussian PSF as we do here is likely to underestimate the “true” reduced shear signal. On the other hand, by assuming there is no anisotropic part of the telescope PSF when there actual is, there is a potential to overestimate of the true shear signal since an anisotropic part of the real PSF has the effect of adding a spurious measured ellipticity to small objects that we are not bothering to subtract.

Additionally, in using SExtractor’s pre-equipped quadrupole moment calculations, it is likely we are oversampling the noise in the quadrupole calculations in the extreme pixels at the edge of a detected galaxy and thus, will have larger shape measurement noise versus what one would have utilizing a more robust weighting scheme such as $q_I[I(\theta)] = I(\theta)W(\theta)$ as mentioned in

Section 3.6. For example, a Gaussian weight factor W as originally proposed by (Kaiser, et al., 1995) can be tuned to cut off at large angular separations from the galaxy center faster than $q_I = I(\theta)$, thereby reducing the noise counted at the galaxy edge in the quadrupole moment formulae. Furthermore, if a galaxy features a bright compact core emitting a significant fraction of the galaxy's total light, then this core can become smeared out by the PSF. The observed ellipticity in this case may be dominated by the core and contain little information about the actual galaxy ellipticity. For this reason, (Bonnet & Millier, 1995) defined a quadrupole moment with a weight factor $W(\theta)$ which not only cuts off at large angular separations, but which is also small near the galaxy center. Figure 16 compares a few of the different weighting schemes used by other groups.

Normalized Sersic Profile ($n = \frac{1}{2}$) with Various Weights Applied

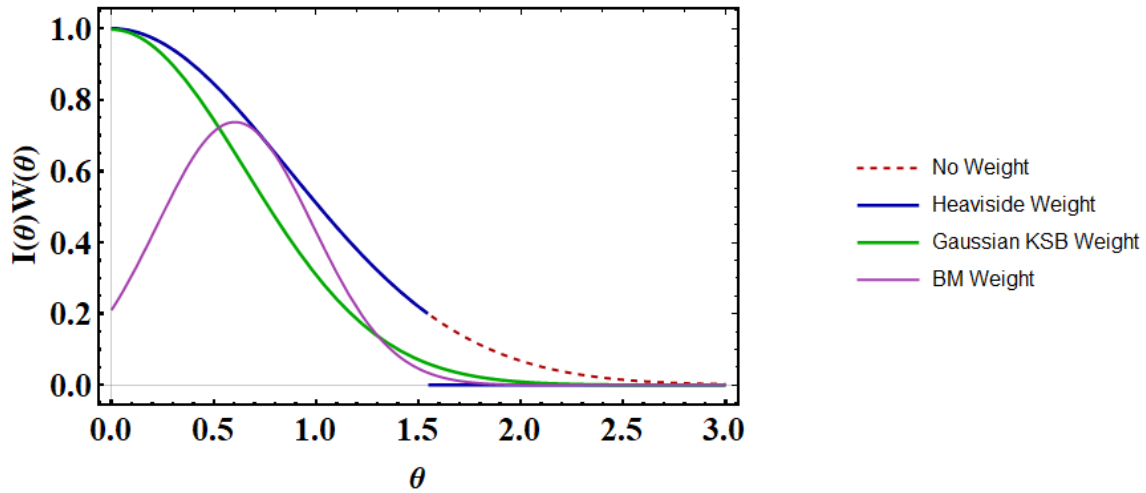


Figure 14 – A comparison of a few different weight functions $W(\theta)$ used by a few different groups. The dashed red line represents no weight, or $W(\theta) = 1$, and is the baseline plot of a Gaussian galaxy light profile. The blue line is similar to SExtractor’s measurement of the galaxy shape which matches the measured the intensity profile but cuts off at some threshold intensity used by the program to represent the boundary of a galaxy object. The green line is similar to the original KSB Gaussian weight which falls off faster than the original profile to avoid counting too much noise at the galaxy edge. Finally, the purple line represents the weight used by (Bonnet & Millier, 1995) which is small at the center of the galaxy and falls off quickly at the galaxy edge.

5. Data

In this chapter we describe the ULTRAVISTA field and Frontier Fields data used to construct the collections of Sersic galaxy light profiles used in our model calculations. For the ULTRAVISTA field data, catalogs of galaxy morphology were readily available for public use, and the galaxy parameters required for Sersic’s equation were simply extracted from these

catalogs. For the FFs, we used SExtractor software on the publically available FF mosaics to estimate the required Sersic parameters for ourselves.

5.1. Constructing a galaxy catalog from the UltraVISTA field

Two independent sets of galaxy data were collected from the ultra-deep UltraVISTA Ks-selected and R-selected photometric catalogs (Muzzin, et al., 2013). These two catalogs are considered simultaneously in this paper to help track any possible role of wavelength-dependent incompleteness in our analysis. These catalogs each provide us with galaxy flux data from 11 different filters, including YJHKs-bands from UltraVISTA, u-band from CFHT, and BVgriz+ bands from Subaru. Stars and other objects with possibly nonsensical photometry and population parameters have been filtered out of the two catalogs, and a 5σ detection limit was imposed on the selection band total flux. Aperture magnitudes were given for all bands in the original UltraVISTA catalogs, while total flux was only provided for the Ks- or R-band, respectively. The ratio of the selection band total flux to selection band aperture flux was used as a conversion factor in each catalog to calculate total flux in other bands, assuming galaxy morphology can be treated as independent of wavelength.

Multi-object searches using the Infrared Science Archive (IRSA); Cosmic Evolution Survey (ULTRAVISTA), ULTRAVISTA Photometry Catalogs (Scoville, et al., 2007) were performed using a 0.5 arcsecond cone search radii with the “ULTRAVISTA ACS I+ band photometry catalog September 2007” (Leauthaud, et al., 2007) and “Photometric Redshift Catalog Fall 2008” (Ilbert, et al., 2009) to obtain half-light radii and morphological data in each of our catalogs, respectively. Throughout this paper, we will refer to these two sets of galaxy data collected from the UltraVISTA Ks-selected and R-selected photometric catalogs as either the Ks catalog or the R catalog. After filtering the original data in the full UltraVISTA catalogs

and after the ULTRAVISTA multi-object searches prescribed above, our Ks and R catalogs contain total galaxy source counts of 74,950 and 64,969, respectively. Although the original R-selected UltraVISTA catalog contains more galaxies than the original Ks-selected catalog, after the 5σ detection limit we impose, more of the dim sources in the R-catalog are cut whereas more of the brighter sources in the K-catalog survive, leaving us a filtered Ks catalog that is slightly larger than the filtered R catalog.

An approximate correction for the Hubble Space telescope point spread function was applied to the half-light radii in the catalogs via

$$(r_{true})^2 = (r_{measured})^2 - (r_{PSF})^2 \quad [140]$$

The mean and median half-light radius in the Ks catalog was 0.367 and 0.324 arcseconds, respectively, and for the R catalog the mean and median half-light radius were 0.363 and 0.317 arcseconds. The average sizes from the two UltraVISTA catalogs are very consistent. We assume the half-light radii of galaxies to be independent of wavelength and these radii values have been obtained by cross-referencing with the ULTRAVISTA ACS I+ band Photometry Catalog as mentioned above. The average total galaxy flux in each wavelength band in our two catalogs are summarized in Table 2 and Figure 17.

Filter	Ks catalog Mean (AB mag)	Ks catalog Median (AB mag)	R catalog Mean (AB mag)	R catalog Median (AB mag)
CFHT u*	24.928	24.857	24.369	24.408
Subaru B	24.476	24.603	24.082	24.225
Subaru g+	24.431	24.476	23.942	24.119
Subaru V	24.051	24.186	23.636	23.742
Subaru r+	23.645	23.835	23.321	23.602
Subaru i+	23.049	23.240	22.870	23.121
Subaru z+	22.677	22.855	22.632	22.862
VISTA Y	22.449	22.677	22.493	22.721
VISTA J	22.161	22.355	23.310	22.559
VISTA H	21.900	22.100	22.134	22.406
VISTA Ks	21.695	21.901	22.044	22.337

Table 2 – The mean and median total flux values for each of the wavelength bands in our Ks-selected and R-selected catalog collected from the UltraVISTA catalogs (*Muzzin, et al., 2013*).

Flux values are listed in AB magnitude.

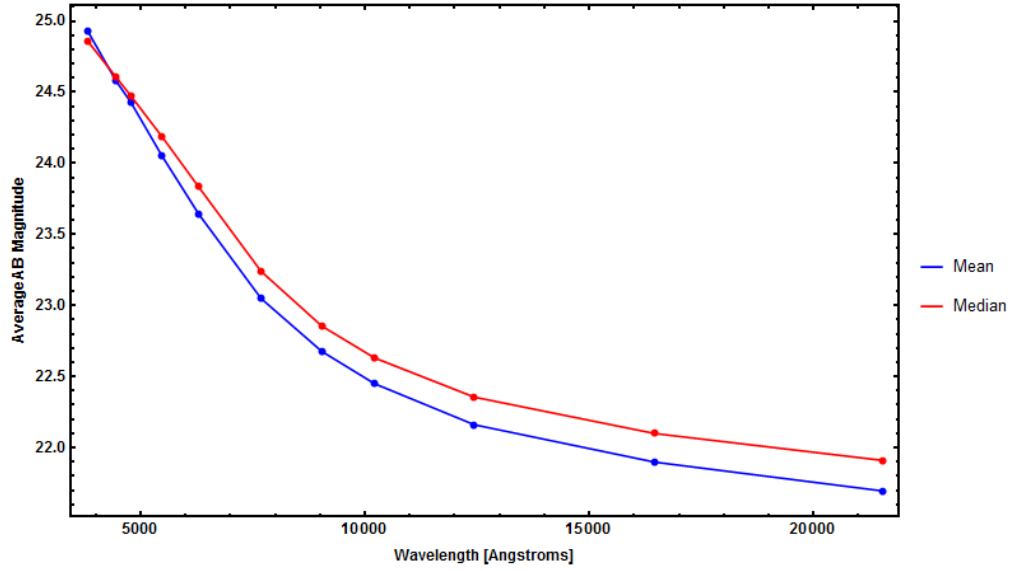


Figure 15 — Plot of mean and median AB magnitude of the 74,950 galaxies collected in the Ks catalog. The average brightness of galaxies is maximum in the Ks-band.

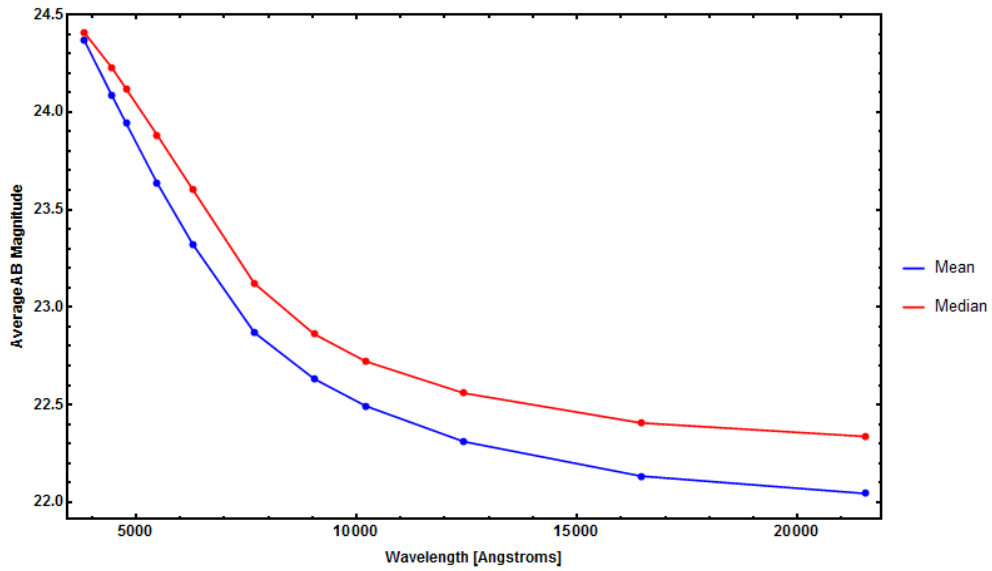


Figure 16 — Plot of mean and median AB magnitude of the 64,969 galaxies collected in the R catalog. The average brightness of galaxies is maximum in the Ks-band.

5.2. Constructing a galaxy catalog from the HST Frontier Parallel Fields

The HST FF Survey consists of six large galaxy clusters selected for their strong lensing properties: Abell 2744, MACSJ0416.1-2403, MACS0717.5+3745, MACS1149.5+2223, Abell S1063, and Abell370. These six clusters were chosen to allow simultaneous observation of the cluster field and a blank parallel field with the HST WFC3/IR and ACS cameras. The FPF observations are centered approximately six arcminutes from the main cluster core, and the weak lensing signal for the FPFs have median magnification factors between 1.02 and 1.30 for background galaxies between $1 < z < 9$ (Lotz, et al., 2017). Each field has been imaged across seven HST filter wavelengths: B_{F435W} (433nm), V_{F606W} (592nm), I_{F814W} (896nm) with the ACS/WFC, and Y_{F105W} (1055nm), J_{F125W} (1249nm), JH_{F140W} (1392nm), H_{F160W} (1537nm) with the WFC3/IR camera. Each camera was given 70 HST orbits for a total of 140 HST orbits over the whole survey.

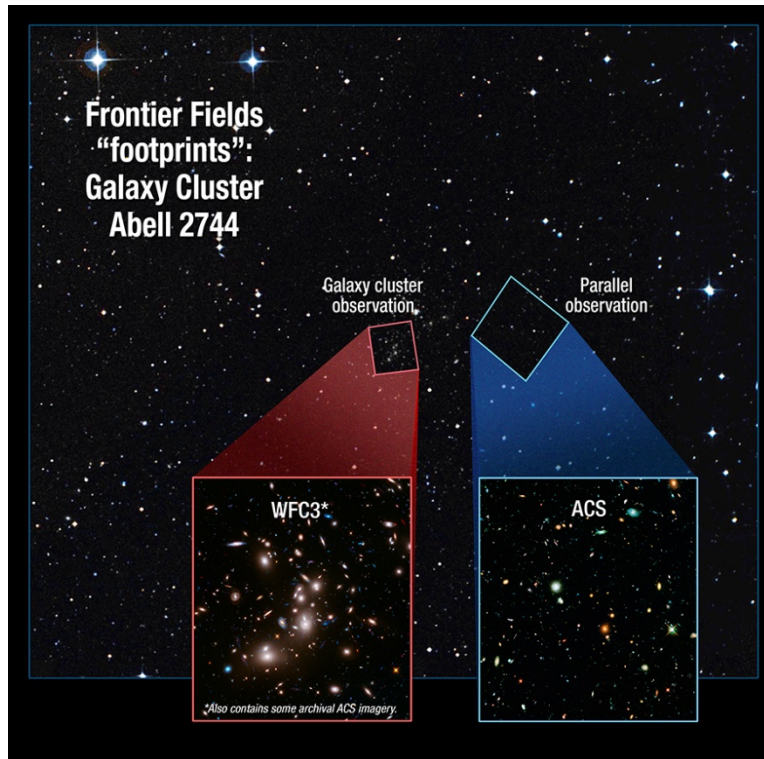


Figure 17 – This image illustrates the “footprints” of the Wide Field Camera 3 (WFC3) infrared detector, in red, and the visible-light Advanced Camera for Surveys (ACS), in blue. An instrument’s footprint is the area on the sky it can observe in one pointing. These adjacent observations are taken in tandem. In six months, the cameras swap places, with each observing the other’s previous location.

From: <https://frontierfields.org/2014/01/10/cluster-and-parallel-fields-two-for-the-price-of-one-2/>

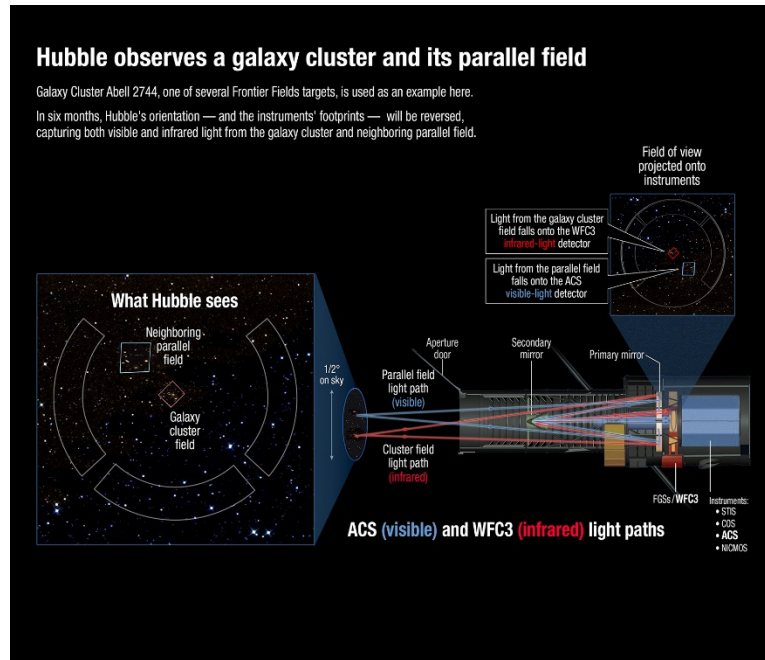


Figure 18 – This diagram shows the light paths that originate with the galaxy cluster field and the neighboring parallel field. The light from the galaxy cluster field (red) is imaged with the Hubble’s Wide Field Camera 3 (WFC3) infrared detector, while the light from the parallel field (blue) is imaged with the visible-light Advanced Camera for Surveys (ACS). Hubble’s entire field of view is shown on the left side of the diagram. It includes the “footprints” of ACS (red) and WFC3 (blue), as well as those of the fine guidance sensors (FGSs), which are the three, white wedges on the outside, and everything in between them.

From: <https://frontierfields.org/2014/01/10/cluster-and-parallel-fields-two-for-the-price-of-one-2/>

HST FPF 30 mas/pixel drizzled mosaics and weight images for each field and each color filter (Koekemoar, et al., 2014) were gathered from the Mikulski Archive for Space Telescopes (MAST) at STSCI. SExtractor was used to produce catalogs for each field image extracting

galaxy total flux, half-light radii and an estimation of the Sersic index. The six catalogs, one for each FPF, were ultimately combined into a single collection containing 6946 sources.

The detection strategy we adopt to construct our catalog is similar to the SExtractor configuration described in (Leauthaud, et al., 2007) to detect faint sources in the HST ULTRAVISTA field. A list of SExtractor parameters used are provided in Table 3 and summarized below. Our data is filtered with a 5 pixel (0.15”) FWHM Gaussian filtering kernel prior to detection. Weight maps produced by MultiDrizzle (Koekemoar, et al., 2014) are used with SExtractor WEIGHT_IMAGE option set to WEIGHT_MAP. Effective half-light radii are obtained with the FLUX_RADIUS parameter and PHOT_FLUXRAC set to 0.5, and this is used in conjunction with KRON_RADIUS to obtain a rough estimate of the Sersic index of each galaxy by taking the ratio between the two radii estimates and cross referencing with Table 1 in (Graham & Driver, 2005), which tabulates Kron radii in units of effective half-light radii via the relation

$$R_{Kron}(x, n) = \frac{R_e \gamma(3n, x)}{b^n \gamma(2n, x)} \quad [141]$$

Here, $x = b_n \left(\frac{R}{R_e}\right)^{1/2}$, the constant b_n is defined in terms of the Sersic index n which describes the “shape” of the light profile, and γ is the incomplete gamma function. If the ratio of the radii was less than or greater than 1.74, it was assigned a Sersic index of one or four, respectively.

PARAMETER	VALUE
DETECT_MINAREA	28
DETECT_THRESH	1.0
DEBLEND_NTHRESH	64
DEBLEND_MINCONT	0.065
CLEAN_PARAM	1.0
BACK_SIZE	100
BACK_FILTERSIZE	3
BACKPHOTO_TYPE	Local
BACKPHOTO_THICK	200

Table 3—SExtractor Configuration Parameters

H-band data was used for the initial detection of objects and cross-referenced with photometry in the other HST filters. Objects with $S/N < 5$ were omitted in the construction of our catalog, and only galaxies for which SExtractor returned good data in all colors were kept. We also omitted any flux data with AB magnitude greater than 28. The detected sources in our catalogs were then used to construct Sersic galaxy light profiles (Sersic, 1963) using the total galaxy flux, effective half-light radius, and Sersic index estimated with SExtractor according to equation [97].

	F160W	F140	F125	F105	F814	F606	F435
	(AB Mag)	(AB Mag)	(AB Mag)	(AB Mag)	(AB Mag)	(AB Mag)	(AB Mag)
Median	26.33	26.36	26.44	26.57	26.80	27.13	27.57
Mean	25.81	25.87	25.96	26.11	26.39	26.81	27.32

Table 4 — Average statistics of our total catalog containing 6946 galaxy sources constructed from combining the six individual FPF catalogs.

5.3. Using SExtractor to measure galaxy ellipticity in the Frontier Parallel Fields

To obtain an estimate of the reduced shear signal in each HST FPF, we need to measure the ellipticity of galaxy sources in each of the parallel fields. To do achieve this, we use the actual galaxy images this time instead of constructing a catalog of Sersic model galaxies as in previous sections. The same SExtractor detection strategy outlined in the previous section is used to locate and identify galaxy sources in the HST FPFs. We chose to keep only sources with $S/N > 10$ and AB magnitude greater than 28 for shape measurements. As outlined in Section 4.7, we utilize SExtractor’s ability to automatically calculate and output galaxy quadrupole moments according to equation [136] and compute complex ellipticity components defined by equation [68] for each galaxy source. For each of the parallel fields, the HST F160w H-band mosaics are used for galaxy shape measurements since the longer wavelengths are expected to have greater flux S/N and smaller ellipticity measurement variance for better weak lensing shear measurement (see the Results chapters for verification).

	Abell 2744	Abell 1063	Abell 370	MACS1149	MACS0717	MACS0416
N_{eff}	1,286	2,424	1,307	1,909	1,493	1,010

Table 5 – Effective number of galaxy sources in each HST FPF using the detection and filtering procedures outlined in Section 5.3.

6. Results

Here we present the results of our model calculations for the galaxy flux S/N, shape measurement error, and effective galaxy number density vs. wavelength. Sub chapters provide results for the ULTRAVISTA field and FPFs, respectively. We note that the ULTRAVISTA field sub chapters include a couple of additional sections for making the model galaxy source shapes intrinsically elliptical instead of circular and for plotting surface brightness vs. galaxy size. While useful, the results of these sections are nothing unexpected and thus excluded in the sub chapters for the FPF results.

6.1. UltraVISTA field

6.1.1. Galaxy Flux S/N vs. Wavelength

The galaxy flux S/N was computed for two subsets of 1000 randomly selected galaxies in the Ks- and R-selected UltraVISTA data sets, respectively, via equation [104]. We will henceforth refer to these two smaller collections of galaxy data the Ks subset and R subset. Using the future space telescope missions Euclid and WFIRST as a reference, we performed calculations for telescope diameters of 1.2 meters and 2.4 meters. Two hundred of these galaxies are individually plotted with flux S/N vs. wavelength for the Ks catalog in Figure 21 and Figure 45, and likewise, plots for the R catalog are displayed in Figure 23 and Figure 24. In these plots,

the median galaxy flux S/N is also plotted, calculated across the full 1000 galaxy subsets used in this calculation.

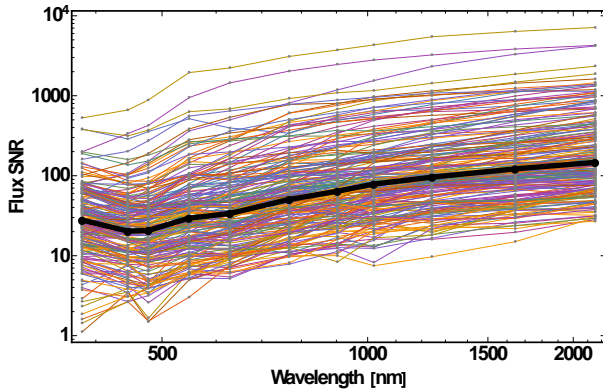


Figure 19 – Log-Log plot of galaxy flux S/N vs. wavelength using a 1.2 meter diameter telescope for the Ks catalog. Individual data points are plotted for 200 of these galaxies. The bold black dots and line represent the median S/N values at each wavelength band, which is calculated across the full 1000 galaxy subset used in the calculation. Median S/N values are shown in this plot to have their highest average value around the Ks-band.

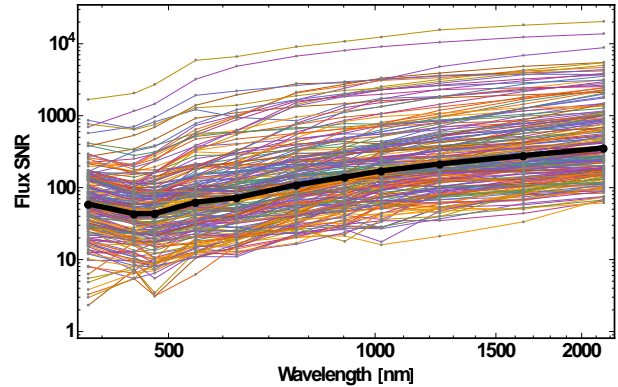


Figure 20 – Log-Log plot of galaxy flux S/N vs. wavelength using a 2.4 meter diameter telescope for the Ks catalog. Individual data points are plotted for 200 of these galaxies. The bold black dots and line represent the median S/N values at each wavelength band, which is calculated across the full 1000 galaxy subset used in the calculation. Median S/N values are shown in this plot to have their highest average value around the Ks-band.

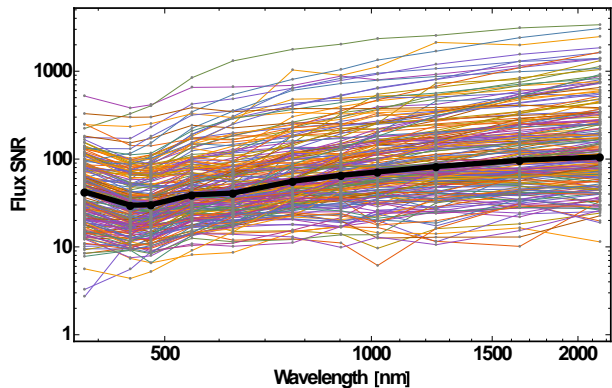


Figure 21 – Log-Log plot of galaxy flux S/N vs. wavelength using a 1.2 meter diameter telescope for the R catalog. Individual data points are plotted for 200 of these galaxies. The bold black dots and line represent the median S/N values at each wavelength band, which is calculated across the full 1000 galaxy subset used in the calculation. Median S/N values are shown in this plot to have their highest average value around the Ks-band.

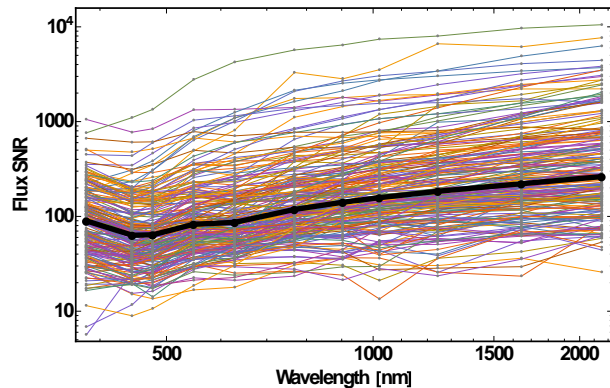


Figure 22 – Log-Log plot of galaxy flux S/N vs. wavelength using a 2.4 meter diameter telescope for the R catalog. Individual data points are plotted for 200 of these galaxies. The bold black dots and line represent the median S/N values at each wavelength band, which is calculated across the full 1000 galaxy subset used in the calculation. Median S/N values are shown in this plot to have their highest average value around the Ks-band.

In all cases considered, we find the maximum of the median flux S/N lies near the Ks-band. In both catalogs, the two times larger 2.4 meter diameter telescope results in S/N values which are on average about 2.2 times larger than S/N values obtained from a 1.2 meter diameter telescope. We note that by doubling the telescope diameter, a perfectly resolved galaxy theoretically results in two times larger S/N values, and point sources would produce four times larger S/N values.

Histogram plots of the number of galaxies across each wavelength band whose S/N is maximum for the Ks subset are shown in Figure 25 and Figure 26 for 1.2 meter and 2.4 meter

telescopes, respectively. Similar histogram plots for the R subset are shown in Figure 27 and Figure 28. These histogram plots all show a large majority of galaxies have their maximum S/N values lying around the Ks-band and the peak around the Ks-band in these plots correlate to the peaks shown in Figure 21 through Figure 24. This trend of maximum S/N peaking around Ks-band is demonstrated for both 1.2 meter and 2.4 meter diameter telescopes, and the peak around the Ks-band in the average S/N curves across wavelength is even more pronounced with the larger telescope.

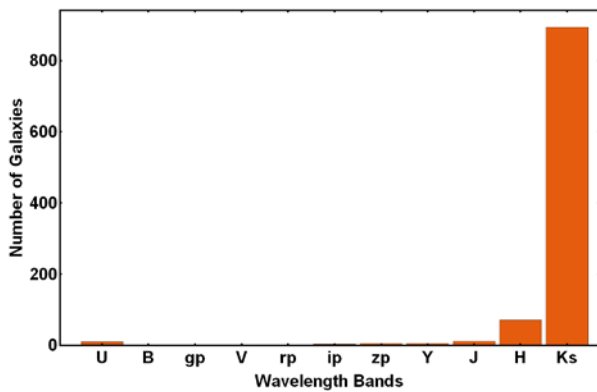


Figure 23 – Histogram plots of the band with the maximum S/N for the Ks selected galaxies using a 1.2 meter diameter telescope. There is a strong peak around the Ks-band showing a large majority of galaxies have their peak S/N value near these wavelengths.

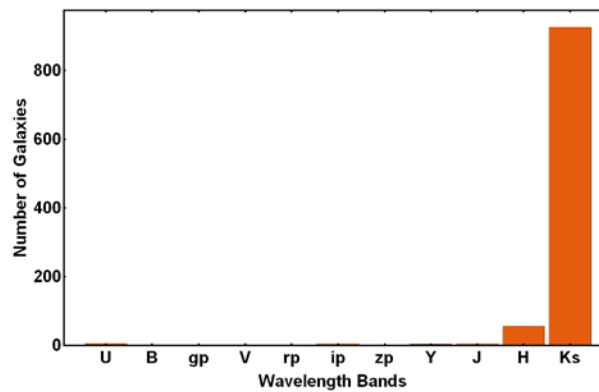


Figure 24 – Histogram plots of the band with the maximum S/N for the Ks selected galaxies using a 2.4 meter diameter telescope. There is a strong peak around the Ks-band showing a large majority of galaxies have their peak S/N value near these wavelengths.

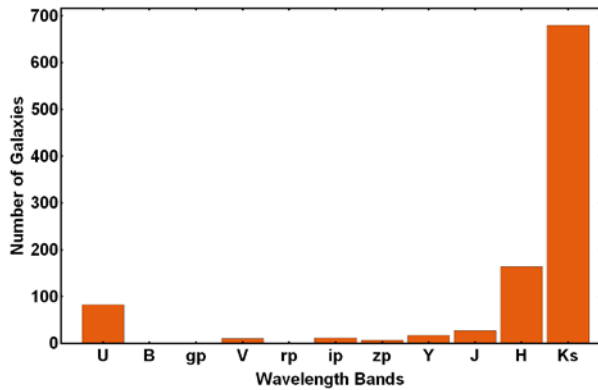


Figure 25 – Histogram plots of the band with the maximum S/N for the R selected galaxies using a 1.2 meter diameter telescope. There is a strong peak around the Ks-band showing a large majority of galaxies have their peak S/N value near these wavelengths.

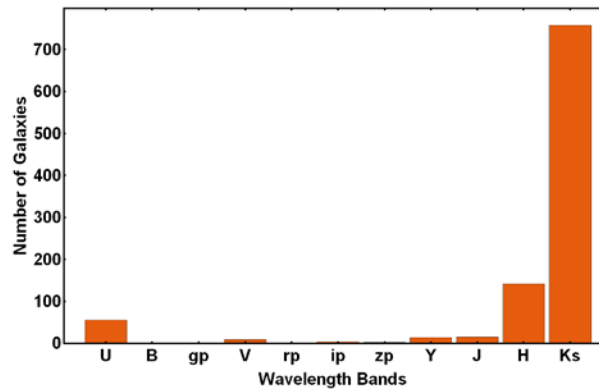


Figure 26 – Histogram plots of the band with the maximum S/N for the R selected galaxies using a 2.4 meter diameter telescope. There is a strong peak around the Ks-band showing a large majority of galaxies have their peak S/N value near these wavelengths.

6.1.2. Ellipticity measurement variance vs. Wavelength

The ellipticity measurement variance via equation [115] was computed for the same 1000 galaxy Ks and R subsets used Section 6.1.1 for telescope diameters of 1.2 meters and 2.4 meters. Plots of the calculated ellipticity measurement variance vs. wavelength for the Ks catalog set are shown in Figure 29 and Figure 30, and plots for the R catalog are shown in Figure 31 and Figure 32.

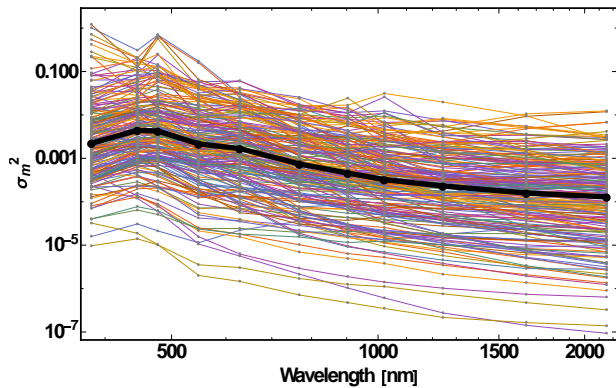


Figure 27 – Log-Log plot of the ellipticity measurement variance vs. wavelength for a 1.2 meter diameter telescope for the Ks subset.

Individual data points are plotted for 200 of these galaxies. The bold black dots and line represent the median ellipticity measurement variance values at each wavelength band, which is calculated across the full 1000 galaxy subset used in the calculation. Median measurement error values are shown in this plot to have their highest average value around the

Ks-band.

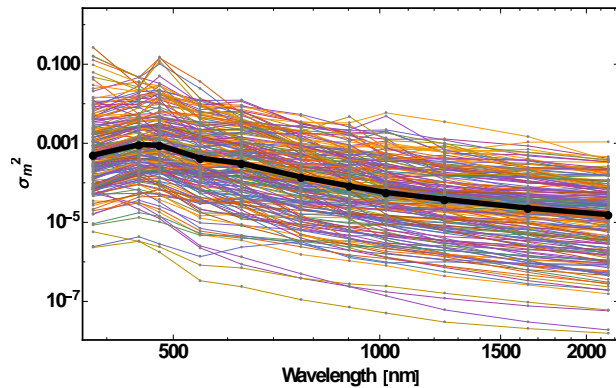


Figure 28 – Log-Log plot of the ellipticity measurement variance vs. wavelength for a 2.4 meter diameter telescope for the Ks subset.

Individual data points are plotted for 200 of these galaxies. The bold black dots and line represent the median ellipticity measurement variance values at each wavelength band, which is calculated across the full 1000 galaxy subset used in the calculation. Median measurement error values are shown in this plot to have their highest average value around the

Ks-band.

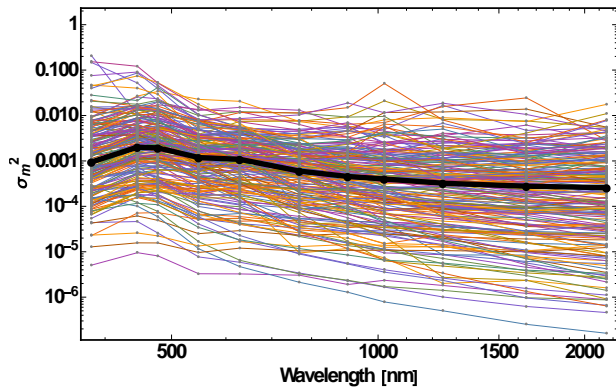


Figure 29 – Log-Log plot of the ellipticity measurement variance vs. wavelength for a 1.2 meter diameter telescope for the R subset.

Individual data points are plotted for 200 of these galaxies. The bold black dots and line represent the median ellipticity measurement variance values at each wavelength band, which is calculated across the full 1000 galaxy subset used in the calculation. Median measurement error values are shown in this plot to have their highest average value around the R band.

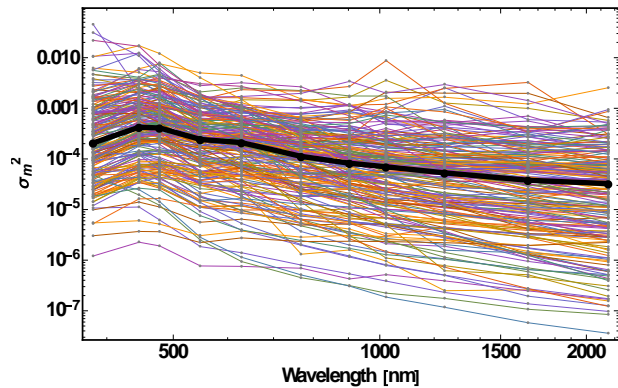


Figure 30 – Log-Log plot of the ellipticity measurement variance vs. wavelength for a 2.4 meter diameter telescope for the R subset.

Individual data points are plotted for 200 of these galaxies. The bold black dots and line represent the median ellipticity measurement variance values at each wavelength band, which is calculated across the full 1000 galaxy subset used in the calculation. Median measurement error values are shown in this plot to have their highest average value around the R band.

Both data sets show the median ellipticity measurement variance obtains a minimum value around the Ks-band. For the Ks (or R) subset, the larger 2.4 meter telescope diameter produces ellipticity measurement variance values generally smaller than the 1.2 meter diameter results by an average factor of 0.182 (0.126). In terms of S/N, this corresponds to a $\frac{1}{\sqrt{0.182}} \approx 2.34$ (2.817) times improvement with a 2.4 meter telescope over a 1.2 meter telescope.

Histogram plots shown in Figure 33 and Figure 34 display the number of galaxies in each wavelength band from the 1000 galaxies plotted in the Ks subset whose ellipticity measurement variance is minimum. The corresponding plots from the R subset are displayed in Figure 35 and Figure 36. These plots again exhibit a clear preference for each galaxy to have minimum variance around the Ks-band for both the 1.2 meter and 2.4 meter diameter telescopes. The trend favoring the Ks-band is even more dramatic using the larger 2.4 meter diameter telescope.

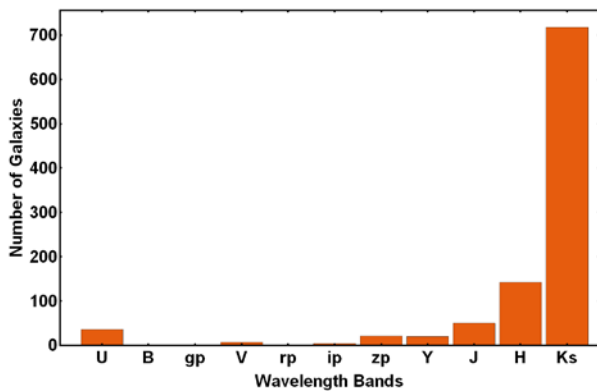


Figure 31 – Histogram plot of the number of galaxies in each wavelength band for the Ks subset whose ellipticity measurement variance is minimum using a 1.2 meter diameter telescope. There is a strong peak around the Ks-band showing a large majority of galaxies have their minimum value near these wavelengths.

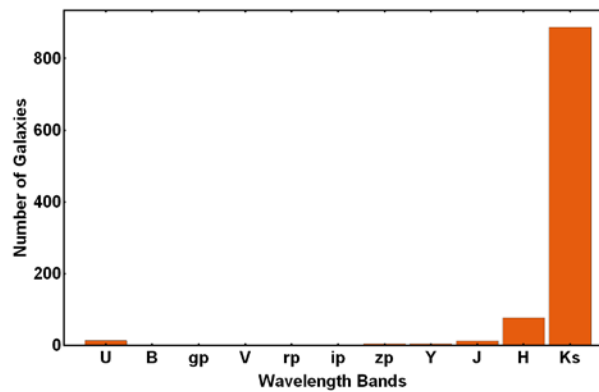


Figure 32 – Histogram plot of the number of galaxies in each wavelength band for the Ks subset whose ellipticity measurement variance is minimum using a 2.4 meter diameter telescope. There is a strong peak around the Ks-band showing a large majority of galaxies have their minimum value near these wavelengths.

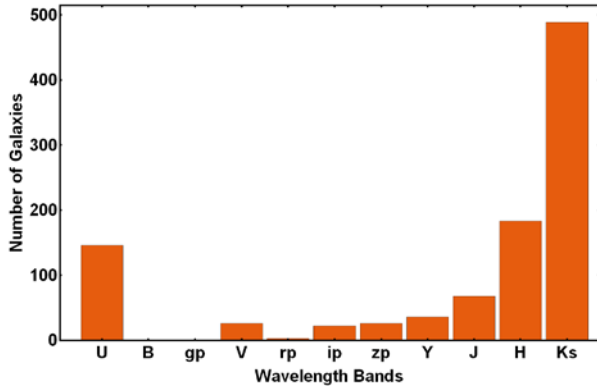


Figure 33 – Histogram plot of the number of galaxies in each wavelength band for the R subset whose ellipticity measurement variance is minimum using a 1.2 meter diameter telescope. There is a strong peak around the Ks-band showing a large majority of galaxies have their minimum value near these wavelengths.

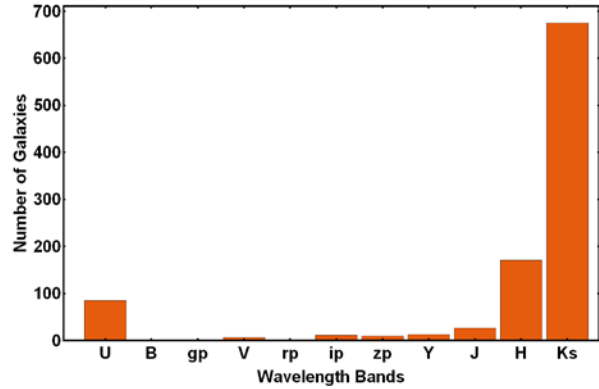


Figure 34 – Histogram plot of the number of galaxies in each wavelength band for the R subset whose ellipticity measurement variance is minimum using a 2.4 meter diameter telescope. There is a strong peak around the Ks-band showing a large majority of galaxies have their minimum value near these wavelengths.

6.1.3. Flux S/N and Ellipticity measurement variance with Gaussian Distributions

For comparison, the same calculations and plots for the ellipticity measurement variance as in Section 6.1.2 were also computed using the analytical Gaussian approximation in equation [128]. Relative to the non-Gaussian calculations, the average Gaussian ellipticity measurement variance values are generally slightly smaller, and the Gaussian plots mirror the trend of lower variance values over larger telescope diameters and minimum average variance around the Ks-band. Figure 37 and Figure 38 show the Gaussian ellipticity measurement variance plots for the Ks catalog. Because the Gaussian calculations are significantly faster, the average ellipticity measurement variance shown in these plots has been calculated across the entire set of 74,950 galaxies in the Ks catalog (instead of only a subset of 1000 as in Section 6.1.2), but only a couple

of hundred of individual galaxies are plotted in the background so as not to compromise the readability of the plot.

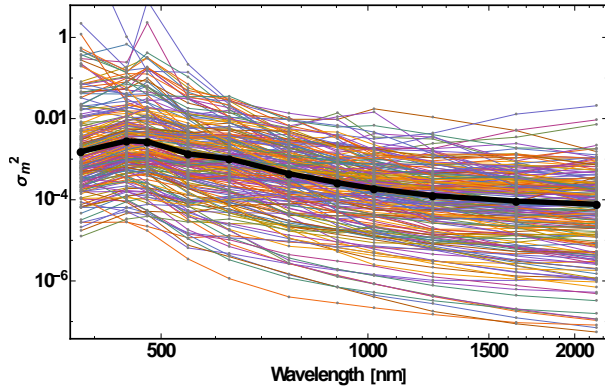


Figure 35 – Log-Log plot of ellipticity

measurement variance using Gaussian functions vs. wavelength for a 1.2 meter diameter telescope for a sample of galaxies in the Ks catalog. The bold black dots and line represent the median values at each wavelength band calculated over the full catalog. Median variance values are shown to have their lowest average value around the Ks-band.

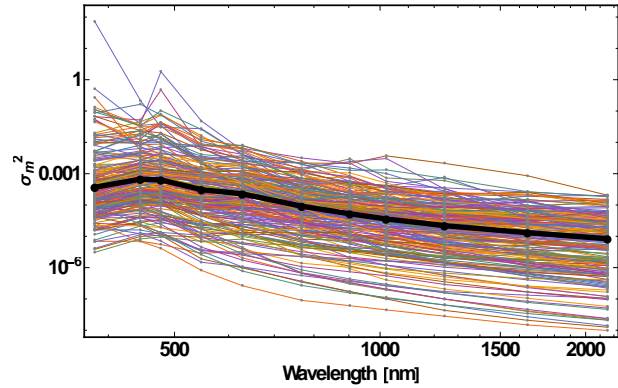


Figure 36 – Log-Log plot of ellipticity

measurement variance using Gaussian functions vs. wavelength for a 2.4 meter diameter telescope for a sample of galaxies in the Ks catalog. The bold black dots and line represent the median values at each wavelength band calculated over the full catalog. Median variance values are shown to have their lowest average value around the Ks-band.

6.1.4. Effective Galaxy Number

As discussed in Section 4.6, we have introduced in equation [133] an effective galaxy number per square degree, N_{eff} . In calculating N_{eff} , the Gaussian equations in Section 0 were used for the flux S/N and ellipticity measurement variance. The effective galaxy number was then computed at various wavelength bands across the full set of galaxies in our Ks and R catalogs and for integration times ranging from one to 10,000 seconds in powers of 10. Both a 1.2 meter and 2.4 meter diameter telescope were considered and plots of the results of the Ks

catalog are displayed in Figure 39 and Figure 40, and the R catalog results are displayed in Figure 41 and Figure 42.

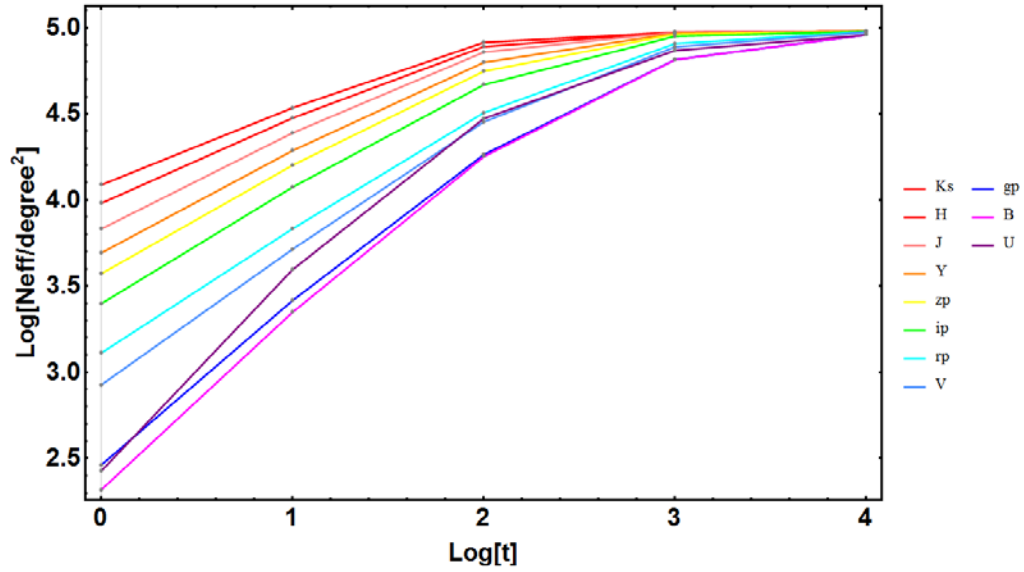


Figure 37 – Log-log plot of the effective galaxy number per square degree vs. integration time calculated from equation [133] with a 1.2 meter telescope diameter using the Ks catalog. Gaussian equations derived in Section 0 were used for the flux S/N and ellipticity measurement variance in these calculations.

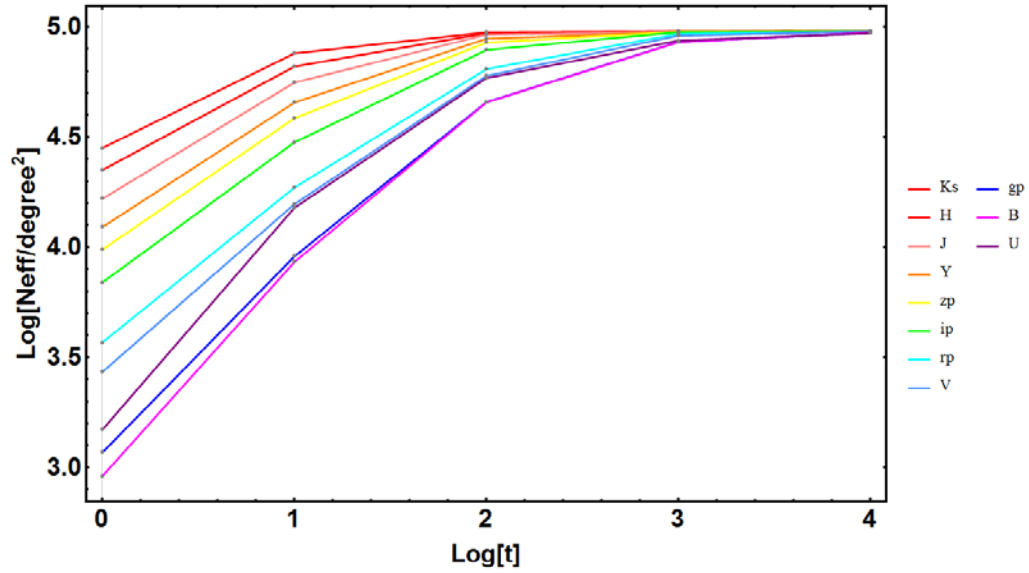


Figure 38 – Log-log plot of the effective galaxy number per square degree vs. integration time calculated from equation [133] with a 2.4 meter telescope diameter using the Ks catalog.

Gaussian equations derived in Section 0 were used for the flux S/N and ellipticity measurement variance in these calculations.

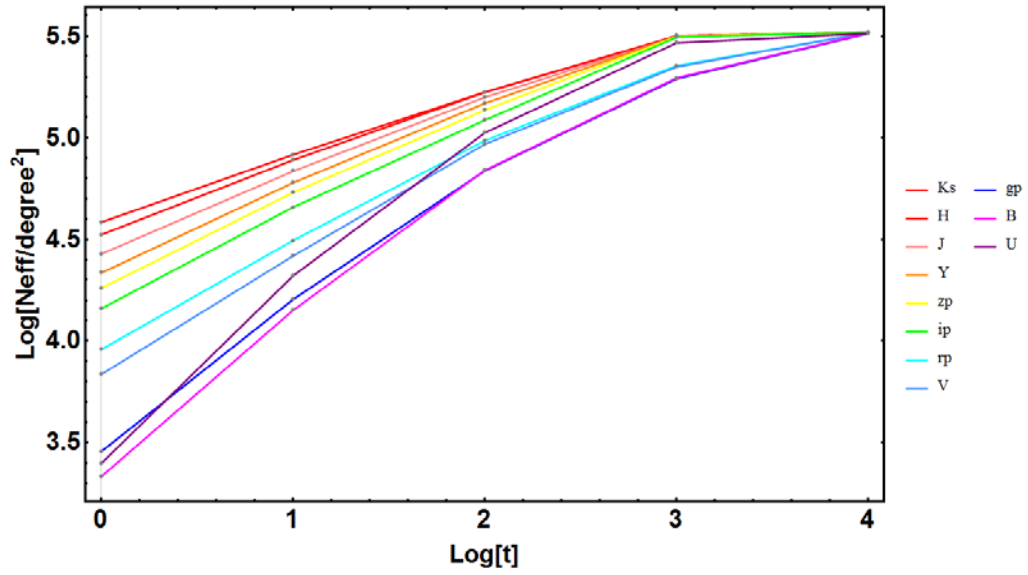


Figure 39 – Log-log plot of the effective galaxy number per square degree vs. integration time calculated from equation [133] with a 1.2 meter telescope diameter using the R catalog. Gaussian equations derived in Section 0 were used for the flux S/N and ellipticity measurement variance in these calculations.

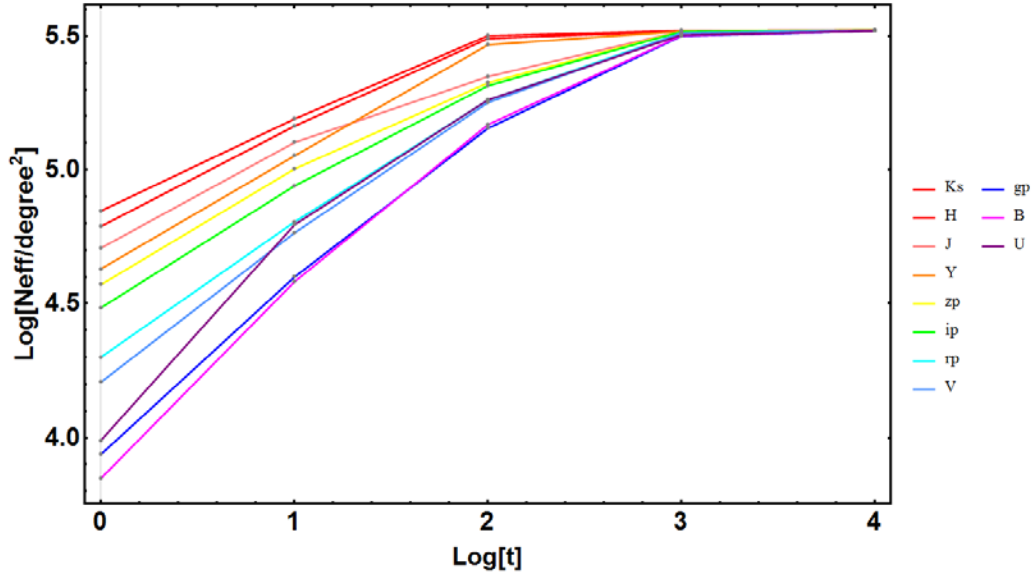


Figure 40 – Log-log plot of the effective galaxy number per square degree vs. integration time calculated from equation [133] with a 2.4 meter telescope diameter using the R catalog. Gaussian equations derived in Section 0 were used for the flux S/N and ellipticity measurement variance in these calculations.

Across all calculations of the effective galaxy number counts are highest in the Ks-band. At longer integration times, performance across wavelength bands begins to even out, at a depth where the incompleteness of the input catalogs becomes apparent in Figure 15. This saturation of the counts occurs at shorter integration times with the larger 2.4 meter telescope, as it is easier to collect more counts with the larger diameter and PSF smearing is less of an issue. Between the Ks catalog and the R catalog, the N_{eff} plots are qualitatively similar. Nevertheless, bluer bands obtain a higher N_{eff} in the R catalog, both in absolute value compared with Ks catalog, and relative to the longer wavelength band counts in the R catalog. In general, counts across all wavelength bands in the R catalog are larger than the corresponding counts from the Ks catalog,

but again, the two calculations are ultimately qualitatively similar, with the Ks counts in either catalog consistently being the largest across all telescope sizes and integration times considered.

6.1.5. Intrinsic Galaxy Ellipticity

In this paper, we have thus far assumed radially symmetric galaxy light profiles given by Sersic's equation, but we can also demonstrate here that the effect of an overall (average) intrinsic ellipticity among source galaxies produces no qualitative difference in the shear measurement results. By applying a linear transformation on the space coordinates in the Sersic profile equation, prior to lensing distortions, we transform the all circular galaxy light profiles into elliptical profiles. We impose an intrinsic 2:1 major axis ratio while preserving the area of the source so the peak surface brightness stays the same via the transformation

$$(x, y) \rightarrow (x', y') = \left(\sqrt{2}x, \frac{y}{\sqrt{2}} \right) \quad [142]$$

As before, a 10% stretch is then applied according to equation [107] to simulate gravitational shear, the Airy disk PSF is convolved with the now elliptical galaxy light profiles, and the ellipticity measurement variance is calculated via equation [115].

Figure 43 displays the ellipticity measurement variance vs. wavelength for the 1000 selected galaxies from the Ks subset used in Section 6.1.1, with non-trivial intrinsic ellipticity imposed on all galaxies, and we use a 1.2 meter telescope for this plot. Quantitatively, compared with the intrinsically circular results, the average ellipticity measurement variance values are very slightly increased on average for the elliptical light profiles across most wavelengths (these are difficult to perceive visually on these plots), but the behavior of the ellipticity measurement variance vs. wavelength is not significantly affected, and the average minimum ellipticity measurement variance is still located around the Ks-band.

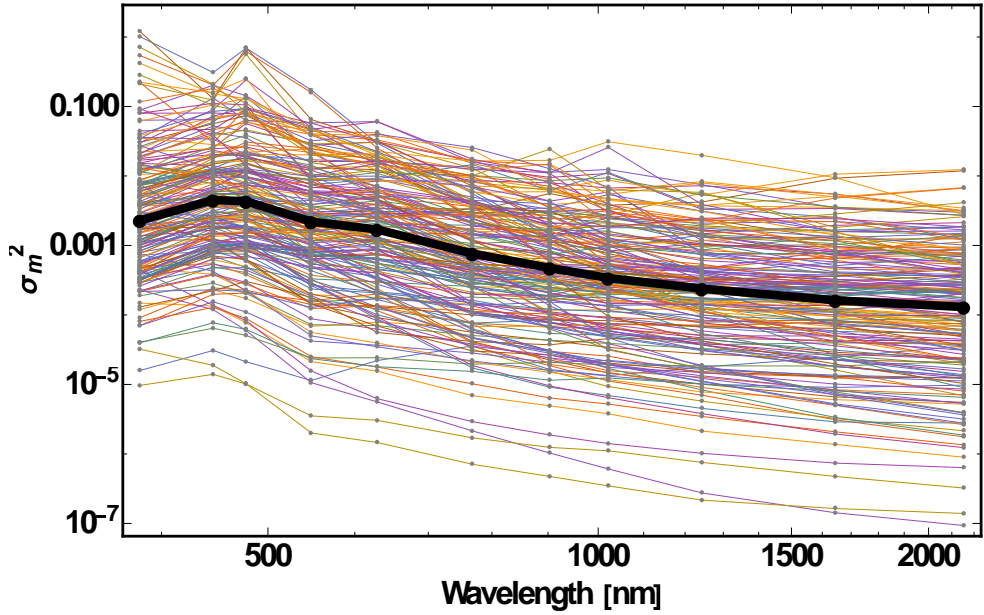


Figure 41 – Log-Log plot of ellipticity measurement variance vs. wavelength for a 1.2 meter diameter telescope for the Ks subset with a 1.2 meter diameter telescope with intrinsic 2:1 elliptical axis ratio imposed. The bold black dots and line represent the median values at each wavelength band. Median variance values are shown to have their lowest average value around the Ks-band. Comparing this with Figure 29, the two plots are nearly identical.

We have also tested the effects of intrinsic ellipticity on a 2.4 meter telescope and on the R subset applying the same procedure as outlined earlier in this section, and results are identical: ellipticity measurement variance values show a very slight increase on average after imposing 2:1 axis ratios on the intrinsic galaxy light profiles with negligible change to the average ellipticity measurement variance vs. wavelength curves displaying minimum variance around the Ks-band for both telescope sizes. We conclude the intrinsic ellipticity of galaxies does not appreciably affect the behavior of the ellipticity measurement variance across wavelengths.

6.1.6. Dependence on Effective Radius

Our results across all data sets consistently favor the Ks-band for maximum flux S/N. As might be expected, the total Ks-band flux generally increases with galaxy radius. Figure 44 displays total Ks-band flux vs. effective radii for the Ks subset used in Section 6.1.1. The plot demonstrates a general trend of increasing Ks-band surface brightness vs. galaxy size.

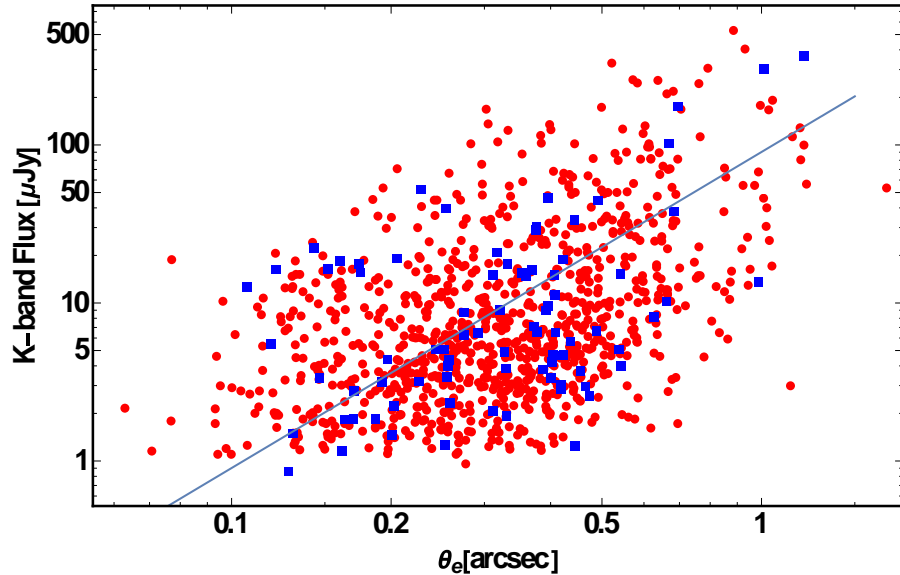


Figure 42 – Log-Log plot of total K-flux vs. effective half-light radius θ_e for 1000 galaxies in the Ks subset. Red circles indicate spiral galaxies with Sersic index $n = 1$, and blue squares indicate elliptical galaxies with Sersic index $n = 4$. The best fit line is of the form $\bar{F} \propto \theta_e^2$, under the assumption the original F_i are independently normally distributed with mean \bar{F}_i and common standard deviation.

6.2. HST Frontier Parallel Fields

6.2.1. Weak Lensing Measurement Performance Across Wavelength

The galaxy flux S/N and shape measurement uncertainty were computed via equations [122] and [128], respectively, for an integration time of 10,000 seconds and plotted vs. wavelength.

For visual clarity, only five hundred galaxies are individually plotted in Figure 45 and Figure 46, but the median galaxy flux S/N and shape measurement uncertainty are also shown, calculated across the full 6946 galaxies in our source catalog. These plots show the highest galaxy flux S/N and lowest shape measurement uncertainty are both found around the longest available wavelength near the H-band.

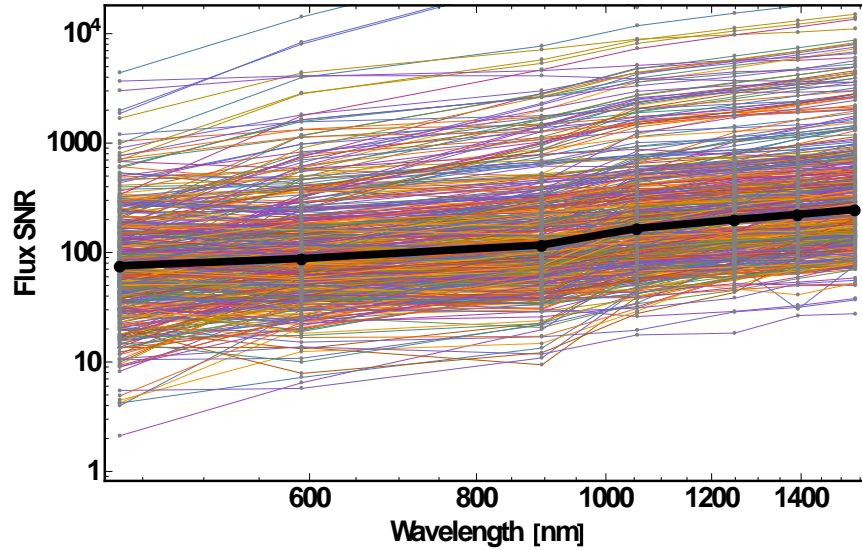


Figure 43 – Log-Log plot of galaxy flux S/N vs. wavelength. Individual data points are plotted for 500 randomly selected galaxies in our combined catalog. Bold black dots and line represent the median S/N values at each wavelength band, which is calculated across the full 6946 galaxy catalog. Median S/N values have their highest average value around the H-band.

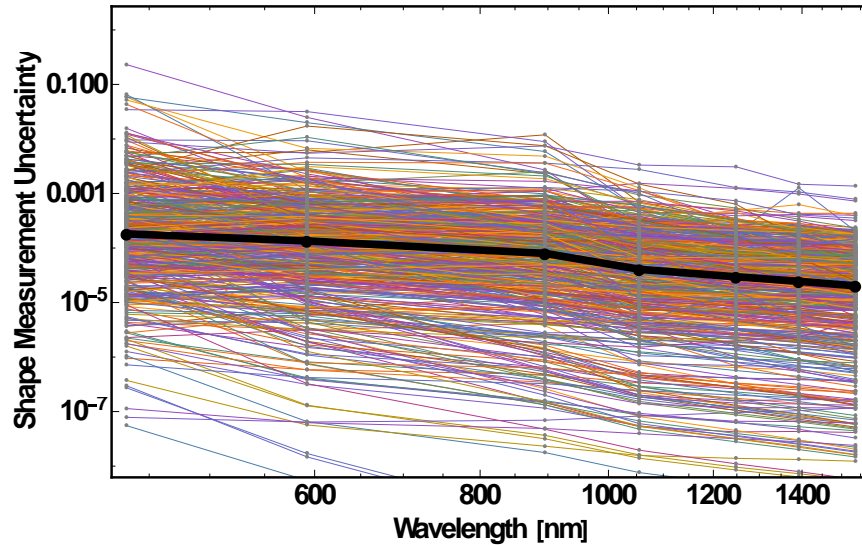


Figure 44 – Log-Log plot of galaxy shape measurement uncertainty vs. wavelength. Individual data points are plotted for the same 500 randomly selected galaxies as in Figure 45. Bold black dots and line represent the median shape measurement uncertainty values at each wavelength band, which is calculated across the full 6946 galaxy catalog. Median shape measurement uncertainty values have their lowest average value around the H-band.

The effective galaxy number was also computed at various wavelength bands across the full set of galaxies in the combined FPF catalog for a range of integration times varying from one to 10^6 seconds in powers of ten using equation [133]. Figure 47 displays a plot of the effective number density vs. integration for the various HST color filters.

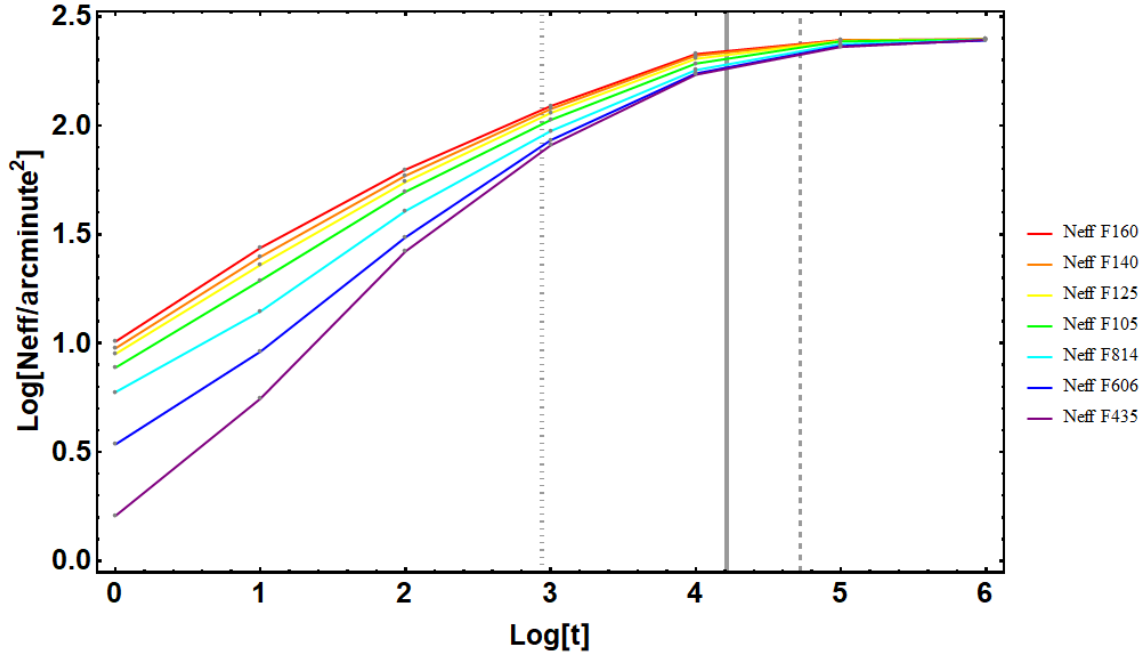


Figure 45 – Log-log plot of the effective galaxy number per square degree vs. integration time calculated from equation [133] for our combined catalog consisting of all six FPFs. The solid vertical line marks the equivalent integration time where the flux uncertainty in our model matches the average uncertainty obtained calculated from the weight maps of the FPF mosaics; the vertically dashed line to the right represents the approximate F160W filter integration time of the FF survey; and the horizontally dashed line to the left represents the integration time of future space telescope mission WFIRST HLS.

The effective galaxy number counts are shown to be highest around the longest available wavelength in the F160W H-band across all integration times. At longer integration times, the performance across wavelengths begins to even out at a depth where the incompleteness of the input catalogs becomes apparent. Since the measurement of weak lensing signal is statistical in nature, these calculations suggest better performance in the longer wavelengths where more galaxy counts can be obtained in shorter integration times. The solid vertical line in Figure 47

marking the equivalent integration time in our sky dominated model where the calculated flux uncertainty matches the median measured uncertainty in the weight maps of the FPFs mosaics, suggests the instrument sensitivity assumptions in our model of a diffraction-limited background-limited space telescope are optimistic, as is to be expected.

6.2.2. Weak Lensing Measurement Performance Across Wavelength

Using the galaxy shape quadrupole moments output by SExtractor, complex ellipticities were computed as per equation [68] for galaxy sources in the HST FPFs. Assuming a symmetric Gaussian PSF, equations [87] – [90] were used to extract approximate source ellipticities from each detected galaxy. Equations [137], [138], and [139] were then used to compute a weighted average ellipticity for each field, and we take this average ellipticity value to be an estimate of the reduced shear for each FPF, which we calibrate with the reported tangential shear value in Abell 2744 FPF measured by (Medezinsk, et al., 2016).

Table 6 summarizes the reduced shear magnitude and angle for each of the FPFs and an estimated encircled mass estimate at the location of the parallel fields using equation [85]. For this calculation, (Castellano, et al., 2016) was used to estimate the median redshift of sources in the parallel fields of Abell 2744 and MACS 0416. We calculate a range of encircled mass estimates corresponding the range of median redshifts we get for these two fields. The angles in Table 6 are given relative to the pointing direction of the corresponding primary field. Figure 48 through Figure 53 graphically summarizes the reduced shear angle at each of the HST FPFs and the relative pointing direction of the primary fields. Figure 54 displays a polar plot of individual galaxy shear vectors in the Abell 2744 parallel field using the shear magnitude as the polar radius and twice the angle as the polar angle. The distribution among galaxies appears random, but the average angle is close to tangent relative to the primary field pointing.

We expect the gravitational distortion at the location of the FPFs to be dominated the massive galaxy clusters of the primary fields, and hence, the direction of the shear in each parallel field should be tangent to radial pointing direction to each of corresponding primary fields. The mean angle relative to the primary pointing across the six fields is 85.6° with a standard deviation of 11.2° . In any given parallel field, the standard deviation of the average angle is around $50^\circ - 60^\circ$, a rather large spread, but the random distribution of intrinsic orientations is expected to vanish in the average, leaving only the relative angle pointing of the reduced shear vector, which we measure to be fairly close to 90° . In the Abell 2744 parallel field, (Medezinsk, et al., 2016) measured a tangential shear value at a the approximate location of the parallel field, a distance 6 arcminutes away from the primary field, of about 0.1. The corresponding tangential shear value that we would naively compute from our average ellipticity measurements is about 0.041. We thus apply a calibration factor of $\alpha = 2.44619$ to match our Abell 2744 measurement with (Medezinsk, et al., 2016), and we use this calibration factor across all fields to estimate an encircled mass via equation [85] and compare with the primary cluster masses reported in (Lotz, et al., 2017). Table 6 summarizes all of these results.

It should be noted that (Medezinsk, et al., 2016) uses a more complicated weight function to define the galaxy shape quadrupole moments and a more accurate and sophisticated method for deconvolving the PSF to obtain accurate measurements of galaxy source shapes. Also, equation [85] assumes a spherically symmetric mass distribution for the gravitational lens, but of course, the real primary FF are not perfectly symmetric but each possess their own structure and mass distributions.

	θ	$\langle g_t \rangle$	$\langle g_t \rangle_{cal}$	z_D	z_S	$M_{encircled}$ ($M_{sun} \times 10^{15}$)	Reported $M_{cluster}$ ($M_{sun} \times 10^{15}$)
Abell 2744	82.2°	0.041	0.1	0.308	1.7 – 2.1	2.01 – 2.00	1.8
Abell 1063	82.8°	0.025	0.062	0.348	1.7 – 2.1	1.46 – 1.40	1.4
Abell 370	92.8°	0.0147	0.036	0.375	1.7 – 2.1	0.916 – 0.872	1
MACS1149	83.1°	0.0154	0.038	0.543	1.7 – 2.1	1.44 – 1.33	2.5
MACS0717	70°	0.031	0.076	0.545	1.7 – 2.1	2.90 – 2.67	2 – 3
MACS0416	103.1°	0.019	0.048	0.397	1.7 – 2.1	1.30 – 1.23	1.2

Table 6 – The columns from left to right represent: 1) the FF cluster name; 2) the relative angle (in degrees) with respect to the primary field pointings; 3) the measured tangential shear as defined in Chapter 3.5; 4) calibrated tangential shear values so that tangential shear in the Abell 2744 parallel field matches the value reported in (*Medezinsk, et al., 2016*); 5) redshift of the primary FF cluster; 6) median redshift of the source galaxies in the parallel fields of Abell 2744 and MACS 0416, respectively, as measured in (*Castellano, et al., 2016*); 7) our calculated encircled mass estimate; and 8) the reported mass of the primary cluster in the FF as in (*Lotz, et al., 2017*). In the ideal case, the angles should be 90°, perpendicular to the primary field pointing. A multiplicative calibration factor of 2.44619 has been applied to the reduced shear values of all fields, chosen so that the Abell 2744 values match those in (*Medezinsk, et al., 2016*). In the mass estimate, the following cosmological parameters were used: $\Omega_m = 0.301$, $\Omega_r = 2.47 * 10^{-5}$, $\Omega_\Lambda = 1 - \Omega_m$, $\Omega_k = 0$, $H = 67.74$. The reported mass values in the far right column and the lens redshift of the primary fields z_D in the fifth column from the left are referenced from (*Lotz, et al., 2017*).

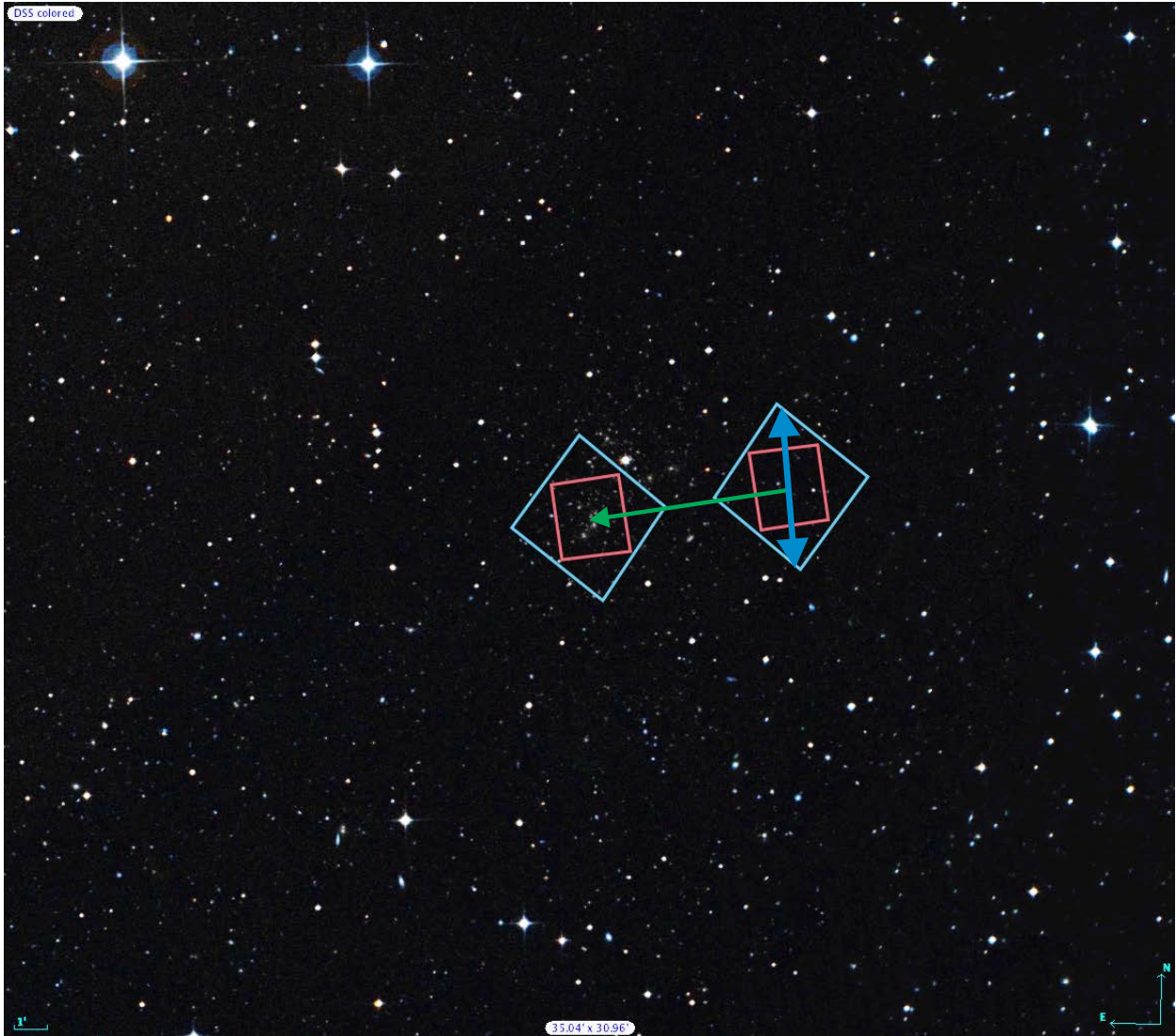


Figure 46 – The relative pointing directions of the primary Abell 2477 field w.r.t. the parallel field. The blue bi-vector represents the average measured shear direction in the parallel field and the green arrow points to the center of the primary field. The relative angle between the two was measured to be about 82 degrees.

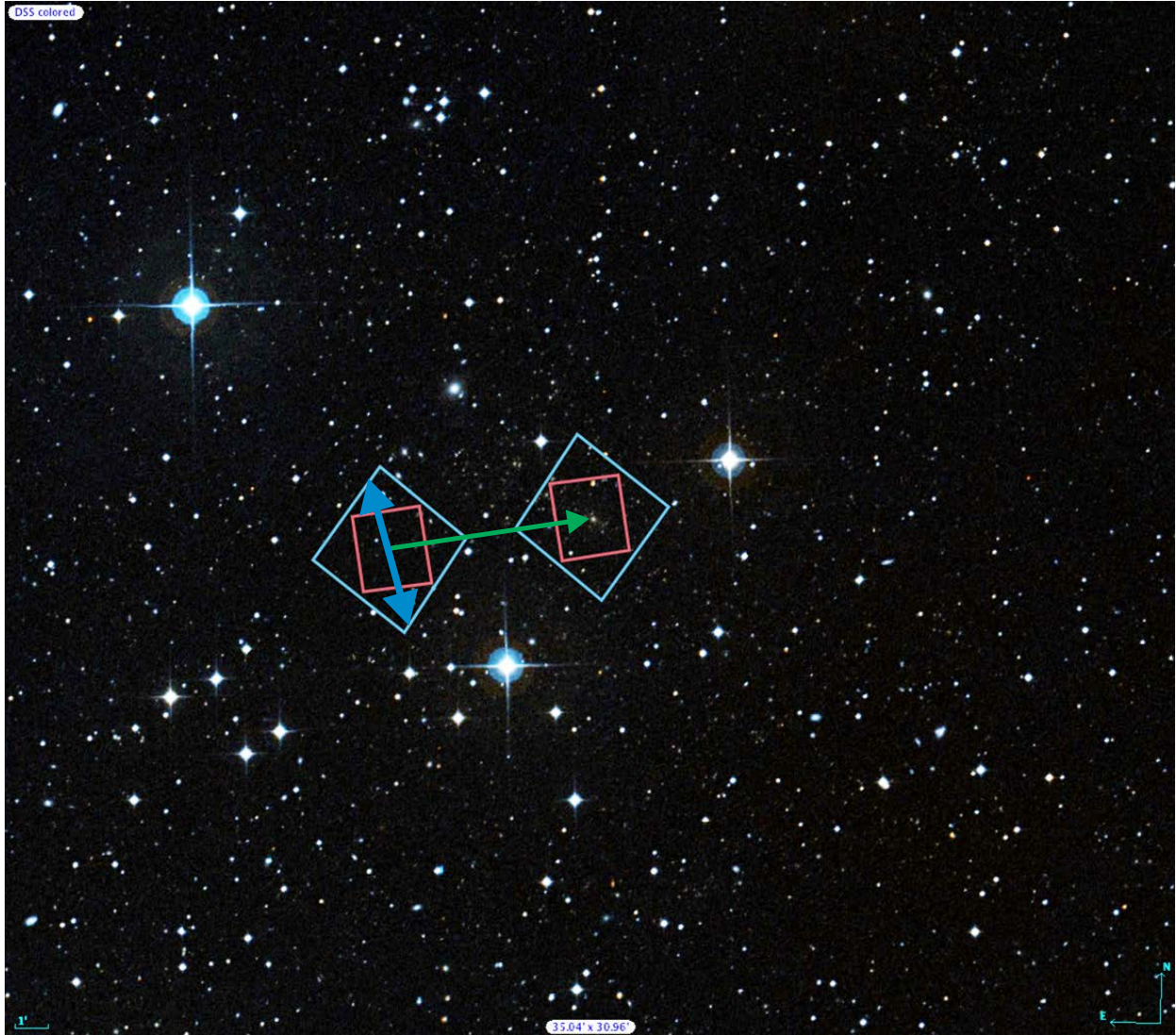


Figure 47 – The relative pointing directions of the primary Abell 1063 field w.r.t. the parallel field. The blue bi-vector represents the average measured shear direction in the parallel field and the green arrow points to the center of the primary field. The relative angle between the two was measured to be about 83 degrees.

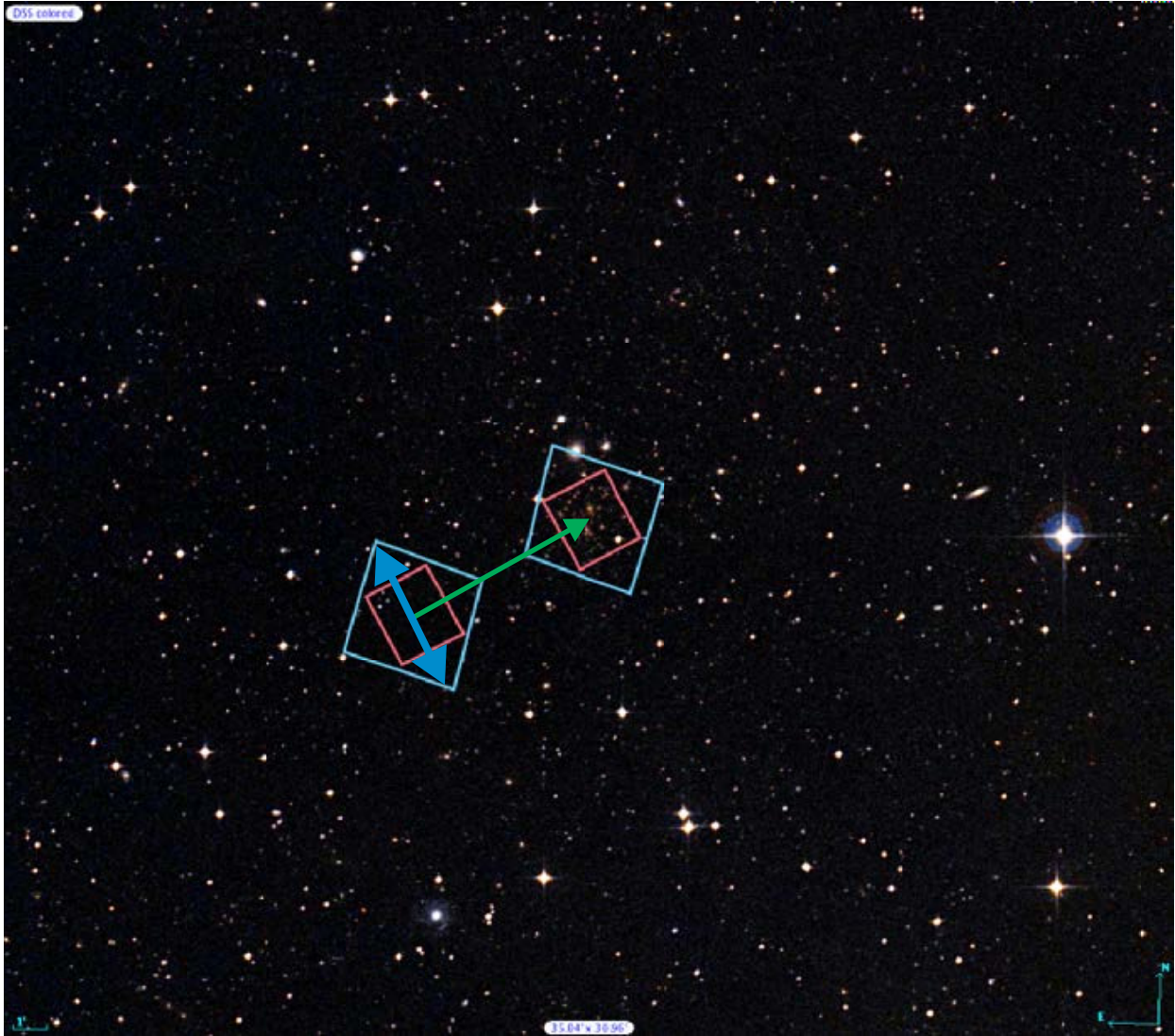


Figure 48 – The relative pointing directions of the primary Abell 370 field w.r.t. the parallel field. The blue bi-vector represents the average measured shear direction in the parallel field and the green arrow points to the center of the primary field. The relative angle between the two was measured to be about 93 degrees.

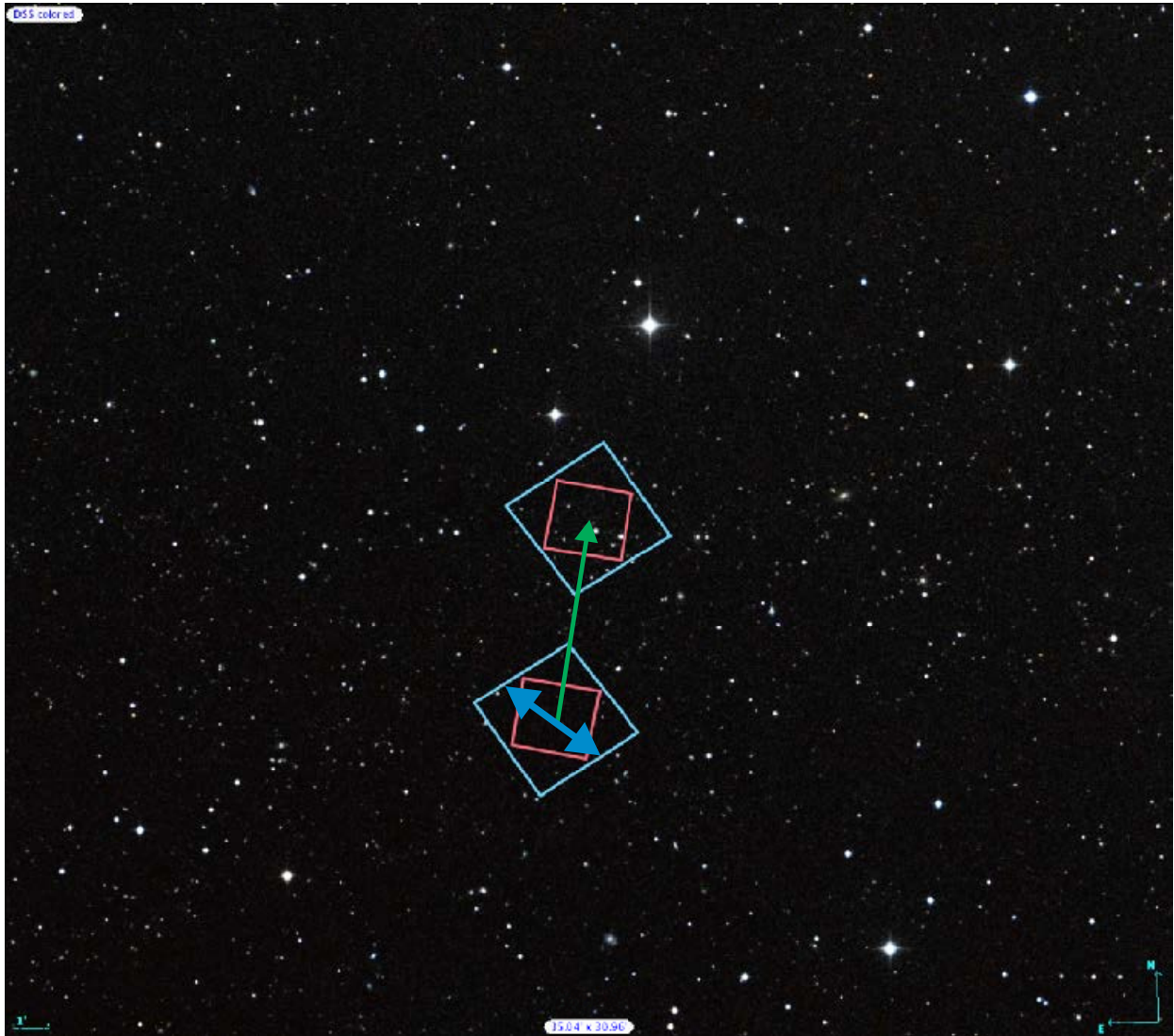


Figure 49 – The relative pointing directions of the primary MACS 1149 field w.r.t. the parallel field. The blue bi-vector represents the average measured shear direction in the parallel field and the green arrow points to the center of the primary field. The relative angle between the two was measured to be about 83 degrees.

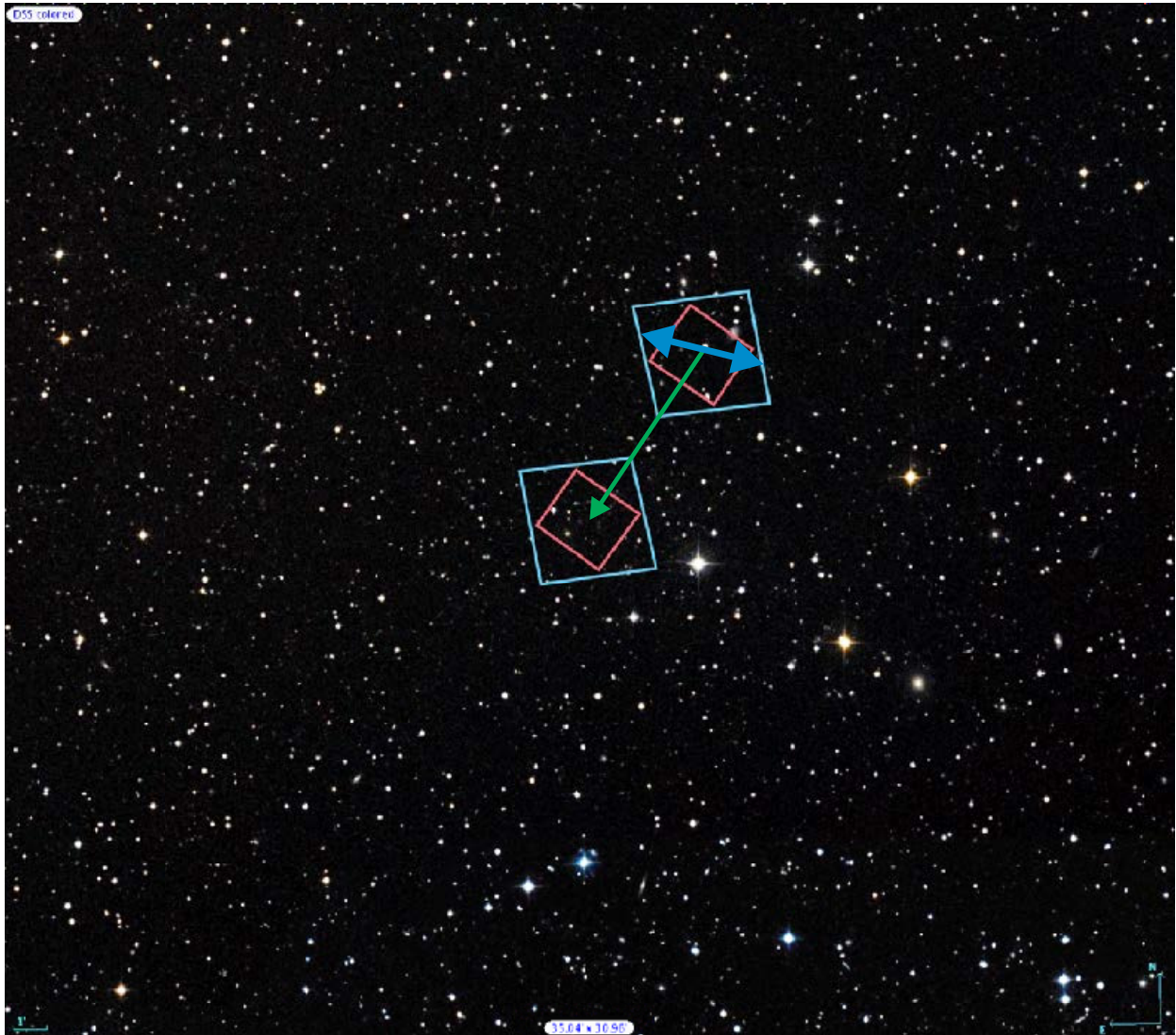


Figure 50 – The relative pointing directions of the primary MACS 0717 field w.r.t. the parallel field. The blue bi-vector represents the average measured shear direction in the parallel field and the green arrow points to the center of the primary field. The relative angle between the two was measured to be about 70 degrees.

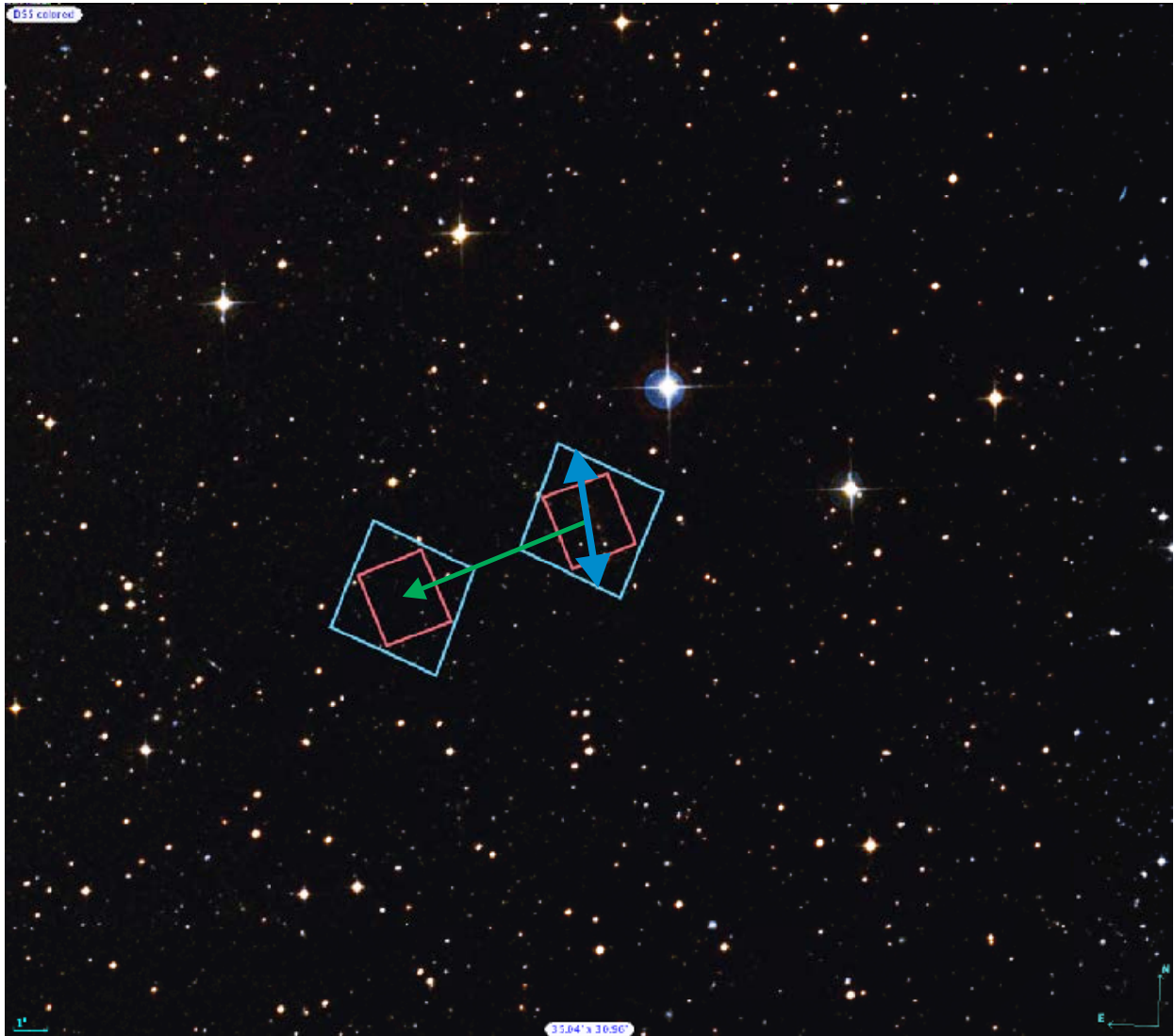


Figure 51 – The relative pointing directions of the primary MACS 0416 field w.r.t. the parallel field. The blue bi-vector represents the average measured shear direction in the parallel field and the green arrow points to the center of the primary field. The relative angle between the two was measured to be about 103 degrees.

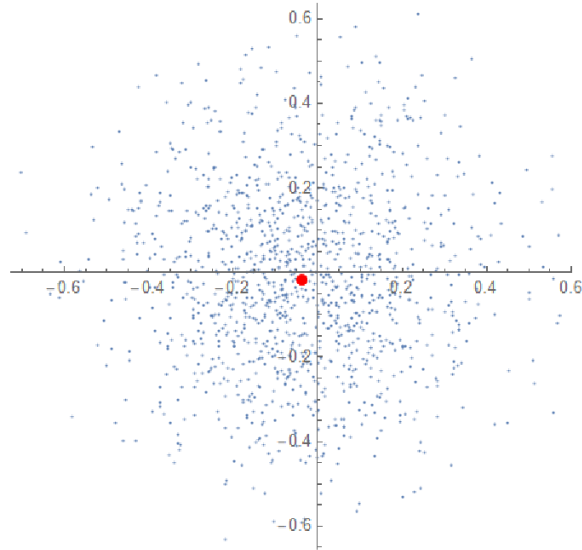


Figure 52 – Polar plot of individual galaxy ellipticity vectors in the Abell 2744 parallel field using the ellipticity magnitude as the polar radius and twice the angle as the polar angle. The distribution among galaxies appears random, but the average angle is close to tangent relative to the primary field.

7. Conclusion

Our results suggest that weak lensing shear measurement performance is improved at longer wavelengths where flux SNR and galaxy number density are largest and the shape measurement uncertainty is smallest. This conclusion is consistent across each of the galaxy catalogs considered.

For the ULTRAVISTA field catalogs and results, the lower zodiacal background at 2 – 4 μm and the galaxy flux peaking in the Ks-band combine to make the optimum band for observing shear in our sample of galaxies to be near the Ks-band around 2.2 μm , and our numerical calculations confirm this result. For the 1.2 meter and 2.4 meter diameters we

considered, and across both the R selected and Ks selected sets of galaxy data, the J band at $1.25 \mu\text{m}$ gives ellipticity measurement variance values on average 1.5 to 2.5 times higher than at the Ks-band. Relative to the r+ band at $0.66 \mu\text{m}$, our calculations show the ellipticity measurement variance at the Ks-band with a 1.2 meter telescope to be around four times smaller in the R catalog and about 13 times smaller in the Ks catalog. For a 2.4 meter telescope, the ellipticity measurement variance at the r+ band relative to the Ks-band is around 6.5 times smaller in the R catalog and about 20 times smaller in the Ks catalog.

Our plots of the effective number of galaxies with measurable shapes per square degree in Section 6.1.4 further validate wavelengths near the Ks-band as being optimal for weak lensing measurements. For both the Ks and R selected UltraVISTA catalogs, our results show that the highest number of effective counts generally occur around the Ks-band across all integration times and both telescope sizes considered. At the largest of integration times, counts for both telescopes in our plots saturate, implying the input galaxy catalogs used in our calculation are becoming incomplete. Thus our calculations do not fully include the additional weak lensing performance coming from fainter background galaxies that benefit from the longest integration times. As the original ULTRAVISTA survey had a depth of one HST orbit per ACS field, this incompleteness is expected.

In the HST FF survey considered in this paper, the HST F160W H-band filter provides the longest available wavelength in our galaxy data, leaving us with a smaller wavelength range than the ULTRAVISTA field catalogs. Additionally, while the ULTRAVISTA survey covered a larger sky area compared to the FF survey, the FFs are considerably deeper and have been observed by the HST over a longer total integration time. Despite these differences, we find the same type of improvements at longer wavelengths.

We note that while Figure 47 shows increasing effective galaxy number over increasing telescope integration time, practically speaking it is preferable for weak lensing measurements to prioritize a wider area survey rather than a deeper one. Not only is a faster survey cheaper and easier to schedule, but the effective galaxy number scales linearly with solid angle, whereas an approximate log-log slope of Figure 47 up to 10^3 seconds suggests slightly less than $1/3$ power law scaling (0.30) of the effective number counts vs. integration time in the H-band. So, for example, while an eight times longer survey could yield a roughly two times larger density count, it would be considerably easier to simply survey a twice larger surface area for the same advantage.

Future space telescope project WFIRST (Spergel, et al., 2015) is planned to launch with a 2.4 meter telescope like the HST, but the wide field camera of WFIRST will have a FoV 200 times larger than HST's powerful WFC3 IR camera. The WFIRST high-latitude survey (HLS) is a proposed wide-area weak lensing survey which will image 2227 square degrees of sky in 4 NIR bands spanning the range of 0.92 – 2.00 microns. The survey will have an exposure time of 5×174 seconds per filter, and WFIRST is expected to yield an effective galaxy number density of 45 per square arcminute in the HLS, or potentially 200 – 300 per arcminute in longer, targeted observations (Spergel, et al., 2015). In contrast, the FF survey data used in this paper was observed over 70 HST orbits per camera, consisting of ~10-40 HST orbits per filter, with a typical exposure time during an orbit of ~2,200 seconds, which is ~25 – 100 times longer per filter than the HLS. However, the entire FF survey was viewed across six FoVs of the comparatively smaller HST camera area. In terms of the weak lensing measurement performance as studied here, the smaller exposure time of the HLS versus the FF survey should be compensated by the much larger observation area of the WFIRST HLS.

We can attempt a crude comparison of our model's performance in this paper with the future WFIRST HLS. Scaling the FF exposure time by the HLS exposure time and multiplying by the equivalent integration time in our model where the calculated flux uncertainty matches the real telescope data of the FPF weight maps yields an effective time of 270 seconds. This effective time of 270 seconds is about one third of the real HLS exposure time and correlates in Figure 47 to an effective galaxy number density of roughly 80 per square arcminute. This is higher than the HLS's reported count of 45 per square arcminute, but again, we understand that our model is optimistic and performs about three times better than the real HST FF survey according to Figure 47. This straightforward comparison is further complicated by the fact that HLS's reported density count of 45 galaxies per square arcminute is presumably obtained by taking into account the measurement performance of all available wavelength bands together to increase overall S/N, while here we are only using our model to investigate performance in individual bands; e.g., the H-band. This gives the reported HLS performance an advantage versus the numbers we have quoted here in this paper from our model, but ultimately our simple model of a diffraction-limited background-limited space telescope still comes out overly optimistic relative to the impressive performance of the WFIRST HLS.

For some final thoughts, we emphasize that the objective of this project is not to directly compare the performance of specific space telescopes, but rather to simply track the weak lensing measurement behavior across wavelength bands. While our model is simplistic, we believe it is sophisticated enough to provide some insight towards this objective. Nevertheless, there are some relevant features that our model admittedly neglects, and including features these in later works could lead to further improvements and refinements of the results therein.

For one, the variation of galaxy shape noise as a function of wavelength is currently assumed to be constant in this model. Lifting this restriction would be a good test to see if our results still hold. Our model also largely ignores galaxy redshift information. Higher redshift galaxies are both redder and carry more lensing signal. It could be useful to account for the relationship between the redshift distributions of galaxies in different bands and the amount of shear signal they carry. Additionally, galaxy populations with a well-measured number density as a function of redshift are more useful for mapping cosmic shear than those with poorly measured $n(z)$. It would be productive to investigate the relationship between the redshift measurement uncertainty and the wavelength of observation. While this current work focusses on finding the highest galaxy flux S/N and lowest shape measurement uncertainty as functions of wavelength for weak lensing measurement, this does not necessarily translate to which galaxies are most useful for weak lensing for the reasons stated above. Improving our model to account for this in the future could proceed by adding redshift information to the simulated catalogs, before applying a redshift-dependent shear with a given power spectrum. From these catalogs, it would then be possible to measure the ability of each sample to recover the input shear signal.

In an attempt to measure an approximate shear signal in the HST FPFs using SExtractor's equipped quadrupole moment definitions and under the assumption of a purely symmetric Gaussian PSF, we seem to have been able to pick up the tangent direction of the shear vectors in each of the fields but significantly under sampled the shear magnitudes. Our average shear angles in the parallel fields are tangent in all six parallel fields relative to the primary field pointing directions, as would be expected of gravitational shear.

A more robust weighing scheme in the quadrupole moment definitions could increase the accuracy of the shape measurements, providing better shear estimates and better mass estimates.

Most weak lensing groups use more sophisticated quadrupole moment definitions, with the understanding that real-life telescope measurements do strictly follow the weak lensing theory outlined in Chapter 3. It is possible that our I_{th} cutoff too small to pick up good galaxy shapes, but have attempted to correct for this by calibrating our shear measurements to the values reported in (Medezinsk, et al., 2016). We have also not individually inspected each galaxy source for accuracy. Neighboring images that SExtractor might count as a single source could lead to awkward shapes and drastically different measurement outputs.

To improve our shear estimates, a more accurate PSF would produce more realistic source ellipticities. We have not accounted for anisotropy or instability of PSF, and we have assumed that the PSF is uniform across CCD frame. As is always the case in weak lensing measurements, higher number density could lead to more accurate statistics and better shear estimates. The FFs are sufficiently deep, but relatively small. We have also assumed that the theoretical equations of weak lensing theory hold and can be used exactly as derived in Chapter 3. This is not quite the case. We are ignoring complications that incur from pixelization on the CCD field and the complications introduced by realistic PSFs of real telescopes. Instead, we have simply assumed that deconvolution of isotropic PSF according to equations [87] – [90] is reasonable, while the real PSF is not purely isotropic, or symmetric, or time independent.

Using our estimated shear values, our encircled mass estimates are of the right order of magnitude, and generally larger than the reported cluster masses. This trend is expected given that our encircled mass estimates are by definition summing over a larger area than just the main galaxy clusters whose masses are referenced in Table 6. However, two of the parallel fields, Abell 370 and MACS1149 have the smallest measured shear values and the corresponding encircled mass estimates are smaller than the reported cluster masses, the latter field having the

largest discrepancy of any of the fields. The method we use to calculate the encircled mass estimates assumes a circularly symmetric mass distribution for the lensing galaxy clusters in the primary FPs. The real clusters, however, have more complicated extended structure, which could be part of why the encircled mass estimates we calculate for these two fields under this assumption are not coming out equal or larger than the primary cluster masses as naively expected.

Nevertheless, despite our crude estimates of the reduced shear and encircled mass in the six FPs, shear measurements in NIR bands are completely reasonable to perform, and based on the results of our current work we can conclude that weak lensing measurement performance benefits from observations at longer wavelengths up to about the K-band, unless limited by thermal background from the telescope or interplanetary dust reduces the sensitivity. Using a colder mirror allowing longer wavelength bands beyond the H-band in future space telescopes could, therefore, lead to further performance improvements and benefits for weak lensing science.

This research has made use of the NASA/IPAC Infrared Science Archive, which is operated by the Jet Propulsion Laboratory, California Institute of Technology, under contract with the National Aeronautics and Space Administration.

This study is based on a Ks-selected (and R-selected) catalog of the ULTRAVISTA/UltraVISTA field from Muzzin et al. (2013). The catalog contains PSF-matched photometry in 30 photometric bands covering the wavelength range 0.15 micron – 24 micron and includes the available GALEX (Martin et al. 2005), CFHT/Subaru (Capak et al. 2007), UltraVISTA (McCracken et al. 2012), S-ULTRAVISTA (Sanders et al. 2007), and zULTRAVISTA (Lilly et al. 2009) datasets.

References

Bartelmann, M. & Schneider, P., 1999. [Online]

Available at: <http://arxiv.org/abs/astro-ph/9912508v1>

[Accessed 2018].

Baxter, E. J. et al., 2013. The Kilo-Degree Survey. *The Messenger*, Volume 154, pp. 44-47.

Baxter, E. J. et al., 2018. Dark Energy Survey Year 1 Results: Methodology and Projections for Joint Analysis of Galaxy Clustering, Galaxy Lensing, and CMB Lensing Two-point Functions. *arXiv:1802.05257*.

Bertin, E., 2018. *SExtractor v2.13 User's Manual*. [Online]

Available at: <https://www.astromatic.net/pubsvn/software/sextractor/trunk/doc/sextractor.pdf>

Bertin, E. & Arnouts, S., 1996. SExtractor: Software for source extraction. *A&AS*, Volume 117, p. 393.

Bonnet, H. & Millier, Y., 1995. Statistical analysis of weak gravitational shear in the extended periphery of rich galaxy clusters.. *A&A*, Volume 303, p. 331.

Dressel, L., 2016. *Wide Field Camera 3 Instrument Handbook, Version 8.0*. [Online]

Available at:

http://www.stsci.edu/hst/wfc3/documents/handbooks/currentIHB/wfc3_cover.html#386407

Graham, A. W. & Driver, S. P., 2005. A Concise Reference to (Projected) Sérsic $R^{1/n}$ Quantities, Including Concentration, Profile Slopes, Petrosian Indices, and Kron Magnitudes. *PASA*, 22(2), pp. 118-127.

Heymans, C. et al., 2012. CFHTLenS: the Canada-France-Hawaii Telescope Lensing Survey. *Monthly Notices of the Royal Astronomical Society*, 427(1), pp. 146-166.

Ilbert, O. et al., 2009. COSMOS Photometric Redshifts with 30-bands for 2-deg². *ApJ*, Volume 290, pp. 1236-1249.

Kacprzak, T. et al., 2012. Measurement and calibration of noise bias in weak lensing galaxy shape estimation. *Monthly Notices of the Royal Astronomical Society*.

Kaiser, N., 2007. Weak Lensing Cosmology with Pan-STARRS. *Bulletin of the American Astronomical Society*, Volume 39, p. 163.

Kaiser, N., Squires, G. & Broadhurst, T., 1995. A Method for Weak Lensing Observations. *ApJ*, Volume 449, pp. 460 - 475.

Koekemoer, A. et al., 2014. The HST Frontier Fields: Science Data Pipeline, Products, and First Data Release. *AAS*, 223(254.02).

Leauthaud, A. et al., 2007. Weak Gravitational Lensing with COSMOS: Galaxy Selection and Shape Measurements. *ApJS*, 172(219).

Lotz, J. M. et al., 2017. The Frontier Fields: Survey Design. *APJ*, 837(1).

LSST-Science-Collaboration, et al., 2009. LSST Science Book, Version 2.0. *eprint arXiv:0912.0201*.

M. Castellano¹, R. A. et al., 2016. The ASTRODEEP Frontier Fields Catalogues: II - Photometric. *A&A*, Volume 590.

Madau, P. & Pozzetti, L., 2000. Deep galaxy counts, extragalactic background light and the stellar baryon budget. *Monthly Notices of the Royal Astronomical Society*, 312(2), pp. L9-L15.

Matthias Bartelmann, P. S., 2001. Weak gravitational lensing. *Physics Reports*, 340(4-5), pp. 291-472.

Medezinsk, E. et al., 2016. Frontier Fields: Subaru weak-lensing analysis of the merging galaxy cluster A2744. *ApJ*, 817(1), p. 16.

Muzzin, A. et al., 2013. A public Ks-selected catalog in the COSMOS/ULTRAVISTA field: Photometry photometric redshifts and stellar population parameters. 206(8).

NASA, E. &., 2012. *Seeing quadruple*, s.l.: ESA/Hubble & NASA.

NASA, E. S. S. t., 2005. *A Gallery of Einstein Rings*, s.l.: NASA, ESA, SLACS Survey team.

Nemiroff, R. & Bonnell, J., n.d. *A Horseshoe Einstein Ring from Hubble*, s.l.: NASA Picture of the Day.

Racca, G. D. et al., 2016. *The Euclid mission design*. [Online]

Available at: <https://arxiv.org/abs/1610.05508>

Refregier, A. et al., 2010. Euclid Imaging Consortium: Imaging the dark Universe with Euclid.

Schneider, P., 1999. *Weak Gravitational Lensing*. [Online]

Available at: <http://arxiv.org/abs/astro-ph/0509252v1>

[Accessed 2008].

Schneider, P., 1999. *Weak Gravitational Lensing with SKA*. [Online]

Available at: <http://arxiv.org/abs/astro-ph/9907146>

Scoville, N. et al., 2007. The Cosmic Evolution Survey (COSMOS): Overview. *ApJs*, 172(1).

Sersic, J. L., 1963. Influence of the atmospheric and instrumental dispersion on the brightness distribution in a galaxy. *Boletin de la Asociacion Argentina de Astronomia*, Volume 6, p. 41.

Spergel, D. et al., 2015. *Wide-Field InfraRed Survey Telescope- Astrophysics Focused Telescope Assets WFIRST-AFTA 2015 Report*, s.l.: NASA.

Tung, N. & Wright, E., 2017. On Using a Space Telescope to Detect Weak-lensing Shear. *PASP*, Volume 129.

Wright, E. L., 1985. On Using a Space Telescope to Detect Faint Galaxies. *Astronomical Society of the Pacific*, 97(591), pp. 451-453.

Wright, E. L., 1998. Angular Power Spectra of the COBE DIRBE Maps. *ApJ*, 496(1), pp. 1-8.